THE THEORETICAL AND TRANSLATIONAL ADVANCEMENT OF DIFFUSE CORRELATION SPECTROSCOPY MEASUREMENTS OF BLOOD FLOW

A Dissertation
Presented to
The Academic Faculty

By

Eashani Sathialingam

In Partial Fulfillment
of the Requirements for the Degree
Doctor of Philosophy in the
Wallace H. Coulter Department of Biomedical Engineering

Georgia Institute of Technology &
Emory University
August 2022

THE THEORETICAL AND TRANSLATIONAL ADVANCEMENT OF DIFFUSE CORRELATION SPECTROSCOPY MEASUREMENTS OF BLOOD FLOW

Approved by:

Erin M. Buckley, PhD,
Research Advisor
Department of Biomedical Engineering
Georgia Institute of Technology & Emory University

Brandon Dixon, PhD
Department of Mechanical Engineering
Georgia Institute of Technology

Shella Keilholz, PhD
Department of Biomedical Engineering
Georgia Institute of Technology & Emory University

Wilbur Lam, MD, PhD
Department of Biomedical Engineering
Georgia Institute of Technology & Emory University

Ofer Sadan, MD, PhD
Department of Neurology and Neurosurgery
Emory University School of Medicine

Date Approved: 05/16/2022

Dedication

To my parents, Sathialingam and Vasuki, and my younger brother, Mayilone.

To my grandparents, Paramasamy and Maheshwary.

ACKNOWLEDGEMENTS

I couldn't have accomplished any of this work in this thesis without the support of a large number of people. My parents and brother were there with me from the beginning, and I would not be the person who I am today without them. From a young age, my parents fostered a passion for science and technology and always encouraged me to work hard. I truly appreciate their willingness to drop everything to help me. Seeing my dad have a PhD in civil engineering also motivated me to work towards achieving my own PhD. I have to thank both my grandpa and grandma for their unconditional love, encouragement, and support, as they ultimately inspired me to pursue biomedical engineering.

As a first-year graduate student at Georgia Tech, I'm grateful I ended up matching with Dr. Erin Buckley to be my PhD mentor. Erin has been an ideal mentor. She always wants the best for her students and has always pushed me to excel, from giving talks at many seminars and conferences to applying for fellowships and internships. I will always appreciate the weekly meetings we had in my first year to discuss diffusion theory, imaging modalities, and sickle cell disease in preparation for my qualifying exam. She has taught me how to give great talks, pay attention to detail, write concisely, keenly examine data, present clean figures, and many more. I appreciate that Erin is always there for her students, whenever they need her, even if she, herself, is swamped with work. Her door is always open to discuss findings and results. She truly has been one of the biggest supporters to see me succeed and is one of my biggest advocates.

I have to also thank my collaborators Drs. Wilbur Lam and Ofer Sadan. Dr. Lam introduced me to his lab members, Evelyn K. Williams and Dr. Rob Mannino, who worked with me to design the microfluidic phantoms and also helped to draw blood from healthy

subjects. I have to also thank Dr. Lam for serving as my co-sponsor for the NIH/NHLBI F31 fellowship.

Without the collaboration with Ofer for measuring SAH patients at Emory's neuroICU, none of my Aim 2 work would have been possible. Ofer has been a strong collaborator because he worked with me to make every measurement happen regardless of how early or late it was, even on weekends. He also has taught me about not only the clinical aspects of this project but also the clinical utility of translating DCS to routinely measure patients. Also, I have to thank him for introducing me to the rest of his team: Drs. Prem Kandiah, Feras Akbik, Cederic Pimental, David Pearce, and Owen Samuels, who have all been extremely receptive to this research device and equally interested in the success of this project. Finally, I have to thank all of the nurses and clinical fellows at the neuroICU; all of the staff have been so friendly to me and made sure that these measurements happened.

I have to also thank the Buckley lab members. Dr. Bharat Sanders, who was the first Buckley lab member I met, showed me around the lab, and became one of my good friends. Dr. Paul (Seung Yup) Lee, who was not only a helpful member to bounce ideas off of but also a great friend to talk to especially during our frequent 5 pm catchup talks. Kyle Cowdrick provides not only support alongside measurements but also comedic relief during our clumsy moments. Amanda Liew, who was a great lab manager, accompanied me to many patient measurements, and became another close friend of mine after having many lunches together and spending late nights in lab. Rowan Brothers, who was a kind friend and helped me with instrumentation/hardware for both lab-related issues and my car. I am also grateful to have met Tara Urner, Lilly Rohrer, Hongting Zhao, and Michelle Lin.

Finally, the work presented here would not have been possible without the financial support of Dr. Buckley, a NIH F31 pre-doctoral fellowship (HL154703-01A1) from the National Heart, Lung, and Blood Institute (NHLBI), and the Andy Zebrowitz Memorial Graduate Research Fund.

TABLE OF CONTENTS

ACKNOWLEDGEMENTS iv
LIST OF TABLES x
LIST OF FIGURES xi
LIST OF SYMBOLS AND ABBREVIATIONS xiv
SUMMARY xvi
Chapter 1: Background 1
1.1 Importance of Cerebral Blood Flow 1
1.2 Quantifying Cerebral Blood Flow with Current Imaging Modalities 1
1.2.1 Perfusion Magnetic Resonance Imaging 2
1.2.2 Nuclear Medicine (PET/SPECT) 4
1.2.3 Xenon-CT 5
1.2.4 Transcranial Doppler Ultrasound 6
1.3 Diffuse Correlation Spectroscopy 6
1.4 Overview 7
Chapter 2: Diffuse Correlation Spectroscopy 9
2.1 Radiative Transport Equation 9
2.2 Photon Diffusion Equation 11
2.3 Diffuse Correlation Spectroscopy 14
2.4 Correlation Transfer Equation 15
2.5 Correlation Diffusion Equation 17
2.6 Diffuse Correlation Spectroscopy Instrumentation 19
2.6.1 Lasers 19
2.6.2 Correlator 21
2.6.3 Sensor Design 22
2.7 Monte Carlo Simulations 23
Chapter 3: Exploring the Validity of the Correlation Diffusion Equation at Small Source-Detector Separations 27
3.1 Introduction 27
3.2 Materials and Methods 29
3.3 Results 38
3.4 Discussion 44

3.5 Conclusion 48
Chapter 4: Microfluidics and DCS 50
4.1 DCS-measured Blood Flow Index is Inversely Proportional to Hematocrit 50
4.1.1 Introduction 50
4.1.2 Materials and Methods 53
4.1.3 Results 61
4.1.4 Discussion 65
4.1.5 Conclusion 69
4.1.6 Appendix 1 70
4.2 Influence of Vessel Size on the DCS-measured Blood Flow Index 71
4.3 Influence of sickle cell blood on DCS blood flow measurements 76
4.3.1 Introduction 76
4.3.2 Methods 77
4.3.3 Results 79
Appendix 1: How to Construct the Microfluidic Phantom 79
Appendix 2: How to make DCS measurements with microfluidic devices 82
Appendix 3: Ergodicity 83
Appendix 4: Integrating Sphere to Assess the Optical Properties of Sickle Blood 85
Experimental Setup and Data Acquisition 86
Chapter 5: Subarachnoid Hemorrhage and DCS 89
5.1 Introduction 89
5.2 DCS-measured Blood Flow Response to the First Dose of IT Nicardipine is Associated with Patient Outcomes 91
5.2.1 Materials and Methods 91
5.2.2 Results 97
5.2.3 Discussion 103
5.2.4 Conclusions 107
5.3 DCS-Measured Cerebral Blood Flow Changes in IT Nicardipine Over Multiple Days 108
5.3.1 Methods 108
5.3.2 Results 110
5.3.3 Conclusion 113
5.4 Diffuse Optical Spectroscopies for Daily Trends from IT Nicardipine 114

5.4.1 Introduction 114
5.4.2 Methods 115
5.4.3 Results/Discussion 116
Chapter 6: Conclusion 121
6.1 Summary and Key Findings 121
6.2 Future Work 122
References 125

LIST OF TABLES

Table 1	Table of	2
Table 2	Multivariable analysis of the coefficients from the linear mixed effects model for diffusion coefficient, $\langle D \rangle$, vessel size (VS), and average velocity (v_{avg})	74
Table 3	Multivariable analysis of the coefficients from the linear mixed effects model for diffusion coefficient, $\langle D \rangle$, vessel size (VS), and flow rate	75
Table 4	Summary of Patient Cohort.	99
Table 5	Summary of patient demographics and clinical characteristics.	99

LIST OF FIGURES

Figure 1	Schematic of the energy flow or radiance	9
Figure 2	Overview of diffuse correlation spectroscopy (DCS)	15
Figure 3	Picture of the DCS instrument cart on wheels	19
Figure 4	Schematic of the multi-tau scheme	21
Figure 5	Different types of DCS sensors uniquely designed for each application	22
Figure 6	Depiction of the momentum transfer in a scattering event.	25
Figure 7	DCS accuracy when simulated $g_1(\rho,\tau)$ data is fit with the constraint of g1(τ)> 0.01 or g1(τ)>0.4	41
Figure 8	Representative measured (solid) and fitted (dashed) g2(ρ,τ) curves at 1.5cm (left) and 6cm	42
Figure 9	Anatomical image of ASL-MRI mouse with one ROI (red) used to obtain a perfusion value of CBF concurrent with the region that DCS measures.	43
Figure 10	Intraclass correlation coefficient (ICC) for intra- and inter-user repeatability	44
Figure 11	In vitro DCS microfluidic phantom.	56
Figure 12	Verification with Intralipid.	62
Figure 13	Verification with whole blood.	63
Figure 14	Effects of hematocrit. DCS-measured blood flow index (BFI) versus hematocrit at five fixed flow velocities	65
Figure 15	Correcting for the effects of hematocrit.	65
Figure 16	Effect of sensor orientation and measurement repeatability.	70
Figure 17	Mean and standard error of the spatially-weighted diffusion coefficient ($\langle D \rangle$) vs the known average velocity (v_{avg}).	74

Figure 18	Mean and standard error of the spatially-weighted diffusion coefficient ($\langle D \rangle$) vs the known flow rate.	75
Figure 19	Mean and standard errors of the spatially-weighted diffusion coefficient ($\langle D \rangle$) vs the known average velocity (v_{avg}) for sickle cell anemic (yellow) blood and healthy (green) blood	79
Figure 20	Drawing of temporal and spatial/ensemble average.	84
Figure 21	Adapted from Prahl's IAD manual[1] on how to make the reflectance and transmittance measurements for a single integrating sphere.	87
Figure 22	Diffuse correlation spectroscopy (DCS) experimental setup	94
Figure 23	Effect of IT nicardipine on systemic blood pressure and heart rate	101
Figure 24	Latent class trajectory groups of relative changes in cerebral blood flow (rCBF) as a function of time post-IT nicardipine administration.	102
Figure 25	Relationship between micro and macrovascular blood flow.	103
Figure 26	Mean ± standard error in relative changes of cerebral blood flow (rCBF, %) as a function of time post-IT nicardipine administration	111
Figure 27	Mean ± standard error as a function of time for days 1 (a), 2 (b), 3 (c), and 7 (d) of nicardipine.	112
Figure 28	Relationship between DCS-measured BFI and TCD-measured mean blood flow velocity	113
Figure 29	Overview of absolute mean and standard error values for HbO, HbR, HbT, SO_2, OEF, absorption coefficient, and reduced scattering coefficient across days 1,2,3, and 7	117
Figure 30	Mean and standard error values of the ratio of ipsilateral divided by the contralateral side for HbO, HbR, HbT, SO_2, OEF, absorption coefficient, and reduced scattering coefficient	118

Figure 31	Overview of absolute mean and standard error values for HbO, HbR, HbT, SO_2, OEF, $CMRO_2$, absorption coefficient, and reduced scattering coefficient across days 1,2,3, and 7	119
Figure 32	Mean and standard error values of the ratio of ipsilateral divided by the contralateral side for HbO, HbR, HbT, SO_2, OEF, $CMRO_2$, absorption coefficient, and reduced scattering coefficient	120

LIST OF SYMBOLS AND ABBREVIATIONS

ACA	Anterior cerebral artery
ACom	Anterior communicating artery
APD	Avalanche photodiode
BFI	Blood flow index
BF	Blood flow
CBF	Cerebral blood flow
CCB	Calcium channel blocker
CSF	Cerebrospinal fluid
CT	Computed tomography
CW	Continuous wave
$CMRO_2$	Cerebral metabolic rate of oxygenation
CHOA	Children's Healthcare of Atlanta
CCC	Lin's concordance correlation coefficient
CDE	Correlation diffusion equation
CI	Confidence interval
CTE	Correlation transport equation
DCI	Delayed cerebral ischemia
DOS	Diffuse optical spectroscopy
DCE	Dynamic contrast-enhanced
DCS	Diffuse correlation spectroscopy
DSC	Dynamic susceptibility contrast
DE	Diffusion equation
EEG	Electroencephalography
EUH	Emory University Hospital
EVD	External ventricular drain
FD	Frequency domain
Gd	Gadolinium
H&H	Hunt and Hess
Hct	Hematocrit
HR	Heart rate
HbO	Oxygenated hemoglobin
HbR	Deoxygenated hemoglobin
HbT	Total hemoglobin
ICA	Internal carotid artery
ICP	Intracranial pressure
ICU	Intensive care unit
IT	Intrathecal
LCMM	Latent class mixture model
LME	Linear mixed effects model
MAP	Mean arterial pressure
MCA	Middle cerebral artery
mFG	Modified Fisher Grading scale
MRI	Magnetic resonance imaging
NIRS	Near infrared spectroscopy

NIR	Near infrared
OEF	Oxygen extraction fraction
PC	Phase contrast
PCom	Posterior communicating artery
PCI	Peripheral component interconnect
PET	Positron emission tomography
PICA	Posterior inferior cerebellar artery
rCBF	Relative change in cerebral blood flow
RTE	Radiative transport equation
SNR	Signal-to-noise ratio
SAH	Subarachnoid hemorrhage
SaO_2	Arterial oxygen saturation
SpO_2	Transcutaneous oxygen saturation
StO_2	Tissue oxygen saturation
Sup Cereb	Superior cerebellar artery
T1	Longitudinal relaxation time
T2	Transverse relaxation time
TCD	Transcranial Doppler ultrasound
TiO_2	Titanium dioxide
TD	Time domain
TTL	Transistor-Transistor Logic
WFNS	World Federation of Neurosurgical Societies

Symbol	**Quantity**	**Units**
n	Index of refraction	
c	Speed of light in vacuum	cm/s
v	Speed of light in tissue: v = c/n	cm/s
μ_a	Absorption coefficient	cm^{-1}
μ_s	Scattering coefficient	cm^{-1}
μ_s'	Reduced scattering coefficient	cm^{-1}
g	Anisotropy coefficient	
D	Diffusion coefficient	cm^2/s
g_1	Electric field autocorrelation function	
g_2	Temporal autocorrelation function	
τ	Delay time	s
α	Blood volume fraction	
D_B	Brownian diffusion coefficient	cm^2/s
BFI	DCS blood flow index; $BFI = \alpha D_B$	cm^2/s
λ	Wavelength	nm
ρ	Source-detector separation	cm
L	Radiance	$W/m^2/sr$
Φ	Fluence rate	W/m^2
F	Fluence	J/m^2

SUMMARY

Cerebral blood flow is an important biomarker of brain health and function. Numerous conditions, such as ischemic stroke and subarachnoid hemorrhage, are associated with compromised cerebral blood flow that, if left untreated, can lead to neuronal death and ultimately to significant adverse outcomes. To optimize clinical management after a brain injury, there is an unmet need for noninvasive modalities that can monitor cerebral perfusion for improved patient-centered care that prevents further brain injury. Diffuse correlation spectroscopy (DCS) is an emerging low-cost (<$50k) optical modality that can provide measurements of microvascular cerebral blood flow in a non-invasive and portable manner.

DCS measures an index of blood flow (BFI, cm^2/s). while BFI has been correlated *in vivo* with measurements of blood flow made with other perfusion modalities, the dependence of BFI on red blood cell properties (i.e., flow velocity, vessel size, hematocrit, and morphology) is less understood. The first aim of this dissertation focuses on the theoretical advancement of DCS by designing a novel microfluidic tissue-simulating phantom to explore the contribution of flow velocity, vessel size, and hematocrit on the measured DCS blood flow index, which to date has not been well defined. Understanding these influences will improve the accuracy of the DCS blood flow index and expand the clinical applications of DCS.

The second aim of this dissertation explores the translational potential of DCS measurements of microvascular cerebral perfusion in patients with subarachnoid hemorrhage (SAH). I demonstrate the clinical utility of these measurements by monitoring the CBF response to a commonly used vasodilatory treatment for SAH. The results

demonstrate that a lack of CBF response to this treatment is associated with development of a secondary stroke. Thus, the blood flow response to this treatment could be used as a novel early biomarker of poor outcome, alerting clinicians that alternative interventions are merited.

Chapter 1: Background

1.1 Importance of Cerebral Blood Flow

Although the human brain weighs less than 2% of the totally body weight, it consumes more than 20% of the body's energy. Adequate cerebral blood flow (CBF) is critical for delivery of oxygen and nutrients necessary to maintain neuronal health and function, and, ultimately, brain function and viability. Compromised blood flow may lead to dangerous clinical conditions in the brain, including stroke[2,3], hemorrhage[4], traumatic brain injury[5,6], hypoxic-ischemia[7–9], and hypertension[10,11]. These diseased states encompass not only significant reductions or elevations in flow, but also critical impairments in the autoregulatory and neurovascular coupling mechanisms that regulate vascular tone[12–14]. Thus, cerebral hemodynamics can serve as an informative biomarker of injury severity, progression, and mechanism.

1.2 Quantifying Cerebral Blood Flow with Current Imaging Modalities

Cerebral blood flow is typically quantified as a volumetric flow rate per 100g of brain tissue (units: mL/100g tissue/min). Normal CBF for healthy adults is ~50 mL/100g tissue/min[15]. After injury, such as in the case of traumatic brain injury or stroke, CBF can decrease to 20-40 mL/100g tissue/min[16,17]. If flow decreases lower than 20 mL/100g tissue/min, infarction occurs[18].

Currently, a handful of imaging modalities exist to quantify cerebral blood flow, such as magnetic resonance imaging (MRI)[19,20], nuclear medicine (PET, SPECT)[21,22], transcranial Doppler ultrasound (TCD)[23], and x-ray imaging coupled with a radioactive

tracer (e.g., Xenon-CT). The following sections summarize key advantages and disadvantages of these existing imaging modalities that measure CBF (Table 1)[12].

Table 1: Table of perfusion modalities available for clinical use

Imaging Modalities	**Invasiveness**	**Spatial Extent**	**Absolute Blood Flow**	**Continuous Measurements**	**Bedside**
Perfusion MRI	Non-invasive/ Invasive	Global	Absolute	Snapshot (repeatable)	No
PET/ SPECT	Invasive	Local	Relative/Absolute	Snapshot	No
Xenon-CT	Non-invasive	Local	Absolute	Snapshot	No
Doppler Ultrasound	Non-invasive	Local	Relative	Snapshot/ Continuous	Yes

1.2.1 Perfusion Magnetic Resonance Imaging

Magnetic resonance imaging (MRI) is an imaging modality that not only provides clear structural images of the whole brain but also is used for perfusion imaging. There are two main types of perfusion MRI techniques that have been developed using: 1) an endogenous contrast agent (arterial blood water) and 2) an exogenous, intravascular contrast agent (typically gadolinium)[24].

ASL-MRI uses the endogenous contrast provided by blood water protons as a diffusible tracer for high resolution (~mms) estimation of cerebral blood flow[25]. In ASL-MRI, a control image is first acquired without any arterial labeling. Next, there are three

types of ways in which the arterial protons can be magnetically labelled, usually in the neck for brain imaging: 1) continuous (CASL), 2) pulsed labeling (PASL), and 3) pseudo-continuous (pCASL)[26]. In the clinical setting, pCASL is the recommended ASL pulse sequencing method, due to its high labeling efficiency and straightforward data acquisition protocols[27]. Next, the protons are "labelled" as they pass through the labeling plane, typically applied at the base of the brain[28]. ASL-MRI measures the difference in the longitudinal relaxation time (T1) between the labeled and control images, which suppresses signal contribution from static tissue[26,29]. By solving the Bloch equations, which relate the dependence of brain water magnetization to blood flow[30], ASL-MRI reports voxel-wise values of CBF in units of mL/100g tissue/min.

Perfusion MRI can also be conducted by using an exogenous contrast agent. Both dynamic susceptibility contrast (DSC)-MRI and dynamic contrast-enhanced (DCE)-MRI use an intravenous bolus injection of gadolinium (Gd)-based contrast agent. In DSC-MRI, the Gd bolus is tracked and captured through a series of transverse relaxation time (T2)-weighted images, as the bolus traverses throughout the brain[31]. When plotting the signal intensity against time, there is a sharp decrease in the T2 signal intensity due to the contrast agent, known as the susceptibility effect. By using the principles of the indicator dilution theory, this signal information can be converted into the concentration of the contrast agent within a given volume of interest as a function of time to yield CBF[32]. In contrast, DCE-MRI involves the serial acquisition of longitudinal relaxation time (T1) images before, during, and after the Gd bolus injection. CBF is also quantified by fitting the concentration versus time curves, which are derived from the T1 signal intensities[33]. Both DSC-MRI and DCE-MRI correlate with each other[33]. However, DSC-MRI is more commonly used since

the postprocessing software is easy-to-use and widely available but provides regional variations in cerebral blood flow.

Finally, to complement ASL-MRI and DSC-MRI, another form of a non-invasive perfusion MRI method is phase contrast (PC)-MRI. PC-MRI measures the flow flux of the large feeding arteries in the brain (i.e., internal carotid and vertebral arteries) to quantify absolute values of whole-brain cerebral blood flow[34,35]. While PC-MRI cannot provide spatial information on blood flow distribution, PC-MRI can be used as a calibration factor for ASL-MRI and DSC-MRI, in times when quantification is confounded by factors such as labeling efficiency[36].

Ultimately, while ASL-MRI is non-invasive and requires no exogenous contrast agent or ionizing radiation, all three types of perfusion MRI offer only snapshot measurements in time while the patient is in the scanner, pose a financial burden, require anesthesia in children under 6yrs[37], which also introduces a confounding effect of sedation on CBF, and finally requires the patient to be transported to the scanner, which may pose complications and not be feasible to critically ill patients.

1.2.2 Nuclear Medicine (PET/SPECT)

Nuclear medicine is another imaging modality employed in the clinic to measure cerebral blood flow. Positron emission tomography (PET) utilizes a radioactive tracer to measure cerebral blood flow. The injected radionuclides decay via positron emission. When emitted positrons collide with nearby electrons in tissue, gamma rays are emitted that are picked up by detectors within the PET scanner[21]. In a PET scanner, detectors are located all around (360^{o}), resulting in improved sensitivity and uniformity and high spatial resolution[21]. While PET is typically used to measure the cerebral metabolic rate of glucose consumption in the

brain, PET with [^{15}O]-water as the radioactive tracer is commonly utilized to quantify cerebral blood flow[38,39]. Here, [^{15}O]-water is injected into the patient, and local CBF is quantified by utilizing Ficks law to fit the concentration of the radioactive tracer as a function of time curve for each volume of interest.

Single-photon emission computerized tomography (SPECT) is another nuclear medicine technique that uses gamma rays via a radioactive tracer to measure regional cerebral blood flow. While a SPECT scanner contains different hardware than a PET scanner (such as number of detectors), uses isotopes with longer half-lives, and produces lower quality spatial resolution images, both modalities have a similar overarching technique, which is injecting a radioactive tracer and measuring the tissue uptake by the brain to calculate cerebral blood flow. Overall, while PET/SPECT offer the advantage of individualized treatment from a patient's blood flow, it is cost prohibitive, and patients need to be wheeled to the scanner. Most importantly, nuclear medicine imaging results in exposure to radiation, preventing longitudinal monitoring as any amount of exposure to radiation increases a patient's lifetime risk of cancer.

1.2.3 Xenon-CT

Xenon-enhanced computed tomography (Xenon-CT) is a neuroimaging technique where a subject inhales nonradioactive Xenon-133 gas during CT image acquisition[40]. After Xenon-133 inhalation, a series of CT images are acquired at various timepoints to capture the Xenon clearance. The calculation of cerebral blood flow is accomplished by quantifying the rate of Xenon entry within each CT voxel in the brain from each sequential scan superimposed over the structural images[41–43]. The disadvantages to this modality are radiation exposure from CT scanner (X-rays) and the pharmacologic effects of Xenon-133

gas (i.e., alteration to the parts of the brain that interpret sensory stimuli resulting in uncontrollable patient motion)[40]. Both disadvantages prevent routine longitudinal monitoring in patients.

1.2.4 Transcranial Doppler Ultrasound

Transcranial Doppler ultrasound (TCD) provides the most feasible bedside tool for quantification of routine cerebral perfusion. TCD uses sound waves to measure the blood flow velocity in the large feeding vessels to the brain (e.g., middle cerebral artery and anterior cerebral artery)[44]. An ultrasound transducer placed on a bone sonographic window emits pulses of sound waves that are reflected by moving red blood cells in the brain. The change in frequency between the emitted and reflected ultrasound waves (i.e., Doppler shift) is directly proportional to the red blood cell velocity[23]. Given its relative ease of use, TCD has evolved to function as a diagnostic, monitoring, and therapeutic bedside tool. TCD is non-invasive, cost-effective, and provides real-time information about cerebral hemodynamics. However, TCD requires a skilled operator and only provides information on the macrovasculature, which may not be representative of the microvasculature in diseased states.

1.3 Diffuse Correlation Spectroscopy

Diffuse correlation spectroscopy (DCS), which is detailed in Chapter 2, is an emerging non-invasive optical modality that can estimate an index of microvascular blood flow from fast temporal intensity fluctuations in detected light that arise from the movement of red blood cells[45–47]. The advantages of DCS over other clinically available perfusion modalities, such as MRI, PET, or TCD, include high temporal resolution (>20 Hz), relatively low cost (<$50k), continuous bedside monitoring capabilities, and sensitivity to

the microvasculature. Further, it does not require exogenous contrast agents, ionizing radiation, or trained personnel. Moreover, blood flow measurements with DCS can be acquired rapidly (<1min) and do not require sedation in young children. This technique has shown promise in a wide array of clinical applications, including stroke[48–51], traumatic brain injury[52–55], and cardiac surgery[56–62].

1.4 Overview

Cerebral blood flow is an important biomarker of brain health and function. Compromised blood flow may lead to dangerous clinical conditions in the brain such as ischemic stroke and subarachnoid hemorrhage. These decreased cerebral blood flow values encompass vital impairments in the autoregulatory and neurovascular coupling mechanisms that regulate vascular tone. Thus, cerebral hemodynamics can serve as an informative biomarker of injury severity, progression, and mechanism.

My dissertation focuses on 1) the theoretical advancement of DCS by developing a novel microfluidic platform to explore the contribution of flow velocity, vessel size, and hematocrit on healthy and sickle cell blood, and 2) the clinical translation of diffuse correlation spectroscopy to measure subarachnoid hemorrhage patients during the intrathecal administration of the drug nicardipine.

Chapter 2 of this dissertation provides a theoretical background for DCS, as well as a description of the experimental setup used in the studies described herein. Chapter 3 explores the validity of DCS at small source-detector separations that are required when employing DCS in small animal models. The work in Chapter 3 was pivotal in guiding the experimental design in Chapter 4, wherein I present a novel *in vitro* microfluidic phantom for benchtop DCS experiments that requires the use of small source-detector separations.

In Chapter 4, I use this microfluidic phantom to systematically explore the influence of flow velocity, vessel size, hematocrit, and red blood cell morphology on the DCS-measured blood flow index. Finally, in Chapter 5, I demonstrate clinical utility of DCS measurements of microvascular cerebral perfusion in patients with subarachnoid hemorrhage in response to the vasodilator, nicardipine. Taken together, this work both advances the understanding of the blood flow index measured with DCS, as well as provides strong supporting evidence of the clinical value that DCS holds.

Chapter 2: Diffuse Correlation Spectroscopy

2.1 Radiative Transport Equation

Photon transport in biological tissue can be modeled analytically with the radiative transport equation (RTE). The radiative transport equation is a conservation equation that represents the conservation of energy of photons as they absorb, emit, and scatter while moving inside tissue. Radiance, $L(\vec{r}, \hat{s}, t)$ (units: W/m^2/sr), is the fundamental physical quantity that is conserved in the radiative transport equation and is defined as the flow of energy at location, $\vec{r}$, and direction, $\hat{s}$, and time, t, through a small area element dA within a small solid angle element, $d\Omega$ (Figure 1).

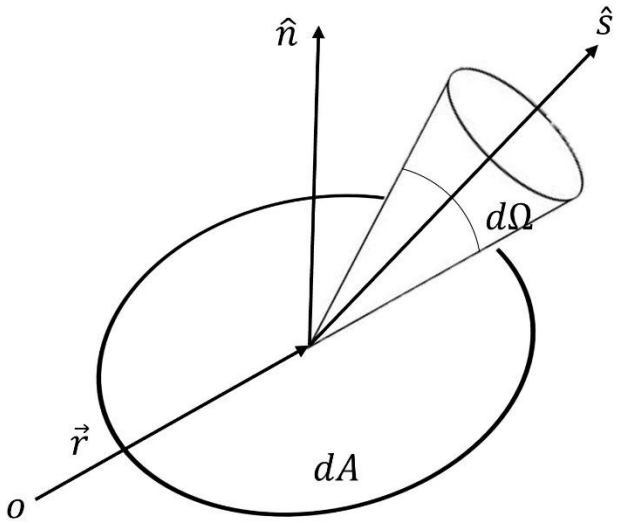

Figure 1: Schematic of the energy flow or radiance through a differential area element, dA, within a differential solid angle element, dΩ. Here, $\hat{n}$ denotes the unit outward normal vector of dA

Below, I will derive the RTE from the conservation of energy principle. The principle of the conservation of energy (P) says that:

$$dP = -dP_{div} - dP_{ext} + dP_{sca} + dP_{src} \quad (1)$$

Here:

$$dP = \frac{\partial L(\vec{r},\hat{s},t)/v}{\partial t} dV d\Omega, \tag{2}$$

which represents the change in energy in the volume (V) element within the solid angle (Ω) element per unit time. v is the speed of light. The energy diverging out of the volume element (dP_{div}) is given by:

$$dP_{div} = \hat{s} \cdot \nabla L(\vec{r},\hat{s},t) d\Omega dV. \tag{3}$$

The energy loss per unit time in the volume element within the solid angle element due to the contributions from absorption and scattering (dP_{ext}) is given by:

$$dP_{ext} = (\mu_t ds)[L(\vec{r},\hat{s},t) dA d\Omega]. \tag{4}$$

Here, $\mu_t ds$ is the extinction probability, and μ_t is the sum of the absorption and scattering coefficients (μ_a and μ_s, respectively). The energy incident on the volume element from any direction $\hat{s}'$ and scatters into $d\Omega$ (dP_{sca}) is given by:

$$dP_{sca} = (\mu_s dV) \left[\int_{4\pi} L(\vec{r},\hat{s}',t) P(\hat{s}' \cdot \hat{s}) d\Omega' \right] d\Omega. \tag{5}$$

Here, $P(\hat{s}' \cdot \hat{s})$ is the phase function, which depends on the angle between the scattered and incident directions. Specifically, the phase function can be thought of as a probability density: given that a photon arrives from direction, $\hat{s}'$, and is scattered, what is the probability that the scattered direction falls within $d\Omega$ centered on direction $\hat{s}$[63]. Finally,

source of the energy in the volume element within the solid angle element per unit time (dP_{src}) is given by:

$$dP_{src} = S(\vec{r}, \hat{s}, t) dV d\Omega. \quad (6)$$

Here, $S(\vec{r}, \hat{s}, t)$ has units of W/(m^3 sr).

Substituting equations (2) – (6) into equation (1), we arrive at the radiative transport equation:

$$\frac{\partial L(\vec{r},\hat{s},t)/v}{\partial t} = -\hat{s} \cdot \nabla L(\vec{r}, \hat{s}, t) - (\mu_t) L(\vec{r}, \hat{s}, t) + (\mu_s) \left[\int_{4\pi} L(\vec{r}, \hat{s}', t) P(\hat{s}' \cdot \hat{s}) d\Omega'\right] + S(\vec{r}, \hat{s}, t) \quad (7)$$

2.2 Photon Diffusion Equation

On its own, the radiative transport equation (Equation 7) is difficult to solve. However, by making several assumptions, it is possible to reduce the RTE to a diffusion equation, which can be readily solved for a variety of different geometries. Namely, in the diffusion approximation some of the assumptions is that $\mu_s \gg \mu_a$ and that the source-detector separation must be large in comparison to $1/\mu_s'$. These assumptions are easily satisfied in biological tissues. For example, in the brain, reduced scattering coefficient ($\mu_s' = \mu_s(1 - g)$, where g (anisotropy factor) is 0.9 in tissue), the scattering coefficient (μ_s), and the absorption coefficient (μ_a) are 10 cm^{-1}, 100 cm^{-1}, and 0.2 cm^{-1}, respectively[64].

In the diffusion approximation, the radiance is expanded in terms of spherical harmonics ($Y_{n,m}$) to the first order, which is known as the P_1 approximation:

$$L(\vec{r}, \hat{s}, t) \approx \sum_{n=0}^{1} \sum_{m=-n}^{n} L_{n,m}(\vec{r}, t)\, Y_{n,m}(\hat{s}), \quad (8)$$

where $L_{n,m}$ are the expansion coefficients. If the expansion of L continues to the upper limit of n=0 to n=N, then the approximation is known as the P_N approximation. Under the assumption that the scattering medium is nearly isotropic after sufficient scattering,

Equation 8 can be expanded and rewritten as a summation of the fluence rate ($\Phi(\vec{r},t)$) and the energy flux ($\vec{J}(\vec{r},t)$, units (W/m^2)) to be:

$$L(\vec{r},\hat{s},t) = \frac{1}{4\pi}\,\Phi(\vec{r},t) + \frac{3}{4\pi}\vec{J}(\vec{r},t)\cdot\hat{s} \tag{9}$$

where here $\Phi(\vec{r},t)$ is defined as:

$$\Phi(\vec{r},t) = \int_{4\pi} L(\vec{r},\hat{s},t)d\Omega\,. \tag{10}$$

This term is dubbed the fluence rate, which is the flow of energy per unit area integrated over the entire 4π solid angle (units: W/m^2). The second term on the right-hand side of Equation 9 is fluence ($\vec{J}(\vec{r},t)$), which is the photon flux.

Substituting Equation 9 into the RTE (Equation 7) and integrating over the 4π solid angle results in the following scalar differential equation:

$$\frac{d\Phi(\vec{r},t)}{vdt} + \mu_a\Phi(\vec{r},t) + \nabla\cdot\vec{J}(\vec{r},t) = S(\vec{r},t) \tag{11}$$

The steps below derive the scalar differential equation above:

1. $\int_{4\pi}\frac{\partial L(\vec{r},\hat{s},t)/v}{\partial t}\,d\Omega$ → With Equation 9 in mind, we know that the first term on the left-hand side of the RTE (Equation 7, *dP*) reduces to : $\boldsymbol{\frac{d\Phi(\vec{r},t)}{vdt}}$.

2. $\int_{-4\pi} -\hat{s}\cdot\nabla L(\vec{r},\hat{s},t)\,d\Omega$ → Due to the vector identities, $\hat{s}\cdot\nabla L = \nabla\cdot(\hat{s}L) - L\nabla\cdot\hat{s}$ and $\nabla\cdot\hat{s} = 0$, and that the energy flux is defined as $\vec{J}(\vec{r},t) = \int_{4\pi}\hat{s}L(\vec{r},\hat{s},t)\,d\Omega$,

then the divergence term reduces to: $\int_{-4\pi} -\hat{s} \cdot \nabla L(\vec{r},\hat{s},t)\, d\Omega = -\int_{-4\pi} \nabla \cdot \left(\hat{s}L(\vec{r},\hat{s},t)\right) d\Omega = -\nabla \cdot \int_{-4\pi}\left(\hat{s}L(\vec{r},\hat{s},t)\right) d\Omega = -\boldsymbol{\nabla \cdot \vec{J}(\vec{r},t)}$.

3. $\int_{-4\pi} -(\mu_t)L(\vec{r},\hat{s},t)\, d\Omega = -\boldsymbol{\mu_t \Phi(\vec{r},t)}$.

4. $\int_{-4\pi}(\mu_s)\left[\int_{4\pi} L(\vec{r},\hat{s}',t)P(\hat{s}'\cdot\hat{s})d\Omega'\right] d\Omega = \boldsymbol{\mu_s \Phi(\vec{r},t)}$.

5. $\int_{-4\pi} S(\vec{r},\hat{s},t)\, d\Omega = \boldsymbol{S(\vec{r},t)}$.

6. Combining all of the results from steps 1-5 and using the relation that $\mu_t = \mu_s + \mu_a$ forms the scalar differential equation.

The scalar differential equation has two variables: fluence rate (Φ) and the energy flux ($\vec{J}$). However, this form can be further reduced and rewritten in terms of fluence rate by assuming that the fractional change in the energy flux within one transport mean free path ($l_t' = \frac{1}{\mu_t'} = \frac{1}{\mu_a+\mu_s'}$) is small in comparison to the source-detector separation. Using this assumption, the energy flux term reduces to:

$$\vec{J}(\vec{r},t) = -D(\vec{r})\nabla\Phi(\vec{r},t), \tag{12}$$

Here, *D* is the diffusion coefficient:

$$D(\vec{r},\lambda) = \frac{1}{3(\mu_a(\vec{r},\lambda)+\mu_s'(\vec{r},\lambda))}. \tag{13}$$

Finally, if we substitute Equation (12) into the scalar differential equation (Equation 11), then we arrive at the final photon diffusion equation:

$$\frac{d\Phi(\vec{r},t)}{vdt} + \mu_a\Phi(\vec{r},t) - \nabla\cdot[D\nabla\Phi(\vec{r},t)] = S(\vec{r},t) \tag{14}$$

Furthermore, the photon diffusion equation can be reduced under the assumption that the diffusion coefficient (*D*) is space-invariant. This assumption means that while the optical

properties will change as a function of wavelength, they will be modeled as constants in space for each wavelength. Therefore, Equation 14 will reduce to:

$$\frac{d\Phi(\vec{r},t)}{vdt} + \mu_a\Phi(\vec{r},t) - D\nabla^2\Phi(\vec{r},t) = S(\vec{r},t) \quad (15)$$

2.3 Diffuse Correlation Spectroscopy

In DCS, coherent near-infrared light multiply scatters as it diffuses through tissue before detection at some distance away on the tissue surface (Figure 2). Light scattering off of moving red blood cells within the tissue leads to temporal fluctuations in detected light intensity measured by a remotely located detector on the tissue surface. These temporal fluctuations are quantified through a normalized temporal intensity autocorrelation function, $g_2(\tau)$, that is fit to simple analytical models, known collectively as the correlation diffusion theory (derived below)[47,65], to extract an index of blood flow (BFI, cm^2/s) of the underlying tissue. In general, BFI reflects the average flow velocity, density, and volume of red blood cells in the interrogated tissue volume[66]. Although the units of this blood flow index (cm^2/s) are not the traditional units of blood flow, numerous *in vivo* validation studies with DCS have shown that BFI strongly correlates with blood flow measured by various "gold standard" perfusion modalities[59,67–69].

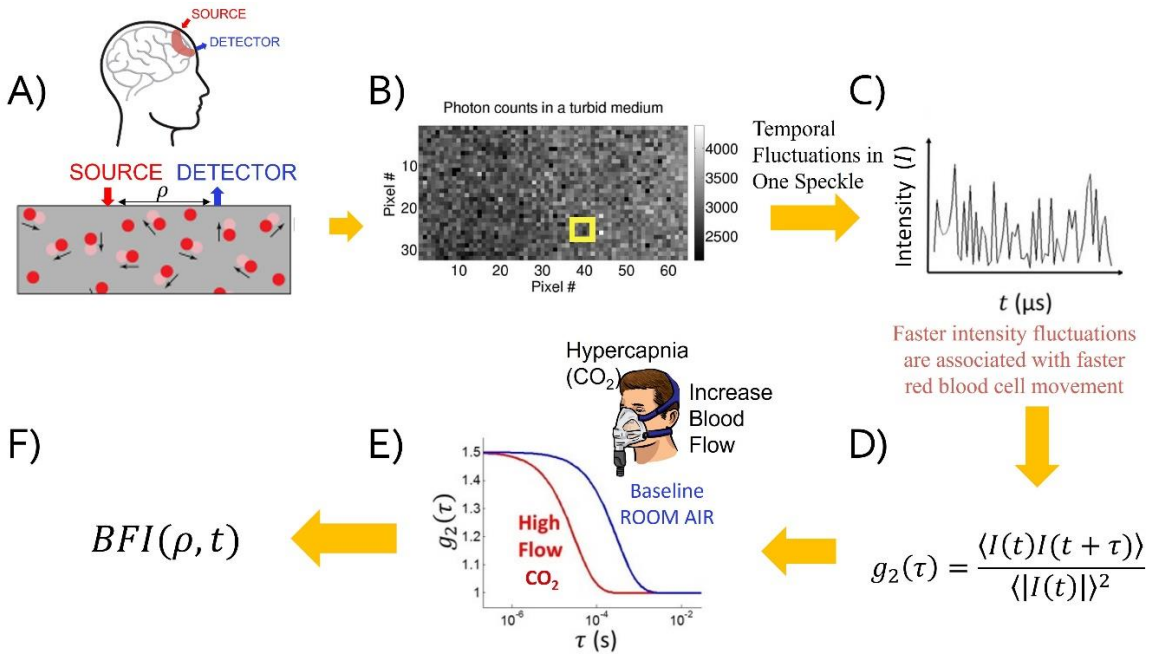

Figure 2: ***Overview of diffuse correlation spectroscopy (DCS) (A)*** *A coherent light source is placed on the tissue surface. Light is absorbed and scattered in tissue. A portion of light is detected by a detector place a distance, ρ, away,* ***(B)*** *A speckle pattern is generated as a result of the constructive and destructive interference of the moving scatterers (primarily red blood cells),* ***(C)*** *Scattering leads to temporal fluctuations in the speckle pattern. DCS measures these temporal fluctuations for a single speckle* ***(D)*** *An intensity autocorrelation function, $g_2(\tau)$, is used to quantify these temporal fluctuations,* ***(E)*** *The decay of this intensity autocorrelation function is related to the blood flow in the underlying tissue, with faster decays corresponding to faster flow,* ***(F)*** *To quantify blood flow, equation 19 relates the decay of the intensity autocorrelation function to the blood flow in the underlying tissue as a function of the source-detector separation, ρ, and time, t.*

2.4 Correlation Transfer Equation

In DCS, we experimentally measure the temporal fluctuations in detected light intensity, $I(\vec{r}, t)$, which is quantified with an intensity autocorrelation function, $g_2(\vec{r}, \tau) = \langle I(\vec{r}, t) I(\vec{r}, t+\tau)\rangle / \langle I(\vec{r}, t)\rangle^2$. The intensity autocorrelation can be related to the electric field (E) autocorrelation function, $g_1(\vec{r}, t, \tau) = \langle E^*(\vec{r}, t) \cdot E(\vec{r}, t+\tau)\rangle / \langle E(\vec{r}, t)\rangle^2$, via the Siegert relation[70]:

$$g_2(\vec{r}, t, \tau) = 1 + \beta |g_1(\vec{r}, t, \tau)|^2, \tag{16}$$

where β is a coherence factor that is dependent on the type of detection fiber used and is inversely proportional to the number of detected speckles[71].

Mathematically, it has been shown that the propagation of the electric field autocorrelation function, $G_1(\vec{r},t,\tau) = g_1(\vec{r},t,\tau) \times \langle E(\vec{r},t)\rangle^2$, diffuses through tissue in a manner that is similar to light fluence rate, which is dictated by a correlation transport equation (CTE) that takes a similar form as the radiative transport equation (RTE) that governs radiance (L)[72]. Both CTE and RTE are energy conservation equations that describe the conservation of G_1 and L within an infinitesimal volume element within the tissue[73]. Mathematically, the CTE takes on the same form as the RTE, but now all of the radiance terms (L) from the RTE are replaced with the propagation of the unnormalized electric field autocorrelation function, $G_1(\vec{r},\tau) = \langle E^*(\vec{r},t) \cdot E(\vec{r},t+\tau)\rangle$, through tissue at position, $\vec{r}$, and time, t. Therefore, the correlation transport equation is[72–75]:

$$\nabla \cdot G_1(\vec{r},\hat{s},\tau)\hat{s} = -\mu_t G_1(\vec{r},\hat{s},\tau) + \mu_s \int G_1(\vec{r},\hat{s},\tau) g_1^s(\vec{r},\hat{s},\hat{s}',\tau) P(\vec{r},\hat{s},\hat{s}') d\hat{s}' + S(\vec{r},\hat{s}) \quad (17)$$

Here, $G_1(\vec{r},\hat{s},\tau)$ is the unnormalized temporal field correlation function at delay time, τ, propagating in the $\hat{s}$ direction, $g_1^s(\vec{r},\hat{s},\hat{s}',\tau)$ is the normalized temporal field correlation function for single scattering, and $P(\hat{s},\hat{s}')$ is the normalized differential single scattering cross-section. Equation 17 is a steady-state equation independent of time, which means that this equation is only valid for continuous-wave DCS, i.e., when the light source is not pulsed or modulated. At a high-level, the correlation transport equation represents that the change in $G_1(\vec{r},\hat{s},\tau)$ is due to: 1) the losses from absorption and scattering within the solid angle element (first term, right-hand side), 2) the gain from $G_1(\vec{r},\hat{s},\tau)$ scattering into the

solid angle element (second term, right-hand side), and 3) gains from sources (third term, right-hand side).

2.5 Correlation Diffusion Equation

As is the case with the RTE, the CTE can only be solved numerically. To make the correlation transport equation more tractable, several assumptions are typically made that enable the problem to be solved analytically. By making the same assumptions as listed above when deriving photon diffusion equation from the radiative transport equation, the correlation transport equation (Equation 17) reduces to the correlation diffusion equation[73]:

$$\nabla \cdot \left(D(\lambda,\vec{r})\nabla G_1(\lambda,\vec{r},\tau)\right) - v\left(\mu_a(\lambda,\vec{r}) + \frac{P_{RBC}}{3}\mu_s'(\lambda,\vec{r})k_0^2(\lambda)\langle\Delta r^2(\tau)\rangle\right)G_1(\lambda,\vec{r},\tau) = v(\lambda)S(\lambda,\vec{r},t) \quad (18)$$

Here, $D(\lambda,\vec{r}) \cong 1/(3\mu_s'(\lambda,\vec{r}))$ is the photon diffusion coefficient in tissue (units: cm^{-1}), $\mu_s'(\lambda,\vec{r})$ is the reduced scattering coefficient (units: cm^{-1}) of tissue at position r and wavelength λ, τ is the autocorrelation delay time, *v* is the speed of light in tissue, $\mu_a(\lambda,\vec{r})$ is the absorption coefficient of tissue (units: cm^{-1}), P_{RBC} represents the fraction of light-scattering events from moving scatterers (e.g. red blood cells), $k_0 = 2\pi n/\lambda$ is the wavenumber of the light diffusing through the tissue, *n* is the index of refraction of tissue, λ is the wavelength of light (units: nm), $S(\vec{r},t)$ is the isotropic source term, and $\langle\Delta r^2(\tau)\rangle$ is the mean-square displacement of the moving scatterers, which in tissue are predominantly red blood cells. *A priori,* one would assume that red blood cells experience convective motion, such that the mean-square displacement would take the form of $\langle\Delta r^2(\tau)\rangle = \langle v^2\rangle\tau^2$, where $\langle v\rangle$ is the average red blood cell velocity. However, *in vivo,* we observe that the mean-square displacement is proportional to τ, not τ^2 [47]. This τ-dependence suggests a sensitivity to diffusive-like motion, i.e., $\langle\Delta r^2(\tau)\rangle = D_B\tau$, where D_B

is an effective Brownian diffusion coefficient (units: cm^2/s). D_B is dubbed an *effective* diffusion coefficient because it is measured *in vivo* to be several orders of magnitude larger than the Brownian diffusion coefficient of red blood cells given by the Einstein-Smoluchowski relation[76,77]. Recently, it has been proposed that this effective diffusion coefficient, D_B, that is embedded in the measured blood flow index likely reflects the shear-induced diffusion that red blood cells experience as they traverse through the microvasculature[78]. Shear-induced diffusion refers to the process by which red blood cells experience significant lateral displacement as they traverse the vasculature due to the hydrodynamic interactions with other particles in the presence of a shear flow under small Reynolds numbers[79–82].

Equation 18 can be readily solved for various boundary conditions. Traditionally, when DCS is used on the head, the tissue is modeled as a semi-infinite, homogenous medium[47]:

$$g_1(\rho,\tau) = \frac{\left[\frac{e^{K(\tau)r_1}}{r_1} - \frac{e^{K(\tau)r_2}}{r_2}\right]}{\left[\frac{e^{K(0)r_1}}{r_1} - \frac{e^{K(0)r_2}}{r_2}\right]}, \tag{19}$$

where $K(\tau)^2 = 3\mu_a(\lambda)\mu_s'(\lambda) + (\mu_s'(\lambda))^2 k_0^2 P_{RBC}\langle \Delta r^2(\tau)\rangle$, $r_1 = \sqrt{\rho^2 + z_0^2}$, $r_2 = \sqrt{\rho^2 + (z_0 + 2z_b)^2}$, $z_0 = 1/(\mu_s')$, $z_b = (\frac{2}{3\mu_s'})(\frac{1+R_{eff}}{1-R_{eff}})$, R_{eff}= 0.493[83] is the effective reflection coefficient, and ρ is the source-detector separation. In practice, we fit our measured $g_2(\rho,\tau)$ data to Equation 19 for $\langle \Delta r^2(\tau)\rangle$, which we define as the blood flow index (BFI, cm^2/s), using the Siegert relationship (Equation 16) [70]. Since the correlation diffusion equation is dependent on μ_a and μ_s, DCS analysis, therefore, either assumes optical properties from literature or derives these patient specific optical properties from concurrent frequency domain near-infrared spectroscopy measurements[84].

While there have been numerous validation studies[85] that show that modeling the tissue as a semi-infinite homogenous medium is a reasonable first-order approximation, this gross oversimplification of the head geometry can lead to significant signal contamination from extracerebral (scalp/skull) layers, particularly when the depth to the brain is non-negligible[86–88]. To minimize extracerebral signal contributions, multiple studies have highlighted the importance and validated the accuracy of multi-layered models that approximate the head as a series of infinite slabs to separate cerebral signal contributions from extracerebral artifacts[89–93]. I go into more detail on this muti-layered model in Chapter 4, Section 4.1.2 of this dissertation.

2.6 Diffuse Correlation Spectroscopy Instrumentation

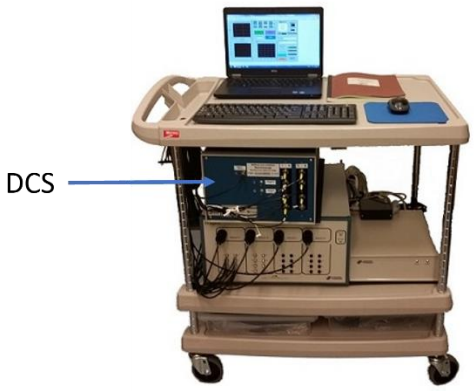

Figure 3: Picture of the DCS instrument cart on wheels

The sections below will describe the major components of the DCS instrumentation utilized for all the work described in this thesis (Figure 3) [94].

2.6.1 Lasers

Typically, for DCS, the light source operates in the near-infrared (NIR) because of the well-known spectral window that exists in the NIR regime where oxy- and

deoxyhemoglobin absorption (the main absorbers in the brain) are low and the reduced scattering is high, permitting light to diffuse deeply into tissue (up to several cm). while a similar window exists ~1100 nm, the lack of availability of detectors in this region have led most instruments to operate in the NIR[95].

Most importantly, the coherence length of the light source must be longer than the difference between the longest and shortest photon pathlengths in the tissue. The width of the pathlength distribution is approximated at 5 to 10 times the source detector separation[45,96]; typically, our largest source-detector separation is 2.5 cm, so the largest difference between the longest and shortest photon pathlengths a photon will take will be 25 cm. The equation for coherence length (L_{coh}) of a light source is:

$$L_{coh} = c\tau_{coh} = c/(\pi\Delta v), \tag{20}$$

where c is the speed of light (3e10 cm/s), τ_{coh} is the coherence time (s), and Δv is the linewidth (Hz) of the light source. For the laser used in all experiments described in this thesis (852 nm long coherence laser from Toptica (iBEAM smart, TOPTICA Photonics, Farmington, NY)), the linewidth is <15 MHz, corresponding to a coherence length of ~600 cm. Clearly, the coherence length of this laser (600 cm) is more than sufficient for our needs (25 cm). Recent work has been conducted into using a laser source with a lower coherence length, which effectively reduces the cost of the DCS laser from ~$10,000 to ~$100 and power consumption[97].

Finally, because the detection optics of our sensors utilize single mode ($\sim 5\mu m$ core diameter) fibers, it is imperative to increase the source power to the tissue as high as possible. However, we have to also keep skin exposure limits in consideration to be in compliance with ANSI standards for the maximum permissible exposure at 852 nm

according to FDA guidance[98–100]. Currently, the power output of our laser from the source is 120 mW, but we attenuated it to 60 mW to be in compliance with ANSI standards.

2.6.2 Correlator

In DCS, the detector fiber collects light that has traversed through the tissue. The photon counting avalanche photodiodes (SPCM-AQ4C-IO, Perkin-Elmer, Quebec, Canada) generate an electrical Transistor-Transistor Logic (TTL) digital pulse for each detected photon. These photon counts are used to estimate the normalized intensity autocorrelation function, $g_2(\tau)$, via either hardware or software correlator. The hardware correlator (Flex05-8ch, www.correlator.com, NJ) records the arrival of these TTL pulses and calculates $g_2(\tau)$ with a multi-tau scheme[101]. In this multi-tau scheme, there are groups consisting of 16 registers (note, that only the first group is 32 registers), whose bin width starts at 160 ns and doubles every 16 registers (Figure 4).

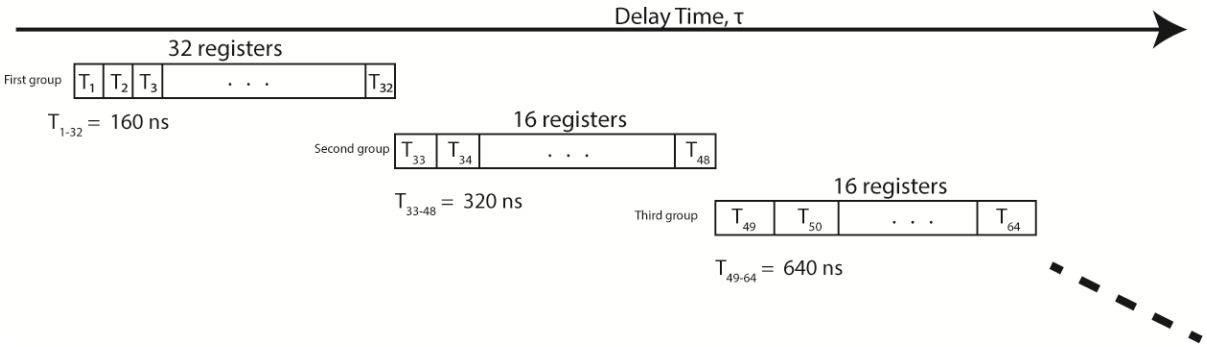

Figure 4: Schematic of the multi-tau scheme

Once the number of photons fill up each bin width in the time scheme, the register is shifted over to count new incoming photons. The photon counts in the registers are then used to generate a normalized intensity autocorrelation function, $g_2(\tau)$. The ensemble average is estimated over the entire acquisition time, t; in Chapters 3 and 4 of this thesis, $t = 3.33\ s$ or a 0.3 Hz acquisition rate. The delay time is calculated as the summation of all the bin

widths to the left of a specific register. For example, at the 40th register, the delay time would be: $\tau_{40} = 32\ bins \times 160\ ns + 8\ bins \times 320\ ns = 7.68\mu s$.

Recent advancements in DCS technology allow for acquisition at higher rates (up to 100 Hz) using a software correlator, such that a pulsatile blood flow waveform at the cardiac frequency can now be resolved[102]. Specifically, the software correlator utilizes the computer's peripheral component interconnect (PCI)-bus as a photon counter. We employ a counter/timer data acquisition board (PCIe-6612, National Instruments) and a custom software program on LabVIEW. This software correlator platform allows the user to specify not only the number of delay times but also the starting point of the first delay time. This versatility permits for shorter acquisition times. Chapter 5 of my dissertation on adult subarachnoid hemorrhage patients utilizes the software correlator, enabling me to capture the cerebral blood flow pulsatile waveform.

2.6.3 Sensor Design

For our DCS measurements, we designed custom-built sensors, where the source-detector separations were adjusted depending on the application (Figure 5).

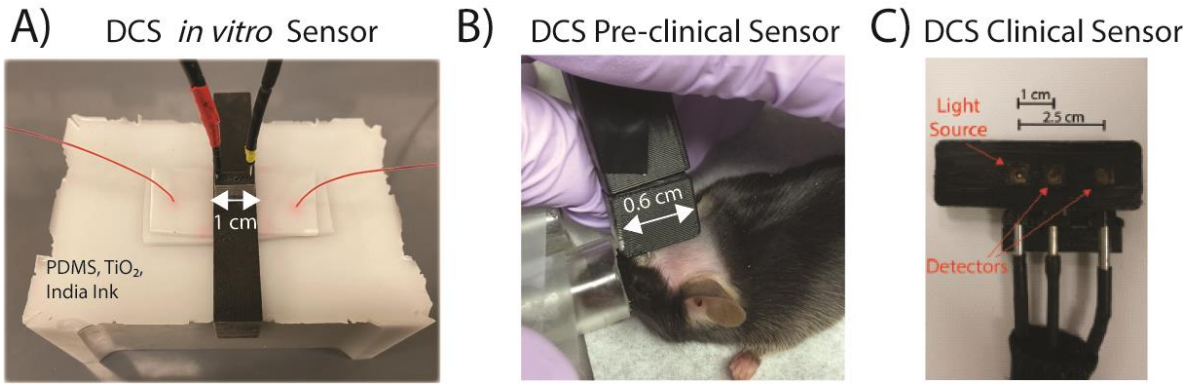

Figure 5: ***Different types of DCS sensors uniquely designed for each application (A)*** *A DCS sensor with a source-detector separation of 1 cm was designed for the in vitro microfluidic phantom project discussed in Chapter 4 of this thesis,* ***(B)*** *DCS sensor with a source-detector separation of 0.6 cm designed for measuring CBF in mice, as discussed*

*in Chapter 3 of this thesis, and **(C)** DCS sensor with two source-detector separations of 1 and 2.5 cm for application in the adult subarachnoid hemorrhage cohort, as discussed in Chapter 5 of this thesis.*

In Chapter 4 of this dissertation, for my microfluidic phantom experiments, I used a source-detector separation of 1 cm (Figure 5a)[92]. In Chapter 3 of this dissertation, I made DCS measurements on mice where we used a source-detector separation of 0.6 cm (Figure 5b)[103]. Finally, in Chapter 5 of this dissertation, I acquired DCS data in the adult subarachnoid hemorrhage population at two source-detector separations – 1 and 2.5 cm (Figure 5c); here, the shorter source-detector separation (1 cm) is meant to be sensitive to the extracerebral (scalp/skull) regions of the brain, while the longer source-detector separation (2.5 cm) is more sensitive to the brain. A bundle of single-mode detection FC fibers were connected to the DCS box from the sensor.

2.7 Monte Carlo Simulations

The Monte Carlo method numerically simulates photons propagating through biological tissue. The trajectory of each photon is modeled as a random walk in tissue, with the direction of each new step depending on the previous step. After simulating millions of photons, it is possible to estimate the momentum transfer of the detected photons and generate a normalized electric field autocorrelation function. Ultimately, Monte Carlo simulations provide us with an excellent computational model to replicate our *in vivo* and *in vitro* experiments. As previously described, in DCS, the correlation diffusion equation is derived from a series of assumptions from the radiative transport equation. Instead, Monte Carlo simulations abide by the radiative transport equation, which provides a "gold-standard" for how light propagates through tissue. This dissertation utilizes Monte Carlo

eXtreme for all simulations, due to its advantage of running simulations of millions of photons in under 10 minutes[104].

In Monte Carlo simulations, we define the thickness of the layers in our medium and assign the following optical properties for each layer: absorption coefficient (μ_a), scattering coefficient (μ_s), index of refraction (n), and anisotropy factor (g)[105]. These layers are infinitely wide and parallel to each other. Then, we specify the location of the source and the detectors. The source is an infinitely narrow photon beam that is perpendicularly incident to the specified medium. One benefit of Monte Carlo simulations is that we are able to set up multiple locations for the detectors to increase the number of photons detected, which is something that is not possible in the *in vivo* scenario due to the prohibitive cost from adding more detectors; typically, an array of 4 SPCM detectors are around $10,000. In a Monte Carlo simulation, millions of photons are launched from the source[105]. Next, each photon randomly moves step-by-step through the medium. For each voxel that the photon moves, the program calculates the scattering length (l) and absorption length of the photon, which is determined from the assigned absorption and scattering coefficients. The photon weight is decreased by $e^{-\mu_a l}$ to account for tissue absorption[105]. Photon propagation continues to be tracked until the photon is detected by a detector, absorbed, escapes the medium, or the time exceeds the set maximum time[73].

The outputs of the Monte Carlo simulations are the detected photons' pathlength and momentum transfer. Momentum transfer is defined as the change of the wavevector during a single scattering event, $\vec{q} = \vec{k}_{out} - \vec{k}_{in}$, where $\vec{k}_{out}$ and $\vec{k}_{in}$ are the incident and scattered wavevectors, respectively (Figure 6).

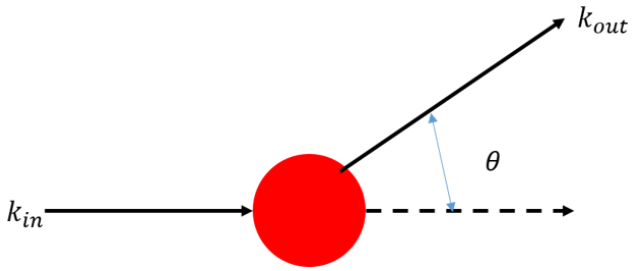

Figure 6: Depiction of the momentum transfer in a scattering event.

Here, $k = 2\pi n/\lambda$, where n is the index of refraction (n=1.4 for human tissue[83]) and λ is the wavelength of light. Also, in tissue, we assume only elastic scattering ($\left|\vec{k}_{out}\right| = \left|\vec{k}_{in}\right| = k_0$) takes place. In elastic scattering, there is no loss of energy; therefore, the elastically scattered electrons can change direction but do not change their wavelength ($\lambda = v/f$, where v is the velocity and f is frequency). For elastic scattering, the calculation of momentum transfer can be reduced to $|q| = 2|k_0|\sin(\frac{\theta}{2})$.

The detected photons' pathlength or momentum transfer are used to estimate the normalized electric field autocorrelation function ($g_1(\tau)$)[101]. However, using pathlength to estimate the autocorrelation function relies on the assumption that photons experience a large number of scattering events before detection. This assumption is not relevant when using momentum transfer, as it's valid in both diffusive and non-diffusive regimes[65]. Therefore, the electric field autocorrelation field function was computed using the total momentum transfer of the detected photons[101]:

$$g_{1,MC}(\tau) = \prod_i e^{-\frac{1}{3}k_0^2 Y(i)\langle \Delta r^2(\tau)\rangle_i} = e^{-\frac{1}{3}k_0^2 \sum_i Y(i)\langle \Delta r^2(\tau)\rangle_i}, \quad (21)$$

where the product and summation are for all tissue types, k_o is the light wavenumber in the medium, Y_i is the total dimensionless momentum transfer for the i[th] detected photon,

$\langle \Delta r^2(\tau) \rangle$ is the mean-square particle displacement at delay time, τ. In this model, we assumed that the mean-square displacement of the moving scatterers will follow diffusive motion such that $\langle \Delta r^2(\tau) \rangle = 6D_B\tau$, where D_B is the effective Brownian diffusion coefficient[85]. Since the output of the Monte Carlo simulation is the momentum transfer, to generate the electric field autocorrelation curve we need to assign a value for D_B, based on previously published values (~0.5 – 10 e-8 cm^2/s)[76].

After generating the $g_{1,MC}(\tau)$ curve, we fit the curve to the semi-infinite solution of the correlation diffusion equation (Equation 19) and solve for D_B.

Chapter 3: Exploring the Validity of the Correlation Diffusion Equation at Small Source-Detector Separations

3.1 Introduction

Adequate cerebral blood flow (CBF) is critical for delivery of oxygen and nutrients necessary to maintain neuronal health and function. Abnormalities in blood perfusion are seen in numerous diseased states, including stroke[2,3], hemorrhage[4], traumatic brain injury[5,6], hypoxic-ischemia[7–9], and hypertension[10,11]. These abnormalities encompass not only significant reductions or elevations in flow, but also vital impairments in the autoregulatory and neurovascular coupling mechanisms that regulate vascular tone[12–14]. Thus, cerebral hemodynamics can serve as an informative biomarker of injury severity, progression, and mechanism.

Preclinical models provide an invaluable tool to explore mechanisms underlying cerebral blood flow regulation, in addition to enabling the development of novel therapeutic strategies that restore perfusion and improve outcome after injury. Rodent (particularly rat and mouse) models are especially appealing given the wide range of genetically modified strains available and the relatively low cost compared to other large animal models. Currently, a handful of techniques exist to enable quantification of cerebral blood flow in small animal models including autoradiography[106,107], perfusion magnetic resonance imaging (MRI)[108], laser Doppler flowmetry (LDF)[109–111], laser speckle contrast imaging (LSCI)[112,113], and micro-ultrasound[114]. While each technique certainly has its own advantages, numerous limitations remain, including the need for radioactive material (autoradiography), poor spatial resolution (LDF), low SNR (MRI), limited depth

penetration (LSCI), and sensitivity to *macro*vascular blood flow velocity instead of microvascular blood flow (ultrasound).

Diffuse correlation spectroscopy (DCS)[47,71,85,115] is an emerging optical modality that has shown promise to non-invasively measure CBF in small animal models[116–122]. In DCS, coherent near-infrared (NIR) light multiply scatters as it diffuses through scalp, skull, and brain before detection at some distance away on the tissue surface. Scattering off moving red blood cells within the tissue leads to temporal fluctuations in the detected light intensity. These temporal fluctuations are quantified through a temporal intensity autocorrelation function, $g_2(\tau)$; $g_2(\tau)$ is then fit to simple analytical models, known as correlation diffusion theory[46,47], to extract a cerebral blood flow index (CBF_i). This CBF_i represents a bulk average of the microvascular flow in the "banana-shaped" region that spans from the source to the detector[47,85]. DCS offers several advantages over other blood flow modalities used in small animals described above. Most importantly, in contrast to autoradiography, laser speckle contrast imaging, and laser Doppler flowmetry, DCS measurements are non-invasive, as data acquisition does not involve animal sacrifice or even resection of the scalp or thinning of the skull, thus enabling longitudinal monitoring of cerebral blood flow within the same animal. Further, the instrumentation is relatively inexpensive (~$50k) and data can be obtained relatively quickly (<1 min) under light anesthesia or even in awake animals[120,123]. Moreover, DCS appears to be sensitive to perfusion in the microvasculature, i.e., capillaries, arterioles, and venules[71,76] in contrast to techniques like Doppler ultrasound[23] that measure flow velocity in large feeding arteries.

The correlation diffusion models used in DCS are predicated on the assumption that the source detector separation is greater than the transport mean free path, $\ell^* \equiv 1/\mu_s'$[47,124].

Thus, for typical brain tissue with μ_s' ~10cm^{-1}, source detector separations >> 0.3cm are needed to ensure the validity of these models. In humans and large animal models, this requirement is easily met, as large source detector separations of > 1cm [125,126] are routinely employed given the depth to the cortex. Indeed, numerous validation studies performed with large source detector separations have demonstrated excellent agreement between DCS and other *in vivo* CBF modalities i.e. MRI[48,58,59,67,126,127], microspheres[69], perfusion CT[55,89], indocyanine green (ICG) tracers[128], and transcranial Doppler[129–132]. However, in small animal models wherein the skull and scalp are ~0.1-0.2cm[133] and the brain itself is only about 1-2cm thick, source detector separations of 0.3-1cm are needed for depth penetration to cortical microvasculature.

Herein, we explore the validity of the diffusion approximation at small source-detector separations (<1cm) required to probe brain tissue in small animal models. We utilize a series of *in silico, in vitro,* and *in vivo* experiments to characterize the accuracy, validity, and repeatability of utilizing the correlation diffusion theory to analyze DCS data taken at source-detector separations of 0.3-1cm. Further, we explore the effects of constraining the fit of $g_2(\tau)$ to early delay times to minimize signal contributions from photons that have traveled shorter paths and to thereby improve accuracy when employing the diffusion approximation. We note that the results from these analyses may be generalized beyond small animal cerebral blood flow studies to any application of DCS wherein the desired penetration depth dictates the use of small source-detector separations[103].

3.2 Materials and Methods

In Silico Verification using Monte Carlo Simulations

Monte Carlo simulations were used for computational verification of DCS at small (< 1 cm) source-detector separations. Monte Carlo eXtreme (MCX) was used for all simulations[104]. For each simulation, we launched 500 million photons, which took <10 min on a NVIDIA Quadro P600. Using a 6cm x 6cm x 6cm semi-infinite medium with anisotropic factor (g) of 0.9 and index of refraction (n) of 1.4 to mimic biological tissue, we ran a total of 784 unique simulations for 14 source-detector separations (ρ), 7 absorption coefficients (μ_a), and 8 reduced scattering coefficients (μ_s') (14 separations × 7 μ_a × 8 μ_s' = 784 unique simulations). Separations ranged from 0.1 to 2 cm (0.1, 0.2, 0.3, 0.4, 0.5, 0.6, 0.7, 0.8, 0.9, 1, 1.2, 1.5, 1.8, 2cm), μ_a ranged from 0.05 to 0.35cm^{-1} in steps of 0.05cm^{-1}, and μ_s' ranged from 3 to 15cm^{-1} (3, 5, 7, 9, 10, 11, 13, 15 cm^{-1}). From each simulation, MCX records a list of all the detected photons with their individual pathlengths and number of random walk steps. Separate simulations were run for each source-detector separation to avoid absorption by a proximal detector. For each simulation, the detected normalized electric field autocorrelation function,$g_1(\rho,\tau)$, was computed using the total momentum transfer of the detected photons[66]:

$$g_1(\rho,\tau) = \frac{\sum_{i=1}^{N_p} e^{-\frac{1}{3}Y_i k_0^2 \left\langle \Delta r^2(\tau) \right\rangle} e^{-\mu_a L_i}}{\sum_{i=1}^{N_p} e^{-\frac{1}{3}Y_i k_0^2 \left\langle \Delta r^2(0) \right\rangle} e^{-\mu_a L_i}}, \tag{22}$$

where N_p is the number of detected photons, Y_i is the total dimensionless momentum transfer for the ith detected photons, L_i is the total pathlength traveled by the ith detected photon, k_o is the light wavenumber in the medium ($k_o = 2\pi n/\lambda$), λ is the wavelength of light (set to 852nm to match our experimental setup), and $\langle \Delta r^2(\tau) \rangle$ is the mean-square particle displacement at time, τ [46,66]. Here, we assumed Brownian motion of the moving scatterers

such that $\langle \Delta r^2(\tau) \rangle = 6D_B\tau$, where D_B is the Brownian diffusion coefficient[85]. For each of the 784 simulations, we computed $g_1(\rho,\tau)$ for 6 different physiologically realistic D_B values seen experimentally (denoted below as $D_{B,known}$), ranging from $0.5\text{x}10^{-8}$ to $3\text{x}10^{-8}$ cm^2/s in steps of $0.5\text{x}10^{-8}$ cm^2/s. Thus, in total we simulated 4704 $g_1(\rho,\tau)$ curves (784 simulations $\times$ 6 D_B per simulation).

To estimate the accuracy of DCS, each simulated $g_1(\rho,\tau)$ dataset was fit for D_B (denoted $D_{B,fit}$) using the semi-infinite solution to the correlation diffusion equation[47]:

$$g_1(\rho,\tau) = \frac{\left[\frac{e^{K(\tau)r_1}}{r_1} - \frac{e^{K(\tau)r_2}}{r_2}\right]}{\left[\frac{e^{K(0)r_1}}{r_1} - \frac{e^{K(0)r_2}}{r_2}\right]}, \tag{23}$$

where $K(\tau)^2 = 3\mu_a(\lambda)\mu_s'(\lambda) + \mu_s'(\lambda)^2 k_0^2 \alpha \langle \Delta r^2(\tau) \rangle$, $r_1 = \sqrt{\rho^2 + z_0^2}$, $r_2 = \sqrt{\rho^2 + (z_0 + 2z_b)^2}$, $z_0 = 1/\mu_s'$, $z_b = 2(1+R_{eff})/(3\mu_s'(1-R_{eff}))$, $R_{eff} = 0.493$[83] is the effective reflection coefficient, and α is the fraction of scattering events that occur from moving scatterers in the medium (assumed to be 1 for these simulations). Error in D_B for each simulated $g_1(\rho,\tau)$ curve was defined as $(D_{B,fit} - D_{B,known})/D_{B,known} \times 100\%$.

Further, because we are often interested in how blood flow changes over time, we also estimated how errors in D_B get translated to errors in relative change in D_B (rD_B). For each D_B, we characterized a range of physiologically realistic relative changes in blood flow ranging from -90% to 200% of the baseline D_B value (denoted $D_{B0,known}$). Error in the relative change in D_B was estimated as $(rD_{B,fit} - rD_{B,known})/rD_{B,known} \times 100\ (\%)$, where $rD_{B,known}$ is the simulated relative change in D_B from $D_{B0,known}$ to $D_{Bi,known}$, $rD_{B,fit} = (D_{B0,fit} - D_{Bi,fit})/D_{B0,fit} \times 100\%$, and $D_{B0,fit}$ and $D_{Bi,fit}$ denote the best fit values using the semi-infinite

correlation diffusion equation solution to the simulated data from $D_{B0,known}$ and $D_{Bi,known}$, respectively.

DCS Acquisition and Analysis

For experimental verification of DCS at small SDS reflectance geometries, we used a custom-built DCS instrument, comprised of an 852-nm long coherence length laser (iBeam smart, TOPTICA Photonics, Farmington, NY), a photon counting avalanche photodiode (SPCM-AQ4C-IO, Perkin-Elmer, Quebec, Canada), and a hardware autocorrelator board (Flex05-8ch, www.correlator.com, NJ). For all *in vitro* and *in vivo* experiments described herein, we utilized a custom optical sensor consisting of a 1 mm source comprised of a tightly packed bundle of 50μm multi-mode fibers (NA = 0.66, FTIIG23767, Fiberoptics Technology, Pomfret, CT) spaced 0.6cm away from a single-mode detection fiber (780HP, Thorlabs, Newton, NJ).

Experimentally, DCS measures the normalized intensity autocorrelation function, $g_2(\tau)$. The Siegert relation[70] was used to convert this measured $g_2(\tau)$ to $g_1(\tau)$; Equation (23) was then used to fit $g_1(\tau)$ for αD_B. Fits were constrained to $g_1(\tau) > 0.01$. Secondary analysis constrained fits to $g_1(\tau) > 0.4$ to explore the effect of this cutoff on DCS validity[134]. *In vitro*, we assume $\alpha = 1$, and *in vivo*, we define αD_B to be the cerebral blood flow index, or CBF_i, as this parameter characterizes the dynamics of the interrogated tissue. These fits require knowledge of the absorption and scattering properties of the medium at 852nm. *In vitro*, we estimated μ_a and μ_s' of the homogenous liquid phantoms using multi-distance (1.5, 2, 2.5, and 3cm) frequency-domain near infrared spectroscopy (Imagent, ISS, Champaign, Illinois) as in [58]. *In vivo*, we assumed values of $\mu_a = 0.25\ cm^{-1}$ and $\mu_s' = 7\ cm^{-1}$ for mouse brain[135].

In vitro Phantom Verification

For benchtop verification of DCS, we compared the measured D_B at a large source-detector separation (1.5 cm) where diffusion theory holds true to a small separation (0.6 cm) commonly used in rodent brain studies[120,123]. Two (3 L) homogenous liquid phantoms of differing reduced scattering coefficients were used. Phantoms were held in a (28x17x14cm) container and consisted of 20% Intralipid® (Fresenius Kabi, Lake Zurich, IL) and India Ink (Higgins®, Chartpak, MA) for scattering and absorption contrast, respectively. The measured optical properties at 852 nm of each phantom were $\mu_s' = 10\ cm^{-1}$, $\mu_a = 0.12\ cm^{-1}$ and $\mu_s' = 4.6\ cm^{-1}$, $\mu_a = 0.12\ cm^{-1}$, respectively. To manipulate D_B in these phantoms, temperature was varied slowly from 6 to 70°C. DCS measurements were made periodically in 2–3°C increments. At every temperature increment, acquired measurements were repeated three times at each source-detector separation, and the measurement order for 0.6 and 1.5cm was randomized. Temperature differences between the two source-detector separation measurements were < 0.5°C at any given temperature increment.

In vivo Verification against ASL-MRI

We validated DCS-measured CBF_i against blood flow measured by Arterial spin labeling (ASL) MRI in a mouse model[30,136]. All animal procedures were approved by Emory University Institutional Animal Care and Use Committee and followed the NIH Guidelines for the Care and Use of Laboratory Animals. Adult male C57BL/6 mice (n=9) were induced with 4.5% isoflurane for 45s and maintained at 1.8% isoflurane (1L/min, 70% nitrous oxide, 30% oxygen mixture) in a stereotaxic holder for the duration of the study. Body temperature and respiration rate were monitored and maintained at 36.5°C and 75-90 breaths per minute, respectively. Depilatory cream was used to remove hair from the

scalp to ensure adequate signal-to-noise for DCS measurements. Once stabilized, animals were placed in the MRI scanner and imaged for ~40 minutes (see Section 2.4.1), at which time the mouse was immediately taken out of the scanner for DCS acquisition to ensure measurements are made under approximately the same physiological conditions.

For DCS measurements, the optical sensor was gently placed over the intact scalp such that the source and detector fibers aligned with the parasagittal plane (source fiber approximately at bregma -1, 3 mm mediolateral). DCS data was acquired for five seconds over each hemisphere; measurements were repeated 3x/hemisphere and averaged to yield a mean CBF_i for the right and left hemisphere. DCS data was rejected from analysis if the intensity (*i.e.* photon count rate) was less than 30 kHz, or if the coefficient of variation (COV) was greater than 20%, where COV was defined as the standard deviation / mean CBF_i across multiple repetitions on a given hemisphere.

We note that in order to obtain a wide range of blood flow for DCS validation, a closed head injury model (described in depth in Buckley *et al.*[121]) was used in a subset of n=2 mice to produce a mild traumatic brain injury 4 hours prior to imaging. This injury paradigm has been shown to decrease blood flow by ~30% at 4 hours post-injury. Theses studies were approved by Emory IACUC.

ASL-MRI Acquisition and Analysis

MRI measurements were performed using a 9.4 T/20 cm horizontal bore Bruker magnet, interfaced to an Avance console (Bruker, Billerica, MA, USA). A two-coil actively decoupled imaging set-up was used (a 2 cm diameter surface coil for reception and a 7.2 cm diameter volume coil for transmission). Sagittal T2-weighted anatomical reference images were acquired with a RARE (Rapid Acquisiton with Refocused Echos) sequence

for the slice localization of interest. Slice location was chosen to encompass the sagittal plane that spanned the midpoint between the DCS source and detector. Imaging parameters were as follows: TR = 1800 ms, Eff.TE = 45 ms, RARE factor = 8; field of view (FOV) =38.4 x 19.2 mm^2, matrix = 256 x 128, Avg =4, slice thickness (thk) = 0.7 mm. Perfusion images were acquired with the vendor provided ASL protocol using a flow-sensitive alternating inversion recovery (FAIR) technique and a RARE sequence. Imaging parameters were as follows: TR = 18000 ms, Eff.TE = 20 ms; RARE factor = 8, FOV = 26.6 x 16 mm^2, matrix = 64 x 40, Avg =1, thk = 1 mm, number of TIR (inversion recovery time) = 8 (30, 200, 600, 1200, 2400, 4000, 6000, 10000 ms). Paired images were acquired alternately with and without arterial spin labeling. Anatomical T2-weighted images were acquired on the same slice of the perfusion image with a RARE (Rapid Acquisition with Refocused Echoes) sequence Imaging parameters were as follows: TR = 4000 ms, Eff.TE = 40 ms, RARE factor = 8, Avg =4, The FOV, matrix, and slice thickness were the same as the perfusion image.

In the FAIR technique[136,137], two inversion recovery images are acquired- non-slice-selective and slice-selective inversion pulses- in an interleaved fashion. The longitudinal magnetization after both a selective (ss) and nonselective (ns) inversion pulse can be defined as:

$$M_{ns} = M_0(1-2e^{-\frac{TI}{T_1}}), \tag{24}$$

$$M_{ss} = M_0(1-2e^{-\frac{TI}{T_1^*}}), \tag{25}$$

Here M_0 is the fully relaxed longitudinal magnetization of the tissue-water proton, T_1 is the longitudinal magnetization time of tissue-water proton, T_1^* is the apparent longitudinal

relaxation time, and TI is the inversion time. From the non-slice-selective and slice-selective inversion pulses, the values for M_{ns}, M_{ss}, and TI are known; thus, we solved for T_1, T_1^*, and M_0 through systems of equations. After obtaining the values for T_1 and T_1^*, it is possible to calculate for blood flow, f (mL/min/100g), with the equation[136,137]:

$$\frac{1}{T_1^*} = \frac{1}{T_1} + \frac{f}{\lambda}, \tag{26}$$

where we assume the tissue-to-blood partition coefficient, λ, is 90 mL/100g[138].

To compare flow measured with ASL-MRI to CBF_i measured with DCS, ROIs were chosen to roughly encompass the region of tissue probed by DCS (~0.2cm into the cortex) while balancing the need for sufficient ASL SNR within the ROI. We selected two 5-sided polygon ROIs that encompassed the right and left superior quadrants to either side of the midline using the *roipoly.m* function in Matlab. ROIs were chosen such 2 of the legs had dimensions of 0.48 and 0.28 cm. Average M_{ns} and M_{ss} within each ROI was computed for all TI, and Equations 25 and 26 were used to compute a mean ROI flow for comparison to DCS.

Small separation DCS Repeatability

Given the known effects of sensor position (i.e. regional inhomogeneity under the tissue surface) and pressure (i.e. changes in scalp flow during compression) on DCS repeatability at large separations[131,139], we next estimated small separation DCS repeatability through both an *in vivo* mouse model and an *in vitro* liquid phantom model, which served as a control experiment.

For *in vitro* repeatability assessment, DCS measurements were made by manually holding the optical sensor over two predefined locations marked on a container that held a

liquid phantom consisting of 1.58 μm diameter microspheres suspended in water (μ_s'(852nm) = 5.68 cm^{-1}, Bangs Laboratories Inc.). Three users acquired three repetitions per location, and the resultant curves were average to yield a mean and standard deviation D_B value at each location.

For *in vivo* repeatability assessment, adult C57BL/6 mice (n=10) were induced with 4.5% isoflurane for 1 minute and maintained at 1.5% isoflurane (1L/min, 70/30 nitrous oxide/oxygen mixture). After stabilization, 3 users each took 3 DCS measurements on each hemisphere by gently resting the sensor on the animal's head. Measurements were acquired once a day for 3 days. To account for blood flow measurement changes among users due to time differences between measurements and anesthesia depth, the order between the three users was randomized per hemisphere. The measurements on each hemisphere from each user, were averaged to yield a mean (standard deviation) cerebral blood flow index per hemisphere per animal.

Statistical Analysis

For *in vitro* phantom verification, Lin's concordance correlation coefficient (CCC) [140] was used to quantify the agreement between the Brownian diffusion coefficient measured at a small source detector separation ($D_{B,0.6cm}$) to that of a large source detector separation ($D_{B,1.5cm}$). Further, as a graphical means for assessing agreement between small and large separation measurements, Bland-Altman plots of the difference versus the mean of the small and large separation data were generated[141].

For ASL-MRI and DCS *in vivo* validation, linear regression analysis was performed to quantify any significant relationship between blood flow measurements from DCS and ASL-MRI. Pearson's correlation coefficient, R, was used to quantify the extent to which a

linear model explains variability in the data. All regression analyses were performed using R statistical software (R Foundation for Statistical Computing). Hypotheses tests and associated p-values were two sided. Statistical significance was declared for p-values < 0.05.

Finally, an intraclass correlation coefficient (ICC) [142,143] was used to assess both *intra*- and *inter*-user reliability of small separation DCS measurements. We used a two-way random effects model for ICC that treats users as random samples from the population of users and the experimental model (i.e. mouse and liquid phantom) as random samples from the experimental population. ICC was calculated using absolute agreement as a more conservative estimate of repeatability of DCS. ICC within a single user or across multiple users indicates the amount of experimental error that can be attributed to variation specific to the experimental model relative to the total variation in the measurements. Ideally, we would want both intra-user and inter-user measurements to have an ICC close to 1, indicating that the total variation is solely due to experimental model variability. Based off published values, ICC values greater than 0.75 are classified as excellent repeatability, ICC between 0.6 and 0.74 are classified as good repeatability, between 0.4 and 0.59 are classified as fair, and less than 0.4 are classified as poor reliability[143].

3.3 Results

In Silico Monte Carlo Verification

Representative Monte Carlo simulated $g_1(\rho,\tau)$ curves along with the best fit lines using the semi-infinite solution to the correlation diffusion equation are shown in Figure 7a,b. As source detector separation decreased, the deviation of the diffusion approximation fit from the simulated $g_1(\rho,\tau)$ becomes more apparent. Fits improve when constraining $g_1(\rho,\tau)>0.4$

(Figure 7b). At typical optical properties seen in brain tissue (μ_s'=10cm^{-1}, μ_a=0.2cm^{-1}), the error in estimating D_B using the diffusion approximation was <12% at source-detector separations greater than 0.2cm (Figure 7c). By constraining fits to where $g_1(\rho,\tau)>0.4$, the error is slightly reduced to <10% at source-detector separations > 0.2cm (Figure 7d). As expected, at large source-detector separations (> 1.5cm) the error in D_B was small (< 1%). The error in D_B was independent of $D_{B,known}$; however, error was heavily influenced by μ_a and μ_s'. To demonstrate the effects of μ_a and μ_s' on the error in D_B, Figure 7e depicts error in $D_{B,known}$ ($1x10^{-8}$ cm^2/s) at a source-detector separation of 0.6cm, as a function of absorbance and scattering. The highest error in D_B (~28%) was observed at the highest simulated μ_a (0.35cm^{-1}) and lowest simulated μ_s' (3cm^{-1}); error then decreases as μ_a decreases and μ_s' increases. Again, by constraining $g_1(\rho,\tau)$ fits to $g_1(\rho,\tau)>0.4$, the effects of μ_a and μ_s' on the error in D_B is slightly reduced to ~25% (Figure 7f). Finally, although

errors in absolute D_B made at small separations are on the order of 5-10%, errors in relative change in D_B are negligible (<0.5%, Figure 7g, h).

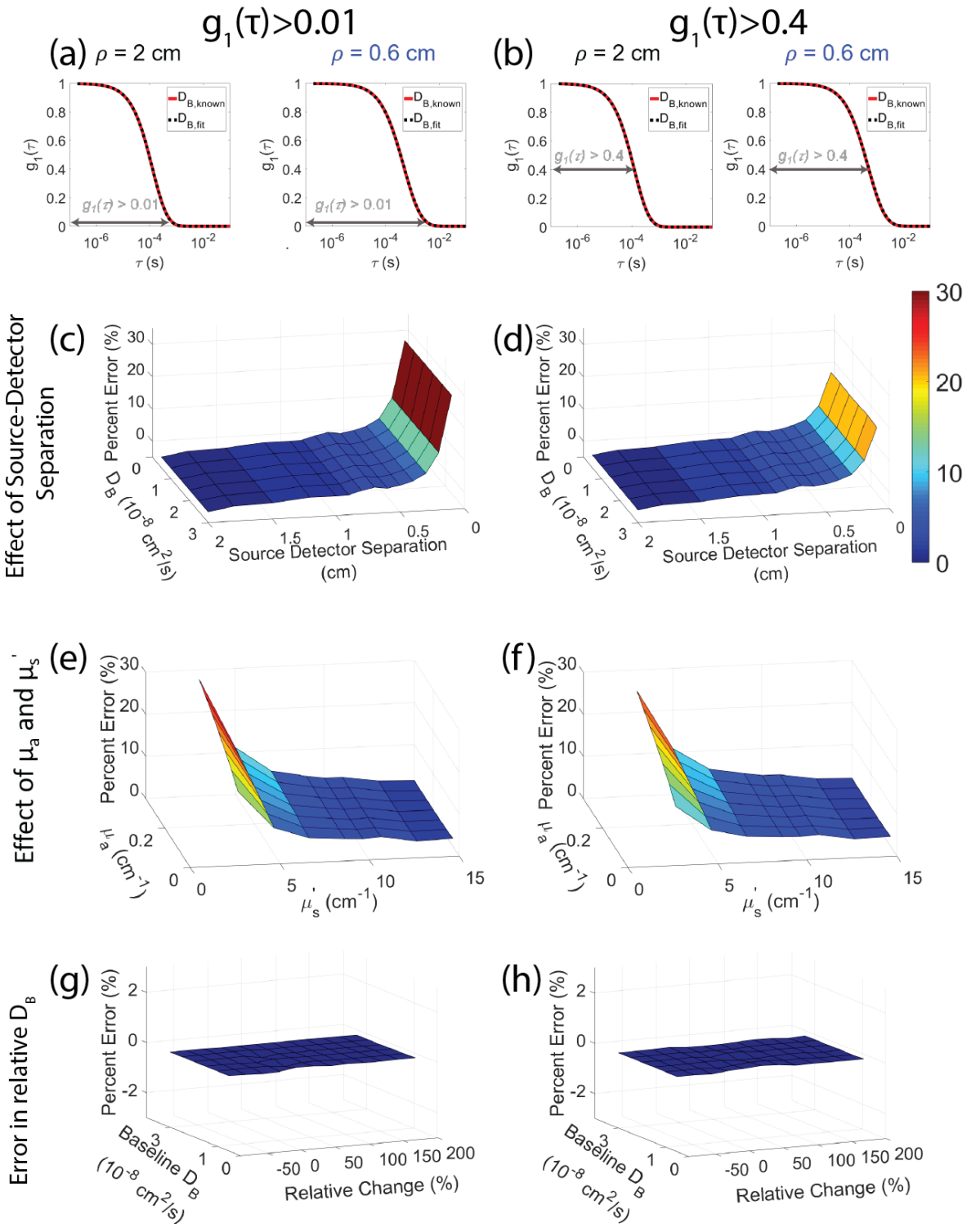

Figure 7: DCS accuracy when simulated $g_1(\rho,\tau)$ data is fit with the constraint of $g_1(\tau)$> 0.01 (left column) or $g_1(\tau)$>0.4 (right column) (a,b) Representative Monte Carlo simulated $g_1(\rho,\tau)$ data (solid line) at 2 and 0.6cm with μ_s'=4.6cm^{-1} and μ_a=0.12cm^{-1}, along with the best fit using the semi-infinite solution to the correlation diffusion equation (dotted line). (c,d) Percent error in D_B as a function of source detector separation and known D_B at a fixed μ_s' =10 cm^{-1} and μ_a= 0.2 cm^{-1}. (e,f) Percent error in D_B as a function of absorption and reduced scattering coefficients at a 0.6cm source-detector separation and a known D_B of 1x10^{-8} cm^2/s. (g,h) Percent error in the relative change in D_B as a function of the baseline D_B and the known relative change in D_B. Data was generated using a 0.6cm source-detector separation with μ_a = 0.2cm^{-1} and μ_s' = 10cm^{-1}.

In Vitro Phantom Verification

Figure 8a displays representative $g_2(\rho,\tau)$ curves measured on the same liquid phantom at both 0.6 and 1.5 cm source detector separations. While the correlation diffusion theory fit for $g_2(\rho,\tau)$ at 1.5 cm matches well with the measurement, the fit for $g_2(\rho,\tau)$ at 0.6 cm slightly diverges from the measurement. This fit at 0.6 cm improved when constrained to only fit $g_2(\rho,\tau)$ >1.2. Despite these small errors in the fit at 0.6 cm, the estimated $D_{B,0.6cm}$ and $D_{B,1.5cm}$ show a good agreement for both phantoms (Figure 8b, c). For fits constrained to $g_2(\rho,\tau)$>1.005, Lin's concordance coefficients, CCC (95% confidence interval), was 0.98 (0.97, 0.99) and 0.83 (0.71, 0.90) for the 2 phantoms, indicating strong agreement between $D_{B,0.6cm}$ and $D_{B,1.5cm}$. Bland-Altman plots of this data reveal that all but 1 data point fall within 1.96 standard deviations of the mean percent difference between the 0.6 and 1.5 cm measurements, providing conformational graphical representation of this strong agreement (Figure 8d, e).

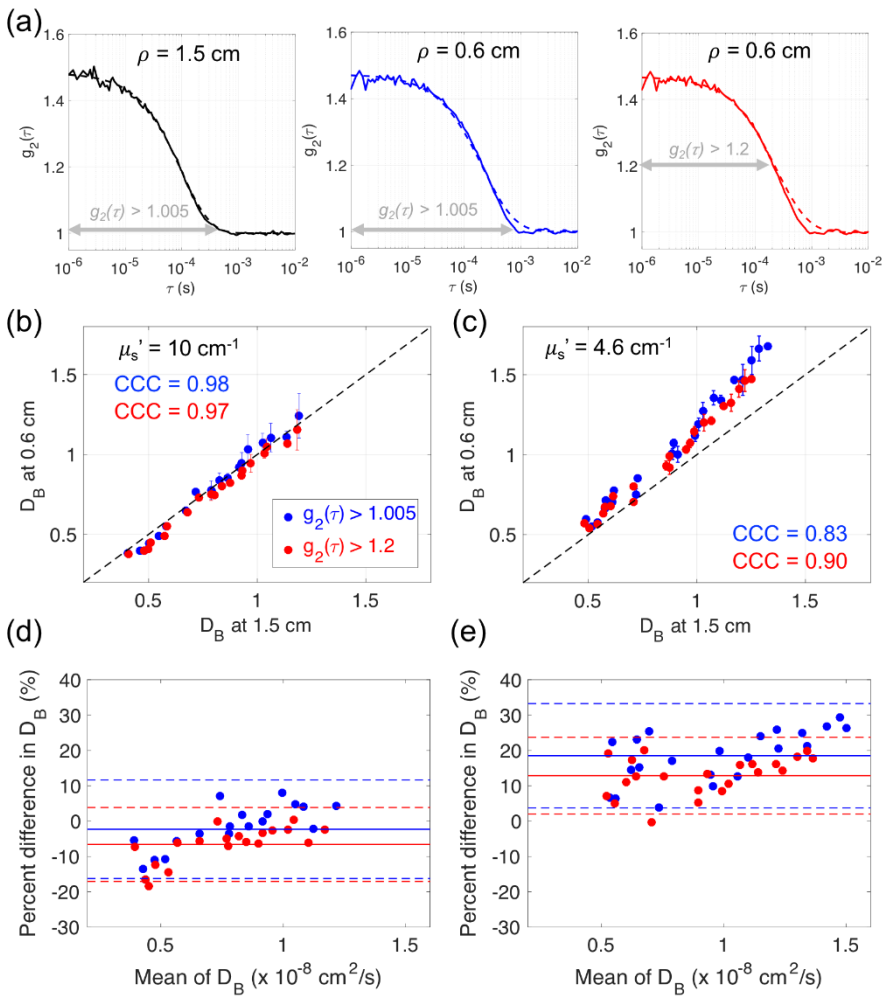

Figure 8: (a) Representative measured (solid) and fitted (dashed) $g_2(\rho,\tau)$ curves at 1.5cm (left) and 6cm (middle: used $g_2(\rho,\tau)> 1.005$, right : used $g_2(\rho,\tau)> 1.2$) on the same liquid phantom (μ_s' = 4.6cm^{-1} and μ_a = 0.12cm^{-1}) at 38°C. (b,c) Comparison between $D_{B,0.6cm}$ and $D_{B,1.5cm}$ for two sets of phantoms (b: μ_s' = 10cm^{-1}, μ_a = 0.12cm^{-1} and c: μ_s' = 4.6cm^{-1}, μ_a = 0.12cm^{-1}) using different g $g_2(\rho,\tau)$thresholds to fit data (blue: $g_2(\rho,\tau)> 1.005$, red: $g_2(\rho,\tau)>1.2$). Error bar represents the standard deviation; CCC denotes Lin's concordance correlation coefficient; dotted line denotes line of identity. (d,e) Bland-Altman plots for b and c, respectively, of the percent difference between $D_{B,0.6cm}$ and $D_{B,1.5cm}$ versus the mean of these parameters. The solid horizontal line represents the mean percent difference and dashed horizontal lines represent the 95% limits of agreement.

Strong correlation between ASL-MRI and DCS

Of the 9 mice imaged, 3 were excluded due to poor T1 image quality. Of the remaining 6 mice, one left hemispheric DCS measurement was discarded based on the exclusion criteria

described in Section 2.2. Thus, a total of 11 hemispheric data points from n=6 mice are included for the final comparison between ASL and DCS. Figure 9a shows a representative anatomical image of the ASL slice taken in the midbrain. The red polygon denotes the region of interest used to quantify an average hemispheric cerebral blood flow. Across all 6 mice, we observed a highly significant correlation between ASL-MRI measures of cerebral blood flow and DCS measures of CBFi measured at 0.6cm (R=0.74, p=0.0088, Figure 9b).

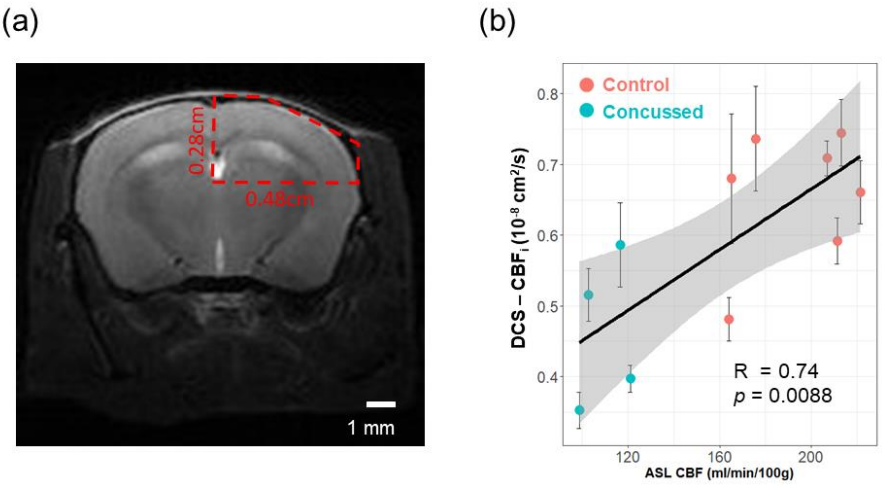

Figure 9: (a) Anatomical image of ASL-MRI mouse with one ROI (red) used to obtain a perfusion value of CBF concurrent with the region that DCS measures. (b) Cerebral blood flow index measured by DCS versus cerebral blood flow measured by ASL-MRI in both healthy (n = 4, 7 hemispheric data points, red) and concussed mice (n=2, 4 hemispheric data points, cyan). Data from left and right hemisphere were treated as independent samples. Black line denotes line of best fit and grey shaded region denotes 95% confidence interval. Error bars represent the standard deviation.

Small separation DCS is highly repeatable

Repeatability measurements taken with a 0.6cm source-detector separation on a liquid phantom revealed an excellent inter-user ICC value of 97%. For mice, the ICC within each user (N=3 users) was 86%, 81%, and 90%; these values are categorized as excellent.

However, the inter-user ICC in mice was only 51%, classified as fair repeatability between users (Figure 10).

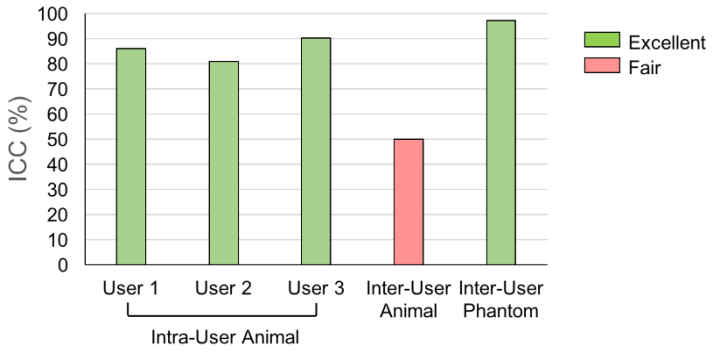

Figure 10: Intraclass correlation coefficient (ICC) for intra- and inter- user repeatability measured on a mouse and for inter-user repeatability measured on a liquid phantom.

3.4 Discussion

In this study, we explore the validity of diffuse correlation spectroscopy in small separation reflectance geometries. A key assumption in correlation diffusion theory is that the source-detector separation must be large in relation to the average random photon walk step size ($\ell^*=1/\mu_s'$). This assumption is necessary such that the photon scattering angles will be sufficiently randomized at the point of detection[47]. In transmission geometries, Kaplan *et al.* demonstrated that DCS works best for slab thicknesses > $10\ell^*$, although in the case of highly anisotropic scattering (as is the case in biological tissue) DCS can work for slab thicknesses as small as $3\ell^*$[124]. However, this same rigorous assessment of the breakdown of DCS has not been performed in reflectance geometries that are most commonly used in biological applications. While a handful of publications have begun to use small (<1cm) DCS reflectance geometries to study blood flow in the mouse brain[121,144], neonatal rat brain[120], mouse and rat hindlimbs[68], mouse tumors[145], mouse bone graft[146,147], skin

flap[148,149], this work is the first to our knowledge that explores the accuracy of these reflectance measurements in a regime where DCS may break down.

Through Monte Carlo simulations, we found that the correlation diffusion approximation does indeed provide a suitable model for small separation reflectance DCS data. For typical absorption and scattering properties of brain tissue, diffusion theory yielded errors in D_B of <12% for source detector separations as small as 0.2cm. As expected, this error decreased with increasing separation because the photon diffusion equation is assumed to be valid at large source-detector separations (>1.5 cm). By constraining fits to those photons associated with shorter tau and thus longer pathlengths by thresholding $g_1(\rho,\tau)>0.4$, this error in the estimation of D_B was reduced to <10% for all tested source-detector separations > 0.2cm. Moreover, we found that these errors effectively cancel out when estimating relative changes in D_B, suggesting that short-separation DCS can be used to accurately track longitudinal changes in cerebral blood flow (assuming the influence of extracerebral layers are negligible).

We next expanded our error quantification beyond the typical optical properties of brain. We found that the error in D_B increased substantially as μ_s' decreased and μ_a increased. This trend was expected, given that the validity of the diffusion approximation is predicated on nearly isotropic radiance (where isotropy is achieved when $\mu_s' >> \mu_a$[47]). However, even when $\mu_s' = 3cm^{-1}$ and $\mu_a=0.35cm^{-1}$, the error in D_B at 0.6cm remained below <25% if the fit for $g_1(\rho,\tau)$ was constrained to > 0.4. This increase in error with decreasing μ_s' was confirmed *in vitro* through our liquid phantom studies that revealed the error in D_B at $\mu_s' = 10\ cm^{-1}$ was roughly half the error seen at $\mu_s' = 4.6\ cm^{-1}$.

Although the error in using the diffusion approximation to fit DCS data at source detector separations needed to probe rodent brain is < 12% for typical brain optical properties, this error certainly may not be negligible for studies in which the effect size of interest is small. As mentioned above, constraining g_2 fits to shorter τ may serve to improve accuracy, as these photons have traveled deeper through tissue[134] and become fully randomized before detection. Indeed, we observed a reduction in the error of D_B when constraining fits to early delay times, although this constraint did not fully ameliorate the error. Future work can explore the depth sensitivity of small separation DCS for a range of delay time constraints, as in Selb et.al.[134] . Alternatively, to further improve accuracy, one could employ a lookup table-based Monte Carlo approach wherein g_2 curves are simulated for a wide range of D_B values, and then the measured g_2 data are fit to this simulated g_2 database[150,151].

We confirmed our *in silico* and *in vitro* results through translation to an *in vivo* mouse brain study. As expected, we observed a significant positive correlation between DCS blood flow index measured at 0.6cm source-detector separation and ASL-MRI measures of absolute cerebral blood flow in mice. We note that the strength of this correlation was likely influenced by several limitations in the experimental design and measurements. First, DCS and ASL-MRI data were not acquired simultaneously because the optical sensor was not MRI compatible, thus introducing the possibility for physiological variation in the time that lapsed between the DCS and ASL measurements (~5 min). Second, DCS measurements represent a bulk average of the banana-shaped region that spans from source to detector, resulting in extracerebral (skull, scalp, cerebrospinal fluid) signal contributions that could be significant. Third, ASL data is subject to low SNR given the small brain size

of mice and the long acquisition time (~20 min for a single blood flow image) and is highly susceptible to motion artifacts caused by respiration. Finally, we had to assume a constant value for μ_a/μ_s' for all animals. As discussed below, this assumption can lead to significant error in D_B if the true optical properties deviate significantly from assumed values. As Diop et.al.[128] demonstrated, measuring individual animal μ_a/μ_s' would improve DCS estimations. Despite these limitations, the significant correlation between ASL and DCS suggests that DCS can provide a sensitive index of cerebral blood flow.

Finally, in the mouse brain, we found excellent repeatability in the DCS measured blood flow index within a given user, although repeatability across different users was only classified as fair. Because inter-user repeatability in the well-controlled phantom experiment was excellent, we attribute inter-user variability in the mouse to both the subtle differences in the positioning of the sensor or possibly to the extent of applied sensor pressure that a particular user typically exerts[139]. Whatever the reason, given the excellent *intra*-user repeatability seen *in vivo*, we recommend that the same operator acquire DCS measurements in the case of longitudinal experiments wherein the same mouse may be measured at multiple time points.

One main limitation in the estimation of an absolute blood flow index with DCS is the need for *a priori* knowledge of μ_a and μ_s' in the sample of interest. In reality, μ_a and μ_s' are often not known and must be assumed from literature-reported values (as we did in our *in vivo* mouse studies). Unfortunately, if these assumed values are inaccurate, they can induce substantial errors in D_B[84]. However, frequency- or time-domain near-infrared spectroscopy techniques that are commonly used in large animal or human studies to quantify μ_a and μ_s' may not be accurate in the rodent head geometry, as the photon diffusion equation that

governs these techniques also breaks down at small separations. Hallacoglu *et al.*[152] demonstrated that μ_a and μ_s' can be measured in the adult rat using multi-distance frequency domain NIRS, although they note that data diverged significantly from diffusion approximation for source-detector separations < 0.8cm. Thus, for mice or neonatal rats, alternative approaches must be employed to estimate tissue optical properties. Our laboratory has developed a Monte Carlo simulation based inverse algorithm to estimate absorption and scattering properties using small separation frequency domain near-infrared spectroscopy that may provide a suitable alternative to estimate μ_a and μ_s' in mice and young rats[150,151].

Although our primary application of small source-detector separation DCS was focused on the rodent brain, we emphasize that the results of this study are generalizable towards other applications. There is a plethora of biological applications that may benefit from a perfusion monitor for tissue at depths of ~1-4mm, wherein other optics-based flow techniques like laser Doppler flowmetry or laser speckle contrast imaging do not provide sufficient depth penetration. These applications include studies of perfusion in the skull and scalp in humans, burn wounds in humans where primary tissue damage occurs in epidermis and dermis[153,154], preclinical models of skeletal muscle[68] , skin flap/ graft monitoring[146,155], and breast cancer models[145].

3.5 Conclusion

We demonstrate that the semi-infinite solution to the correlation diffusion equation provides a suitable approximation to fit DCS data obtained in a reflectance geometry at small (0.2-1cm) source detector separations with excellent *in vivo* intra-user repeatability. Absolute blood flow index estimation is subject to <12% error at these separations, and

error in the estimation of the relative change in blood flow is < 0.5%. These results suggest that DCS may be used to accurately estimate cerebral blood flow in small animal models, as well as other biological applications where a depth penetration >0.1cm is desired.

Chapter 4: Microfluidics and DCS

DCS blood flow measurements are sensitive to red blood cell flow, size, and density. While numerous studies have shown that the DCS-measured BFI is correlated with the flow in tissue, the functional form of the dependence of BFI on flow velocity, vessel size, hematocrit (i.e., red blood cell density), and red blood cell morphology is less understood[78]. Unfortunately, determining the individual effects of these parameters on BFI is challenging in large part due to experimental limitations. For example, *in vivo,* the vasculature dilates in response to decreases in hematocrit to enhance perfusion and maintain adequate oxygen delivery, making it inherently difficult to separate the influence of hematocrit from blood flow on BFI. Alternatively, determining these effects *in vitro* is also challenging given the lack of robust optical phantoms, i.e., systems that mimic the optical and dynamic properties of tissue. Typically, phantoms for DCS consist of a bulk optically-scattering liquid (e.g., Intralipid) wherein "blood flow" is manipulated by adjusting temperature, viscosity, or particle size[156]. While some *in vitro* DCS phantoms have employed small millimeter-diameter tubes embedded in a bulk medium[157], the dimensions and density of these vessels do not adequately recapitulate the microvasculature and thus limit interpretability of the results. Herein, we develop a novel *in vitro* phantom wherein we can *independently* and *systematically* investigate the effects of flow velocity, vessel size, hematocrit, and morphology on the DCS-measured BFI.

4.1 DCS-measured Blood Flow Index is Inversely Proportional to Hematocrit

4.1.1 Introduction

Diffuse correlation spectroscopy (DCS) is a well-validated optical modality used to non-invasively measure blood flow in biological tissue[115,158]. The advantages of DCS over other

clinically-available perfusion modalities, such as MRI, PET, or transcranial Doppler ultrasound, include a high temporal resolution (>20 Hz), relatively low cost (<$50k), continuous bedside monitoring capabilities, and sensitivity to the microvasculature. The technique has shown promise in a wide array of clinical applications, including stroke [48–51], traumatic brain injury [52–55], and cardiac surgery [56–62].

In DCS, the tissue is illuminated with a long-coherence length laser operating in the near-infrared. Light scattering off of moving red blood cells leads to temporal fluctuations in reflected light intensity measured by a remotely located detector on the tissue surface. These intensity fluctuations are characterized using an intensity autocorrelation function that is fit to simple analytical models to extract an index of blood flow, BFI (cm^2/s) [45–47]. In general, BFI reflects both the average flow and density of red blood cells in the interrogated tissue volume[66]. While numerous clinical and preclinical validation studies have experimentally confirmed that BFI correlates with blood flow measured by other gold standard perfusion modalities[158] the dependence of BFI on the density of red blood cells (i.e., hematocrit) has received considerably less attention.

The influence of hematocrit on BFI is an important factor that likely needs to be accounted for both in healthy populations as well as in conditions associated with anemia or polycythemia. Hematocrit levels within the normal population span a broad range and vary with age and between sexes. For example, normal hematocrit levels range from 38–52% for men and 35–44% for women. For women, hematocrit levels can vary significantly over the course of the menstrual cycle [159]. Moreover, for patients with blood disorders, especially chronic anemia, variations in hematocrit are a well-known phenomenon with significant adverse consequences that affect perfusion. For example, patients with sickle

cell disease suffer from "crises" – including crises in which blood is pooled and sequestered in their spleens, crises in which bone marrow function temporarily ceases due to viral infection, and crises that involve microvascular occlusion – during which times hematocrit levels can drop precipitously. This acute worsening of anemia affects blood flow to major organs, including the brain, and a non-invasive monitor of adequate perfusion (e.g., DCS) could help avoid devastating complications like stroke [160]. At the other end of the spectrum, patients with polycythemia vera, a bone marrow disease that leads to elevated hematocrit levels, suffer from increasing hematocrit levels when their disease worsens or when medications begin to fail. Again, given the high risk of stroke in these patients, assessment of microvascular cerebral blood flow with DCS may provide valuable information to guide therapeutic management.

Determining the effects of hematocrit on the DCS-measured BFI is challenging in large part due to experimental limitations. *In vivo,* the vasculature dilates in response to decreases in hematocrit to enhance perfusion and maintain adequate oxygen delivery, making it inherently difficult to separate the influence of hematocrit from blood flow on BFI. Alternatively, determining these effects *in vitro* is also challenging given the lack of optical phantoms that recapitulate tissue microvasculature. Typically, phantoms for DCS consist of a bulk liquid wherein "blood flow" is manipulated by adjusting temperature, viscosity, or particle size [103,156]. While some *in vitro* DCS phantoms have employed small millimeter-diameter tubes embedded in a bulk medium[157], the dimensions of these vessels do not adequately recapitulate the microvasculature and thus limit interpretability of the results.

Herein, we present a novel *in vitro* DCS phantom platform that consists of hundreds of micron-sized channels embedded within a solid polydimethylsiloxane/titanium dioxide/India Ink substrate. While microfluidic systems are not inherently novel, their application to DCS offers a substantial improvement over the traditional bulk liquid phantoms. Our system allows us to utilize physiologically relevant arteriole-sized channel diameters and to flow blood through these channels. In this work, we first validate that DCS can accurately estimate flow in this novel platform, and then we use the platform to demonstrate that the DCS-measured blood flow index is strongly confounded by hematocrit. Finally, we use these results to approximate a hematocrit-correction factor that may be used to minimize the influence of hematocrit[92].

4.1.2 Materials and Methods

Microfluidic phantom platform

For all experiments described herein, we designed a phantom platform that consists of a thin layer of hundreds of long (> 1.5 cm), uniformly spaced, parallel, micron-sized channels embedded 0.3 cm below the surface of a solid polydimethylsiloxane (PDMS), titanium dioxide (TiO_2), and India Ink substrate (Figure 11). Four phantoms were independently tested with minimum microchannel cross-sections of 10×11, 30×28, 60×56, and 100×85 μm ($w \times h$). Channel sizes were chosen to roughly mimic the dimensions of arterioles, capillaries, and postcapillary venules [161]. Vessel spacing within the microfluidic layer was maintained at a constant volume fraction of 3/8 for all phantoms [162,163].

To fabricate these phantoms, standard photolithography processes were used [162]. In brief, SU-8 series photoresists were spun onto silicon wafers to desired heights after cleaning and dehydration. The MLA150 Maskless Aligner (Heidelberg Instruments) was

then used to directly expose patterns onto soft baked resist covered wafers using a 375 nm laser. Following post exposure baking and developing steps, wafers were silanized by treatment with vapor phase hexamethyldisilazane (HMDS) for at least 24 hours. The resulting patterned wafers served as masters for generation of multiple identical microfluidic devices via soft lithography. In this case, a mixture of PDMS/TiO_2/India Ink was prepared by combining 80 g of PDMS at a 10:1 ratio of elastomer to curing agent (NC9285739, Fisher Scientific), 0.152 g of TiO_2 (S25818, Fisher Scientific), and 0.084 g of India Ink (Higgins, Chartpak, MA)[164]. The PDMS/TiO_2/India Ink mixture was poured over the silicon wafer to achieve a thickness of ~0.3 cm. The remainder of this PDMS/TiO_2/India Ink mixture was poured into a plain petri dish to create a thin ~0.2 cm sheet. Both dishes were placed in a vacuum chamber for 1 hour and then cured overnight at 60°C. Next, the surfaces of the patterned device and the unpatterned sheet were exposed to oxygen plasma (NC9332171, Fisher Scientific) for 1 minute and then bonded together. Bonding was further secured by placing the device on a hot plate at 80°C for 10 minutes. The final microfluidic embedded device was trimmed to ~2×3×0.5 cm. Finally, to model the experimental setup as a series of parallel slabs over a semi-infinite medium for data analysis, the microfluidic device was placed on a large PDMS/TiO_2/India Ink block (~13×9×6 cm) with the same optical properties as the embedded microfluidic device.

Experimental protocol

To validate that DCS can accurately measure flow in this phantom platform, we first flowed Intralipid (Fresenius Kabi, Baxter Healthcare, Deerfield, IL) through each of the microfluidic phantoms. Measurements were made on each phantom at multiple flow

rates and at varied concentrations of Intralipid. Intralipid concentration was titrated from 20% to 7% by diluting with distilled water.

To validate the platform with blood and to assess the influence of hematocrit on DCS, we obtained blood samples from healthy human subjects (6 – 24 mL/subject). Blood was collected in EDTA tubes to prevent clotting; all samples were used within 8 hours of collection. Hematocrit was measured via complete blood count (Element HT5, Heska). Each blood sample was aliquoted into 6 subsamples that were diluted with phosphate buffered saline (PBS) to achieve hematocrits ranging from 20 to 45% in increments of 5%. DCS measurements were made on the 30×28 and 100×85 μm microchannel phantoms using each hematocrit aliquot at multiple flow rates. Prior to running each hematocrit aliquot in the phantom, the microfluidic device was flushed with PBS for 2 minutes.

For all experiments, the input of each microfluidic device was connected to a standard syringe pump (70-3008, Harvard Apparatus) through microbore tubing (06418-02 and 06417-11, Cole-Parmer Instrument Company) [162]. The output was connected to a reservoir and allowed to drain freely. The pump flow rate was incrementally adjusted such that the average velocity in the smallest channels varied from 0.155 to 0.93 cm/s in steps of 0.155 cm/s to mimic physiologically relevant velocities [165]. Pump flow rate, Q, can be related to average channel velocity via $Q = A_{cs} \times v_{avg} \times n_{chan}$, where A_{cs}, v_{avg}, and n_{chan} are the cross-sectional area of the microchannels, average velocity, and number of microchannels, respectively[166]. Once the desired flow rate was set, DCS data were acquired after a 1-minute equilibration period.

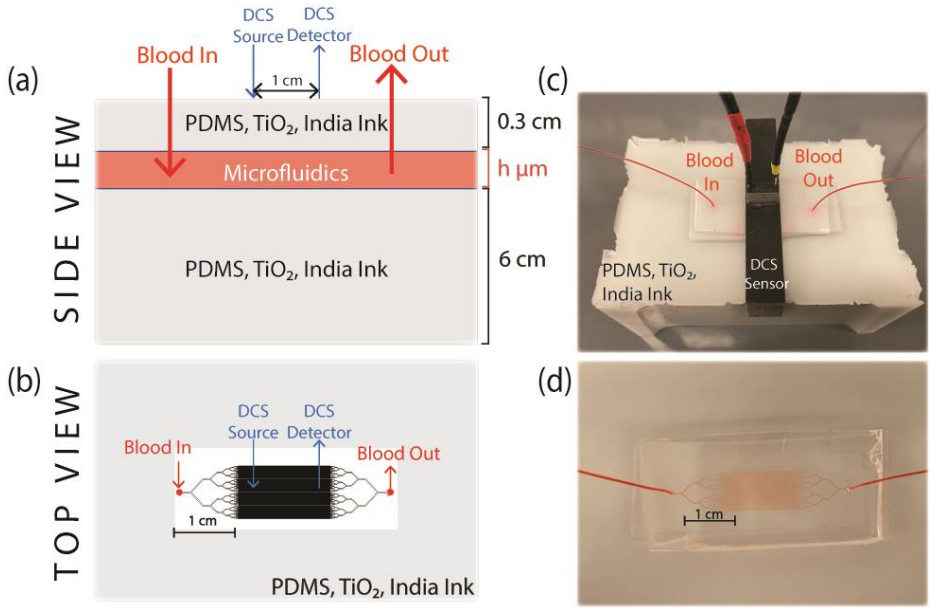

Figure 11: ***In vitro DCS microfluidic phantom.*** *Schematic representation of the (a) side and (b) top view of the microfluidic tissue-simulating phantom. The phantom is comprised of a layer of hundreds of microchannels with height, h, embedded 0.3 cm below the surface of a polydimethylsiloxane (PDMS), titanium dioxide (TiO_2), and India Ink substrate. Intralipid or blood is flowed at a known rate using a standard syringe pump. A 1-cm source-detector separation DCS sensor is placed at the surface the device, and the 3-layer slab solution to the correlation diffusion equation is used to extract an average flow index within the microfluidic layer (c) Image of the experimental setup represented in (a) and (b). (d) Image of the microfluidic capillary network in a transparent PDMS substrate to visualize the channel architecture.*

DCS Acquisition

DCS measurements were made with a custom-built instrument comprised of an 852 nm long coherence length laser (iBeam smart, TOPTICA Photonics, Farmington, NY), a photon counting avalanche photodiode array (SPCM-AQ4C-IO, Perkin-Elmer, Quebec, Canada), and a hardware autocorrelator board (Flex05-8ch, www.correlator.com, NJ). A custom optical sensor was used that consisted of a 1 mm fiber bundle source (FTIIG23767, Fiberoptics Technology, Pomfret, CT) spaced 1 cm away from a single-mode detection fiber (780HP, Thorlabs, Newton, NJ). Fibers were embedded in a black 3D printed holder that was secured to the surface of the microfluidic phantom (Figure 11c). The source and

detector were oriented such that they aligned parallel with the microchannels; however, the sensor orientation and positioning did not significantly influence the results (Appendix 1). Measurements of the intensity autocorrelation function, $g_2(\rho,\tau)$,were made at a 3s integration time and 20-36 frames of data were acquired for each flow rate.

DCS analysis

To analyze DCS data, the experimental setup was modeled as a series of two parallel slabs over a semi-infinite medium. For this geometry, the steady state solution of the correlation diffusion equation for the unnormalized field correlation function at a distance, ρ, from the source on the surface of the top slab is [91]:

$$G_1(\rho,\tau) = \frac{1}{2\pi}\int_0^\infty \tilde{G}_1^0(s,\tau)sJ_0(s\rho)ds, \tag{27}$$

where J_0 is the Bessel function of zeroth order, and

$$\tilde{G}_1^0(s,\tau) = \frac{\text{numerator}}{\text{denominator}}, \tag{28}$$

$$\begin{aligned}\text{numerator} =& (\beta_1 D_1 \cosh(\beta_1(\Delta_1 - z_s))(\beta_2 D_2 \cosh(\beta_2\Delta_2) + \beta_3 D_3 \sinh(\beta_2\Delta_2)) + \\ & \beta_2 D_2 (\beta_3 D_3 \cosh(\beta_2\Delta_2) + \beta_2 D_2 \sinh(\beta_2\Delta_2)) \sinh(\beta_1(\Delta_1 - z_s)))\end{aligned}$$

$$\begin{aligned}\text{denominator} =& \beta_2 D_2 \cosh(\beta_2\Delta_2)(\beta_1(D_1 + \beta_3 D_3 z_0)\cosh(\beta_1\Delta_1) + (\beta_3 D_3 + \beta_1^2 D_1 z_0)\sinh(\beta_1\Delta_1)) \\ & +(\beta_1(\beta_3 D_1 D_3 + \beta_2^2 D_2^2 z_0)\cosh(\beta_1\Delta_1) + (\beta_2^2 D_2^2 + \beta_1^2\beta_3 D_1 D_3 z_0)\sinh(\beta_1\Delta_1)) \times \sinh(\beta_2\Delta_2).\end{aligned}$$

Here, $\beta_i^2 = s^2 + 3\mu_{a,i}\mu_{s,i}^{'} + 6\mu_{s,i}^{'2}k_{0,i}^2 P_i \left\langle \Delta r_i^2(\tau)\right\rangle$, $D_i = 1/(3\mu_{s,i}^{'})$, $z_0 = 1/(\mu_{a,1} + \mu_{s,1}^{'})$, $z_s = 1/\mu_{s,1}^{'}$, Δ_i is the thickness of the i[th] layer, $\mu_{a,i}$ and $\mu_{s,i}'$ are the absorption and reduced scattering coefficients, respectively, for the i[th] layer, $k_{0,i} = 2\pi n/\lambda$ is the wave number for the i[th] layer, λ is the wavelength of light (852 nm), n is the index of refraction (assumed to be 1.4 for all layers [164]), P_i is the probability of scattering off of a moving scatterer in the i[th] layer, and $\langle \Delta r_i^2(\tau)\rangle$ is the mean-square displacement of the moving scatterers in the i[th] layer. For

our experimental setup, layers 1 and 3 consisted of the PDMS/TiO_2/India Ink substrate, and layer 2 contained the microchannels embedded in the PDMS/TiO_2/India Ink substrate, such that Δ_1=0.3 cm and Δ_2 was dependent on the height of the microchannels (either 11, 28, 56, or 85 μm). We measured the optical properties of the substrate in layers 1 and 3 ($\mu_{a,substrate}$ and $\mu'_{s,substrate}$) to be 0.2 cm^{-1} and 5.6 cm^{-1}, respectively, using multi-distance frequency domain near-infrared spectroscopy on the bulk phantom without embedded microchannels [167]. The optical properties of the microfluidic layer ($\mu_{a,2}$ and $\mu'_{s,2}$) took the form of a weighted average by volume of the optical properties of the substrate and the flowing medium (either Intralipid or blood). Optical properties of Intralipid and blood were obtained from literature [168,169].

The probability of scattering off of moving scatterers within the 1st and 3rd layers was assumed to be negligible (i.e., P_1 and P_3~0). For layer 2, this probability took the form of $P_2 = f \times \mu'_{s,flow}/\mu'_{s,avg}$, where f is the volume fraction of flowing medium within the microfluidic layer (0.375 for all phantoms), $\mu'_{s,flow}$ is the reduced scattering coefficient for the flowing medium at 852 nm, and $\mu'_{s,avg} = f \times \mu'_{s,flow} + (1-f) \times \mu'_{s,substrate}$. When flowing Intralipid, we assumed $\mu'_{s,flow} = 186 \times C$ cm^{-1}, where C is the fractional concentration of Intralipid. When flowing blood, $\mu'_{s,flow}$ for each blood sample was estimated using an empirically-derived relationship between the reduced scattering coefficient and hematocrit [169].

The mean-square particle displacement, $\langle \Delta r_i^2(\tau) \rangle$, of layers 1 and 3 was assumed to be negligible. For layer 2, we tested two flow models for $\langle \Delta r_i^2(\tau) \rangle$: convective and diffusive. For the convective model, $\langle \Delta r_i^2(\tau) \rangle$ took the form of $\langle v \rangle^2 \tau^2$, where $\langle v \rangle$ is the spatially weighted average speed of the particles within a microchannel and τ is the delay time. For

the diffusive model, $\langle \Delta r_i^2(\tau) \rangle$ took the form of $\langle D \rangle \tau$, where $\langle D \rangle$ is the spatially-weighted diffusion coefficient of the scatterers within the microchannels. For all experiments, data was separately fit to these two models, and the sum of squares of the fit residuals (SS) was used to determine the form of the mean-square displacement that yielded the best fit of the data. For Intralipid, we expect $\langle \Delta r_i^2(\tau) \rangle$ to be dominated by convective motion, whereas for blood, we expect diffusive motion to dominate. The dominance of diffusion is expected due to an effect known as shear-induced or self diffusion, which occurs in the presence of a shear flow under small Reynolds numbers[79–82]. Effectively, multiple inter-particle hydrodynamic interactions give rise to significant lateral displacements that, when taken together, constitute a random walk. Although shear-induced diffusion is present for both Intralipid and blood, the magnitude of this effect is expected to be much smaller for Intralipid than blood given the small size and spherical nature of Intralipid[80,81] compared to the larger size and deformable, disk shape nature of red blood cells[66,82,170–176].

Experimentally, DCS measures the normalized intensity autocorrelation function, $g_2(\rho, \tau)$, which is typically converted to the normalized field correlation function, $g_1(\rho, \tau)$, using the Siegert relation[70]. However, our phantom is non-ergodic (See Chapter 4 Appendix 3) such that the measured time averaged $g_2(\rho, \tau)$ is not equivalent to the ensemble average of $g_2(\rho, \tau)$ due to the presence of both dynamic and static layers; hence, the Siegert relation breaks down. To relate experimental measurements of $g_2(\rho, \tau)$ to theoretical models for $g_1(\rho, \tau)$ in a non-ergodic sample, we isolate our fit of $g_2(\rho, \tau)$ to the early portion of the curve that is dominated by photons that have sampled the dynamic microchannel layer such that the Siegert relation is valid [73]. For Intralipid, fits were constrained to $g_2(\rho, \tau) \geq 1.33$, and for blood, fits were constrained to $g_2(\rho, \tau) \geq 1.25$. These thresholds were determined

based on visual inspection of the data and were chosen conservatively to isolate the appropriate portion of the $g_2(\rho,\tau)$ curve for all flow rates tested. Each measured frame of $g_2(\rho,\tau)$ data was fit to Equation 28 for either $\langle v \rangle$ or $\langle D \rangle$ within the microfluidic layer (for Intralipid or blood experiments, respectively) and β, a coherence factor used to relate $g_2(\rho,\tau)$ to $g_1(\rho,\tau)$ in the Siegert relation. Results were averaged to obtain a mean and standard error $\langle v \rangle$ or $\langle D \rangle$ across all frames for each pump flow rate. For consistency with *in vivo* DCS studies wherein *P* is not known, when flowing blood through the phantom we also estimated a blood flow index, $BFI \equiv P_2\langle D \rangle$, using the known P_2.

Statistical analysis

For Intralipid experiments, Lin's concordance correlation coefficient (CCC) [140] was used to quantify the agreement between the DCS-measured velocity and the true average velocity in the channels. The CCC is the product of Pearson's R, a measure of precision, and a bias correction factor which reflects the degree that the linear association between two variables differs from 45 degrees through the origin. For whole blood, we plotted the DCS-measured blood flow index (BFI) against the known velocity (v_{avg}) or flow rate (BF_{abs}) to assess the functional relationship. We observed a strong linear relationship (Figure 13); thus, we modeled the relationships between BFI and v_{avg} and BFI and BF_{abs} with linear mixed effects models using sample specific random intercepts that took the forms of $BFI = \beta_0 + \beta_1 \times r + \beta_2 \times v_{avg} + \beta_3 \times r \times v_{avg}$ and $BFI = \beta_0 + \beta_1 \times r + \beta_2 \times BF_{abs} + \beta_3 \times r \times BF_{abs}$, respectively, where *r* is the microchannel dimension (30 or 100 μm).

To assess the influence of hematocrit on $\langle D \rangle$, we first graphically examined the relationship between $\langle D \rangle$ and hematocrit across several flow velocities and two vessel

sizes. Prior to modeling, we assessed the functional form of this relationship using linear models with both linear and higher ordered polynomial terms. The relationship appeared linear across both vessel sizes and all velocities tested; higher-order polynomials did not significantly improve the model fit. Thus, to empirically describe the relationship between hematocrit (Hct) and $\langle D \rangle$, we used a linear mixed effects model that took the form of $\langle D \rangle = \beta_0 + \beta_1 \times Hct + \beta_2 \times v_{avg} + \beta_3 \times Hct \times v_{avg}$. All data from both vessel sizes were included in this model. The coefficients derived from this model were used to to develop a hematocrit-correction factor for $\langle D \rangle$. In order to estimate a confidence interval (CI) for the hematocrit-correction factor, we simulated 1,000 bootstrap samples of size n = 17 with replacement from the overall dataset. For each bootstrap sample, a linear regression was applied using the equation above, and the resulting correction factor was noted. The 95% CI was derived from the 2.5 and 97.5 percentiles of the bootstrap distribution of 1,000 estimated correction factors.

Finally, we applied this hematocrit correction factor to the measured data. We performed a secondary linear mixed effects model for the data obtained from each vessel size to confirm independence of $\langle D \rangle_{Hct-corrected}$ from hematocrit (Hct) (i.e., $\langle D \rangle_{Hct-corrected} = \beta_0 + \beta_1 \times Hct + \beta_2 \times v_{avg} + \beta_3 \times Hct \times v_{avg}$). The goal of this model was to demonstrate that β_0, β_1, and β_3 were not statistically different from 0. All regression analyses were performed in Matlab (Mathworks, Natick, MA) using the *fitlme* function. Goodness of fit was determined by visual inspection of fit residuals and quantification of model R^2. Statistical significance was declared for p-values < 0.05.

4.1.3 Results

Verification of DCS measurements in the microfluidic phantom using Intralipid

To demonstrate the accuracy of DCS in this platform, we first used Intralipid at multiple flow rates. Representative $g_2(\tau)$ curves from Intralipid along with the best fit lines using the diffusive and convective models for the mean-square displacement in the microfluidic layer are shown in Figure 12a. The convective model provided the best fit to the data, as indicated by the reduction in the sum of squares fit residual (SS). Using this model, the DCS-measured average flow velocities agreed well with the known average velocities across all concentrations of Intralipid tested (all R^2>0.99, p<0.01, CCC > 0.95, Figure 12b).This strong agreement between the measured and known velocities was also seen for all vessel sizes tested (all R^2>0.98, p<0.001, CCC > 0.95, Figure 12c).

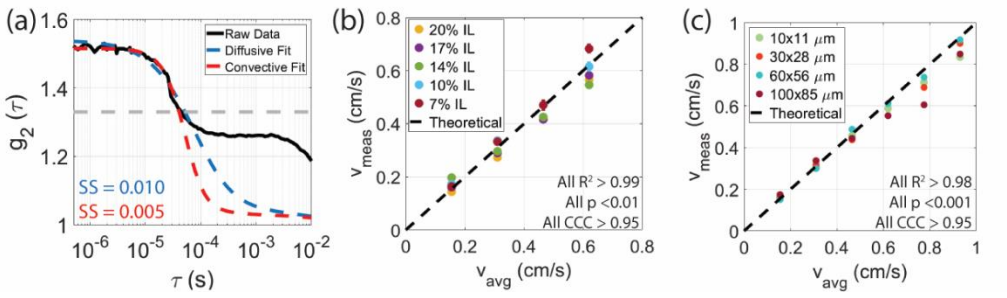

*Figure 12: **Verification with Intralipid.** (a) Representative $g_2(\tau)$ data measured when flowing Intralipid through the 30×28 μm microfluidic phantom. The gray dashed line represents the cutoff used to fit the data to minimize the effects of non-ergodicity. The convective model (red) resulted in the lower sum of squares (SS) fit residual than the diffusive model (blue). (b-c) The DCS-measured velocity (v_{meas}) versus the known average velocity (v_{avg}) in the (b) 30×28 μm microchannels for five concentrations of Intralipid (7-20%, all R^2>0.99, CCC>0.95, and p<0.01) and (c) in four different microchannel phantoms using 20% Intralipid (10-100 μm, all R^2>0.98, CCC>0.95, and p<0.001). In these subplots, the black dashed line denotes the line of unity, and the colored dots are the mean/standard error values across 36 frames of data.*

Verification of DCS measurements in the microfluidic phantom using whole blood

Representative $g_2(\tau)$ curves from whole blood (hematocrit = 45%) along with best fit lines using the diffusive and convective models for the mean-square displacement in the microfluidic layer are shown in Figure 13a. When flowing whole blood, the diffusive

model provided the best fit to the data, as shown by the lower SS. Using this model, the DCS-measured BFI was strongly linearly correlated with the known average velocity in the channels, such that a 4× increase in velocity from 0.155 to 0.62 cm/s resulted in a similar 4× increase in BFI. This linear trend persisted across both vessel sizes studied (Figure 13b, model R^2=0.98, p<0.001, no significant interaction term between velocity and vessel size, p=0.64). BFI was also strongly correlated with the average flow rate in the channels, although the slope of this trend was dependent on vessel size, with smaller vessels having a steeper slope (Figure 13**c**, model R^2=0.98, p<0.001, significant interaction term between average flow rate and vessel size, p<0.001).

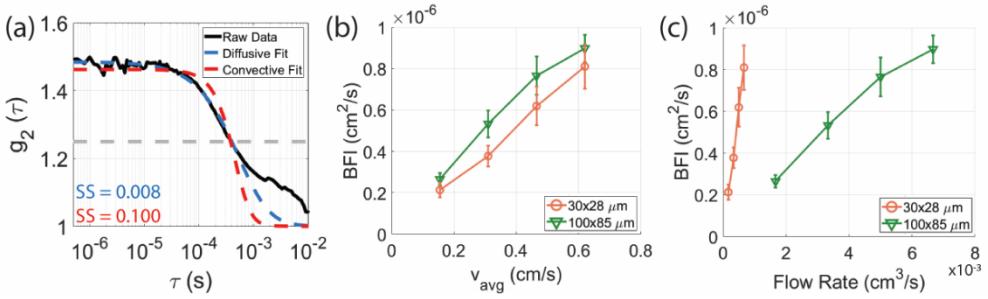

Figure 13: ***Verification with whole blood.*** *(a) Representative $g_2(\tau)$ curve measured when flowing whole blood (hematocrit = 45%) through the microfluidic phantom. The gray dashed line represents the cutoff used when fitting the data to minimize the effects of non-ergodicity. The diffusive model (blue) resulted in the lower sum of squares (SS) fit residual than the convective model (red). (b-c) Mean/standard error DCS-measured blood flow index (BFI) versus b) the known average velocity (v_{avg}) and c) the known flow rate in the microchannels for 30×28 µm (n=4) and 100×85 µm (n=3) vessel sizes (salmon pink and green, respectively).*

DCS blood flow index is inversely proportional to hematocrit

Next, we varied the hematocrit of the flowing blood within the microfluidic layer. At a fixed flow velocity, as hematocrit increased, the DCS-measured BFI decreased (Figure 14 a, b). This confounding effect was observed for all vessel sizes and flow velocities tested. Further, we found that the hematocrit-dependence of BFI was not solely attributable to the

fraction of scattering events that occur from moving scatterers (P_2), which is known for our model systems. The BFI-derived effective diffusion coefficient, $\langle D \rangle = BFI/P_2$, was inversely linearly proportional to hematocrit and varied by as much as ~70% as hematocrit dropped from 45% to 20% (Figure 14 c, d). Modeling $\langle D \rangle$ as a function of hematocrit and v_{avg}, we found that the overall effect of hematocrit was not significant ($p = 0.934$). However, both the interaction between hematocrit and v_{avg} and the overall effect of v_{avg} were significant ($p < 0.001$), indicating a significant relationship for hematocrit that depended on v_{avg} ($p < 0.001$), i.e., $\langle D \rangle = \beta_2 \times v_{avg} + \beta_3 \times v_{avg} \times Hct$, where β_2 and β_3 are the model coefficients for the overall effect of v_{avg} and the interaction between v_{avg} and hematocrit, respectively.

Using this empirical model, we derived a hematocrit correction factor, $^{1/(1-\gamma \times Hct)}$, where $\gamma = \beta_3/\beta_2$ and $\langle D \rangle_{Hct-corrected} = \langle D \rangle/(1 - \gamma \times Hct)$. We found $\gamma = 1.8$ with a 95% CI of (1.786, 1.792). Figure 15 shows the results of applying this correction factor to the data from Figure 14c, d. Once corrected, neither the overall effect of hematocrit nor the interaction between hematocrit and v_{avg} were statistically significant (all $p>0.05$ for both vessel sizes tested).

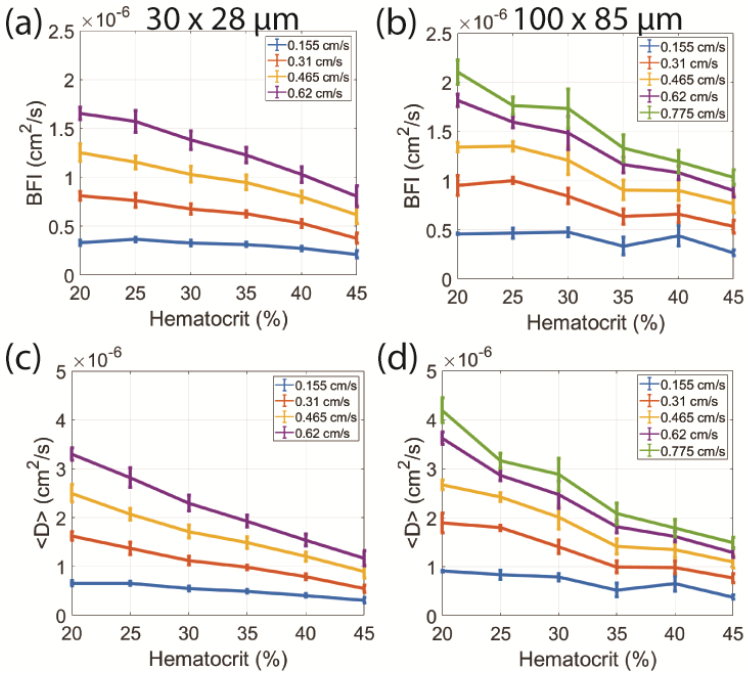

Figure 14: ***Effects of hematocrit.*** *DCS-measured blood flow index (BFI) versus hematocrit at five fixed flow velocities for (a) 30×28 μm and (b) 100×85 μm microchannels. (c-d) The DCS-measured spatially-weighted average diffusion coefficient ($\langle D \rangle = BFI/P_2$), where P_2 is the known probability of scattering off of a moving red blood cell within the microfluidic layer) versus hematocrit across five fixed velocities for (c) 30×28 μm (n=4) and (d) 100×85 μm (n=3) microchannels. All data are reported as mean/standard error across 3-4 blood samples; solid lines connect data points obtained at a fixed flow velocity.*

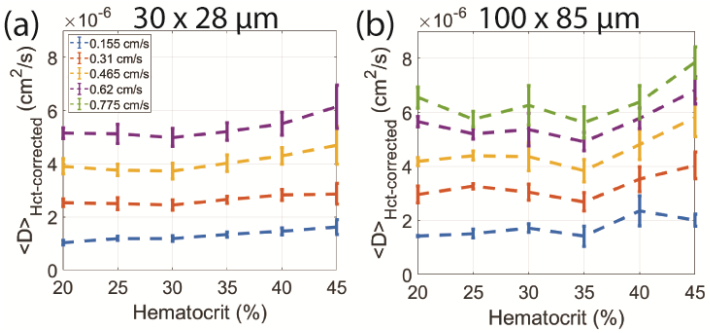

Figure 15: ***Correcting for the effects of hematocrit.*** *The hematocrit-corrected diffusion coefficient ($\langle D \rangle_{Hct-corrected}$) versus hematocrit for (a) 30×28 μm (n=4) and (b) 100×85 μm (n=3) microchannels. All data are reported as mean/standard error across 3-4 blood samples; dashed lines connect data points obtained at a fixed flow velocity.*

4.1.4 Discussion

In this study, we characterize the confounding influence of hematocrit on the DCS-measured blood flow index using a novel *in vitro* microfluidic phantom platform. This *in vitro* model presents an alternative to bulk liquid phantoms commonly used by the DCS community in that it better mimics the tissue microvasculature. The slab geometry of the phantom enables us to utilize an analytical solution to the correlation diffusion equation to measure flow dynamics within the microchannels. Furthermore, the phantom is biologically inert, thereby enabling us to probe a particular biological interaction of interest, e.g., hematocrit and BFI, without unintended confounding variables (e.g., vessel dilation in response to lowered hematocrit). These interactions are often challenging to isolate *in vivo* wherein hemodynamics are regulated by complex physiological processes.

We first validated this phantom platform using Intralipid, a highly scattering fatty emulsion that consists of spherical soybean oil droplets within a lipid membrane (~0.5 μm in diameter [177]) suspended in glycerin and water. As expected for the case of small spherical particles in a shear flow under low Reynolds number, we show that convective motion dominates the decay of the intensity autocorrelation due to the relatively small influence of shear-induced diffusion. Given this dominance of convective motion, we demonstrate that DCS can accurately measure the average velocity within the micron-sized channels of the phantom. We observed strong agreement between the DCS-measured velocity and known average velocity across all channel sizes and Intralipid concentrations tested (Figure 12).

In the case of whole blood, we observed that the diffusive model provided the best fit to the intensity autocorrelation data (Figure 13a). This observation is in good agreement with the plethora of *in vivo* DCS studies that show the diffusive model best fits

experimental data obtained on a wide-range of tissue types. Further, it agrees well with recent *in silico* work by Boas *et al.* simulating a dense volume of tissue with embedded dynamic blood vessels that suggests the correlation decay is dominated by shear-induced diffusion[66]. Moreover, our measured diffusion coefficient is the same order of magnitude as Tang *et al*. measured *in vivo* with dynamic light scattering optical coherence tomography (~0.5e-6 cm^2/s)[178]. Through dimensional analysis, it can be inferred that the shear-induced diffusion coefficient should be proportional to the shear rate[79–81]. Thus, as Boas *et al*. derive, the blood flow index measured by DCS should be proportional to the average flow rate in the vessels[66]. Indeed, we observed strong positive correlation between BFI and flow velocity and flow rate, where the slope of this linear relationship was dependent on vessel cross-section (Figure 13b, c). The consistency of these results with the work of Boas et al. further validate our platform and support the notion that DCS is sensitive to shear-induced diffusion of red blood cells.

Importantly, for both vessel sizes studied, we found that BFI decreases as hematocrit increases, despite a constant flow rate (Figure 14a, b). This result confirms that hematocrit is a significant factor that can confound estimations of blood flow made through DCS. We show that the dependence of BFI on hematocrit is driven by both P_2, the fraction of scattering events that occurs off moving red blood cells (which is known for our phantom), as well by $\langle D \rangle$ (Figure 14c, d). Assuming the DCS-measured $\langle D \rangle$ reflects the spatially-weighted average of the shear-induced diffusion coefficient, there are several possible explanations for the inverse linear relationship between hematocrit and $\langle D \rangle$. While an increase in hematocrit increases the chances of interparticle interactions, it also limits the degree of lateral movement that can be experienced before interaction with another blood

cell and thereby may reduce the magnitude of the diffusion coefficient. Alternatively, or possibly additionally, the Fåhraeues-Lindqvist effect may play a significant role [179,180]. This effect dictates that for vessel sizes less than ~300 μm, increasing hematocrit leads to an increase in apparent viscosity, which in turn may significantly reduce lateral displacements of red blood cells. Although the hematocrit-dependence of the shear-induced diffusion coefficient has been investigated previously by a handful of studies[82,171,172,181], none have been performed with relevant microvascular geometries, concentrations, and/or on time scales relevant to DCS measurements, preventing direct comparison to our results. One limitation with our tissue-simulating microfluidic phantom involves flow in one direction. *In vivo,* vessels are not parallel to each other; therefore, the flow profile is in multiple directions. However, we are not able to vary flow direction across different channels in our microfluidic phantom.

The observed inverse relationship between BFI and hematocrit agrees well with recent *in vivo* data from our laboratory wherein we found that DCS appeared to significantly overestimate cerebral blood flow in moderately/severely anemic patients with sickle cell disease compared to healthy controls[182]. While studies with MRI and PET have demonstrated ~1.5× increases in cortical cerebral blood flow in sickle versus controls[183–185], we observed a markedly more pronounced 3× difference in DCS-measured BFI between sickle and control groups on average. After applying the empirically derived correction factor described herein, the median difference in BFI between sickle and control groups was reduced to 1.7×, which is much closer to literature reports. While this result is promising, more work is needed to validate this hematocrit correction factor *in vivo*, as the

results obtained from the simplified vessel geometry of our *in vitro* phantom may not directly translate to the complex vascular networks found in tissue.

Finally, we note several limitations of this novel microfluidic DCS phantom. The device consists of hundreds of uniformly sized channels and flow is only permitted in one direction, whereas *in vivo* capillary networks contain an array of vessel sizes that are not planar in geometry. Moreover, the channels are rigid in size, whereas *in vivo* blood vessels exhibit a range of compliance. Vessel compliance may permit additional diffusive motion than observed in our rigid channel structure. Despite these limitations, this microfluidic platform certainly provides a better recapitulation of the microvascular environment than existing DCS phantom platforms. Finally, the correlation diffusion equation that we used to fit our experimental data relies on the assumption that the motion of the scatterers is uncorrelated, i.e., that the photon scattering direction is randomized between dynamic scattering events. This assumption is not valid when flowing blood through our microfluidic platform, as outlined in[66], although Monte Carlo simulations suggest that the correlation diffusion equation is still a good model for the system. Future work that independently measures the shear-induced diffusion coefficient within the microchannels is warranted to confirm the accuracy of the model.

4.1.5 Conclusion

In summary, we develop and validate a novel phantom platform for diffuse correlation spectroscopy measurements. We use this platform to determine that hematocrit significantly influences the DCS-measured blood flow index, and we derive a hematocrit correction factor to minimize this influence. These results suggest that without correcting for the effects of hematocrit, DCS BFI will overestimate blood flow in anemic patients.

Future work will validate the hematocrit correction factor *in vivo* and will use this platform to investigate other parameters that may confound the blood flow index, including vessel size, vessel density, and red blood cell morphology.

4.1.6 Appendix 1

To examine the effect of sensor orientation on the measured data, we flowed 20% Intralipid through the 30×28 µm microchannel device at four velocities and varied the DCS sensor positioning to be either parallel or perpendicular to the microfluidic channels. Sensor orientation did not significantly influence the measured channel velocity (Figure 16a). Thus, for all experiments described herein, the DCS sensor was oriented parallel to the microfluidic channels for consistency.

To examine the repeatability of these measurements we obtained two blood samples from a healthy volunteer taken nine months apart. Measurements of DCS blood flow index were acquired within eight hours of sample collection at multiple flow velocities and two different hematocrits. Data were found to be highly repeatable with an intra-class correlation coefficient (ICC) = 0.95 (Figure 16b)[142,143].

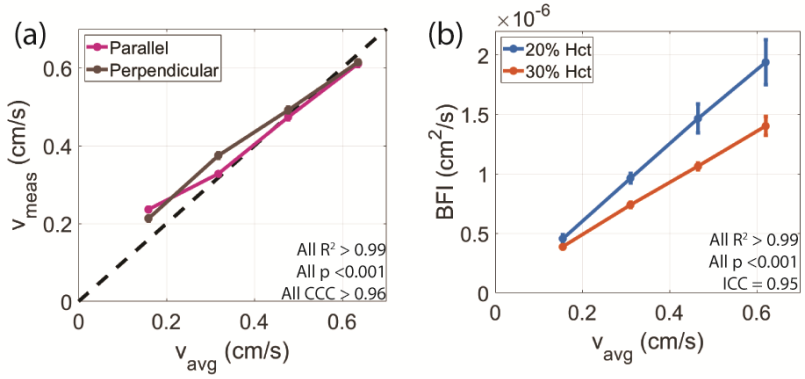

Figure 16: ***Effect of sensor orientation and measurement repeatability.*** *(a) The DCS-measured velocity (v_{meas}) versus the known average velocity (v_{avg}) of 20% Intralipid in the 30×28 µm microchannel phantom device when the sensor was positioned parallel (magenta) or perpendicular (brown) to the channel orientation. Data are plotted as mean*

and standard error across 36 frames of data. (b) The DCS-measured blood flow index (BFI) versus the known average velocity of blood obtained from a healthy volunteer and diluted with PBS to 20% (blue) and 30% hematocrit (orange). Data are reported as mean and standard error across two repetitions of this experiment from the same donor, spaced nine months apart.

4.2 Influence of Vessel Size on the DCS-measured Blood Flow Index

Diffuse correlation spectroscopy (DCS) is an optical modality used to non-invasively measure an index of blood flow (BFI) in biological tissue[47,115]. Specifically, in DCS, coherent near-infrared light multiply scatters as it diffuses through tissue before detection at some distance away on the tissue surface. Scattering off moving red blood cells within the tissue leads to temporal fluctuations in the detected light intensity. These temporal fluctuations are quantified through a temporal intensity autocorrelation function, $g_2(\tau)$, that is fit to simple analytical models, known as correlation diffusion theory[65], to extract an index of blood flow. Although the units of this index (cm^2/s) are not the traditional units of blood flow, DCS has been extensively validated *in vivo* against various "gold-standard" perfusion modalities[158].

Recently, it has been posited that DCS is sensitive to the shear-induced diffusion of red blood cells, which refers to the random walk-like motion of red blood cells in shear flow and is linearly proportional to blood flow[78]. However, the functional form of the dependence of BFI on flow velocity, hematocrit, and vessel size is less understood. Boas et al. demonstrated *in silico* that the DCS BFI is proportional to flow rate, but this relationship is modulated by hematocrit and vessel size[66]. Previously, we developed an *in vitro* platform to demonstrate for the first time a significant inverse relationship between hematocrit and the DCS BFI at two different vessel sizes; we subsequently developed a hematocrit correction equation that eliminated this inverse relationship [92].

In this Letter, we utilize a novel, previously validated[92] microfluidic phantom platform to empirically determine the influence of vessel size on the blood flow index measured with DCS. This phantom system provides the unique ability to systematically explore the influence of various physiologic factors (e.g., flow velocity, vessel size, hematocrit) without the confounding variables often seen *in vivo*. Details of the experimental setup, data acquisition, and data analysis are described in[92].

In brief, we tested 5 independent phantoms with minimum microchannel cross-sections of 10 ×11, 30×28, 60×56, 80×78, and 100×85 μm ($w \times h$). These channel sizes were chosen to mimic the size of arterioles, venules, and capillaries[161]. Vessel spacing within the microfluidic layer was maintained at a constant volume fraction of 3/8 for all phantoms[162,186]. For each phantom, blood was flowed at 5 velocities, ranging from 0.155 to 0.775 cm/s in even steps, chosen to mimic physiologically relevant velocities[165], using a standard syringe pump and whole blood obtained from four healthy male volunteers. Blood was collected in EDTA tubes to prevent clotting; all samples were used within 8 hours of collection. Hematocrit was measured through a complete blood count analyzer (Element HT5, Heska). Blood samples were diluted using phosphate-buffered saline (PBS) to achieve a desired hematocrit of 45%. The relationship between average velocity (v_{avg}) and flow rate (Q) is $Q = A_{cs} \times v_{avg} \times n_{chan}$, where A_{cs} is the cross-sectional area of the microchannels and n_{chan} is the number of microchannels. For each flow velocity, DCS was used to measure an index of blood flow in the channel.

BFI is defined as $BFI \equiv P_{RBC} \times \langle D \rangle$, where P_{RBC} is the probability of scattering off a red blood cell and $\langle D \rangle$ is the spatially-weighted diffusion coefficient [78]. P_{RBC} is known for our model system [92], thus, we report $\langle D \rangle$ herein.

For statistical analysis, to assess the influence of vessel size on $\langle D \rangle$, we first graphically examined the relationship between $\langle D \rangle$ and vessel size across 5 flow velocities at a single hematocrit. Since we observed a strong linear relationship, we empirically modeled the relationships between $\langle D \rangle$ and velocity (v_{avg}) and $\langle D \rangle$ and flow rate (BF_{abs}) with a linear mixed effects models using sample specific random intercepts that took the forms of: $\langle D \rangle = \beta_0 + \beta_1 \times v_{avg} + \beta_2 \times VS + \beta_3 \times v_{avg} \times VS$ and $\langle D \rangle = \beta_0 + \beta_1 \times BF_{abs} + \beta_2 \times VS + \beta_3 \times BF_{abs} \times VS$, respectively, where VS is vessel size. Using a linear mixed effects model allowed us to quantify the coefficients derived from this model and their statistical significance, indicating to us which variables or combination of variables are independent of the relationship between $\langle D \rangle$ and velocity/flow rate. These regression analyses were performed in Matlab (Mathworks, Natick, MA) using the *fitlme* function. Goodness of fit was determined by visual inspection of fit residuals and quantification of model R^2. Statistical significance was declared for p-values < 0.05.

We found that $\langle D \rangle$ increases linearly with average velocity across all vessel sizes (model R^2=0.94, Figure 17). When all five vessel sizes were included, we observed that the only statistically significant interaction terms were between the combination of vessel size and average velocity and average velocity ($p<0.05$, Table 2). However, this interaction term between vessel size and average velocity was not significant when only vessel sizes >10 μm were included in the model ($p=0.6$).

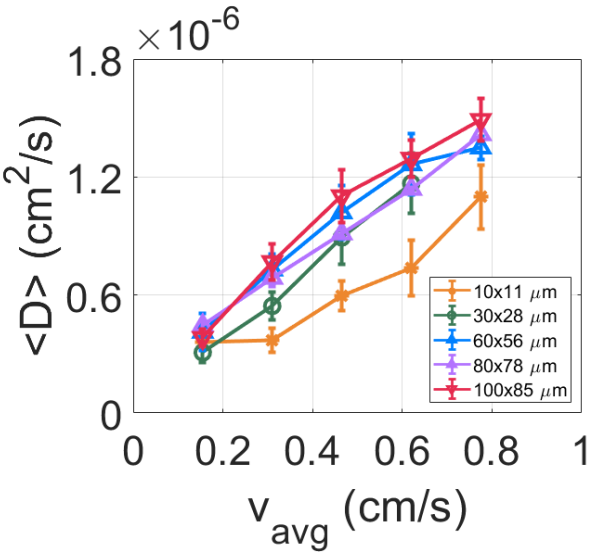

Figure 17:Mean and standard error of the spatially-weighted diffusion coefficient ($\langle D \rangle$) vs the known average velocity (v_{avg}). All blood samples had a hematocrit of 45%.

Table 2: Multivariable analysis of the coefficients from the linear mixed effects model for diffusion coefficient, $\langle D \rangle$, vessel size (VS), and average velocity (v_{avg})

	Vessel sizes > 10 µm		All Vessel Sizes	
	Est (95% CI)[1]	*P*	Est (95% CI)[2]	*P*
V_{avg}	1.77e-6 (1.42e-6, 2.12e-6)	**<0.001**	1.33e-6 (1.09e-6, 1.57e-6)	**<0.001**
VS	2.43e-9 (-1.18e-9, 6.04e-9)	0.18	1.65e-9 (-1.24e-9, 4.53e-9)	0.26
V_{avg} x VS	-1.21e-9 (-5.91e-9, 3.48e-9)	0.61	4.21e-9 (4.88e-10, 7.93e-9)	**0.03**

Next, we similarly observed a linear relationship between $\langle D \rangle$ and flow rate across 5 different vessel sizes (model R^2=0.88, Figure 18); however, the interaction between vessel size and flow rate was highly significant, regardless of vessel size (p<0.001, Table 3).

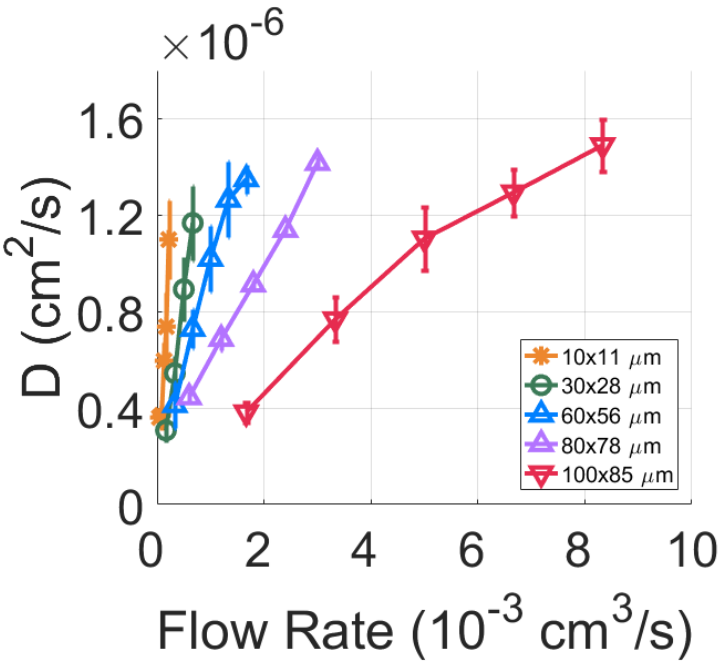

Figure 18: Mean and standard error of the spatially-weighted diffusion coefficient (⟨D⟩) vs the known flow rate. All blood samples had a hematocrit of 45%.

Table 3: Multivariable analysis of the coefficients from the linear mixed effects model for diffusion coefficient, ⟨D⟩, vessel size (VS), and flow rate

	Vessel sizes > 10 μm		All Vessel Sizes	
	Est (95% CI)[1]	*P*	Est (95% CI)[2]	*P*
Flow Rate	1.7e-3 (1.5e-3, 1.9e-3)	**<0.001**	1.7e-3 (1.5e-3, 1.97e-3)	**<0.001**
VS	-6.41e-10 (-4.19e-9, 2.9e-9)	0.72	-2.69e-9 (-5.5e-9, 1.56e-10)	0.06
Flow Rate x VS	-1.54e-5 (-1.74e-5, -1.33e-5)	**<0.001**	-1.56e-5 (-1.8e-5, -1.31e-5)	**<0.001**

In summary, we explored the effects of vessel size on our DCS blood flow index. We observed that $\langle \boldsymbol{D} \rangle$ linearly increases with the average velocity and flow rate but is influenced by vessel size. Fundamentally, blood flow is equal to the blood pressure gradient divided by the vascular resistance to blood flow. Further, resistance to blood flow is determined by Poiseuille's Law, where $\boldsymbol{R = 8\eta L/(\pi r^4)}$, where $\boldsymbol{\eta}$ is the blood viscosity, L is the length of the vessel, and r is the radius of the vessel. Thus, blood flow is proportional to vessel size. However, in blood vessels less than 500 μm, blood behaves as a non-Newtonian fluid, where the blood viscosity is dependent on the vessel diameter and hematocrit in an effect known as the Fahraeus-Lindqvist effect[179]. At 45% hematocrit, the

blood viscosity decreases with decreasing vessel diameter till 30 μm before it significantly increases at smaller diameters[187]. Since the apparent viscosity is much lower in these smaller vessels, it could attribute to a reason why our measured $\langle \boldsymbol{D} \rangle$ was significantly lower in the $\mathbf{10 \times 11}\ \boldsymbol{\mu m}$ channels, in comparison to the other four channels. Since DCS is sensitive to the shear-induced diffusion of red blood cells, an increase in blood viscosity means that particle-particle interactions from shear-induced diffusion may experience less lateral displacement, resulting in a lower $\langle \boldsymbol{D} \rangle$ [78,178].

Regardless, across the five vessel sizes, we observed that $\langle D \rangle$ remains linearly proportional to average velocity and flow rate. However, with flow rate, this proportionality is dependent on vessel size.

4.3 Influence of sickle cell blood on DCS blood flow measurements

4.3.1 Introduction

The motivation behind setting up these microfluidic experiments was to gain a better understanding of the DCS blood flow values that we were measuring in the sickle cell disease patients. Because sickle cell patients are anemic, we expect that the resting state cerebral blood flow of a sickle cell disease patient will be higher than that of a healthy control. This result has been observed in the perfusion MRI community, who observed 1.5 times increase in resting state cerebral blood flow between sickle cell pediatric patients and healthy controls[183]. However, when we published a paper that utilized DCS and made resting state cerebral blood flow measurements in sickle cell pediatric patients and healthy children, we observed 3 times increase in resting state cerebral blood flow measured by DCS between sickle cell pediatric patients and healthy children[182]. Therefore, we designed this microfluidic phantom platform to study the origins of the DCS blood flow signal.

Earlier in this chapter, I have discussed the work we have done with healthy blood by varying hematocrit and vessel size. Here, I will flow sickle cell blood through the microfluidic channels for the first time under fully oxygenated conditions. I hypothesize that the DCS blood flow index of sickle cell blood will be less than that of healthy blood since sickle cell blood is more viscous than healthy blood.

4.3.2 Methods

Microfluidic Phantom Platform

For all experiments described in this section, we utilize a novel, previously validated[92] microfluidic phantom platform to measure the DCS blood flow index when flowing sickle cell anemic blood, under fully oxygenated conditions. Two phantoms were independently tested with minimum microchannel cross-sections of 30×28 and 80×75 μm ($w \times h$). Vessel spacing within the microfluidic layer was maintained at a constant volume fraction of 3/8 for all phantoms[162,163].

Experimental Protocol

To assess the influence of sickle cell blood on the DCS blood flow index, we obtained blood samples from two sickle cell anemic (HbSS) pediatric patients, (6-9 mL/subject) who were on hydroxyurea and did not receive a transfusion in the <3 months through the Children's Healthcare of Atlanta Biorepository. Blood was collected in EDTA tubes to prevent clotting; all samples were used within 6 hours of collection. Hematocrit was measured via complete blood count. Gel electrophoresis was performed to quantify hemoglobin concentrations. Each blood sample was aliquoted into 1-2 subsamples that were diluted with phosphate buffered saline (PBS) to achieve hematocrits ranging from 20 to 30% in increments of 5%. DCS measurements were made on the 30×28 and 80×75 μm

microchannel phantoms using each hematocrit aliquot at multiple flow rates. Prior to running each hematocrit aliquot in the phantom, the microfluidic device was flushed with PBS for two minutes.

For all experiments, the input of each microfluidic device was connected to a standard syringe pump through microbore tubing[92]. The output was connected to a reservoir and allowed to drain freely. The pump flow rate was incrementally adjusted such that the average velocity in the smallest channels varied from 0.155 to 0.775 cm/s in steps of 0.155 cm/s to mimic physiologically relevant velocities[165]. Pump flow rate, Q, can be related to average channel velocity via $Q = A_{cs} \times v_{avg} \times n_{chan}$, where A_{cs}, v_{avg}, and n_{chan} are the cross-sectional area of the microchannels, average velocity, and number of microchannels, respectively[166]. Once the desired flow rate was set, DCS data were acquired after a 1-minute equilibration period.

DCS Data Acquisition and Analysis

The same DCS acquisition and analysis schemes were followed as describe in [92]. For the DCS analysis, it is necessary to know the optical properties of each of the three layers. We measured the optical properties of the PDMS/TiO_2/India Ink substrate in layers 1 and 3 to be 0.2 cm^{-1} and 5.6 cm^{-1}, respectively, using multi-distance frequency domain near-infrared spectroscopy[188] on the bulk phantom without any embedded microchannels. The optical properties of the microfluidic layer took the form of a weighted average by volume of the optical properties of the substrate and the flowing medium (blood). We assumed the optical properties of sickle cell blood to be similar as healthy blood[169,189]. Alternatively, an integrating sphere can be utilized to measure the optical properties of sickle cell anemic blood (Appendix 4).

4.3.3 Results

For the two patient samples gathered, the patients' hematocrits were 22.9% and 24.5%. Therefore, both samples were diluted to only a hematocrit of 20%. In this preliminary analysis, we observed no statistically significant change in the DCS BFI between sickle cell anemic blood and healthy blood under fully oxygenated conditions (Figure 19).

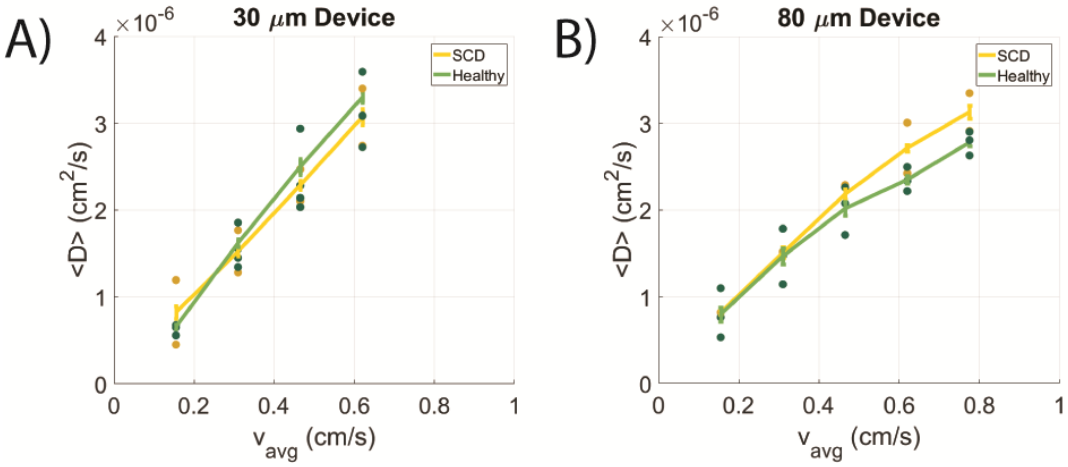

Figure 19: Mean and standard errors of the spatially-weighted diffusion coefficient ($\langle D \rangle$) vs the known average velocity (v_{avg}) for sickle cell anemic (yellow) blood and healthy (green) blood for the (A) 30×28 and (B) 80×75 μm. Individual patient data points are plotted as circles of the same color.

While we observed no statistically significant difference between SCD and healthy blood, more data samples will need to be taken. Future work will also employ utilizing an integrating sphere to quantify the optical properties of SCD blood.

Appendix 1: How to Construct the Microfluidic Phantom

Below are the instructions to construct the microfluidic phantom mold. These instructions are using previously published instructions on microfluidic making and optical phantom

making as a foundation[162,164]. The microfluidic device is first constructed by our collaborator and then we make the molds.

1. Pre-heat the oven or the hot plate at 80 degrees Celsius.
2. Use a scalpel to cut around the cured PDMS device and remove it from the wafer. Follow the pre-made markings of where to cut as the PDMS device will be opaque and it is easy to accidentally cut through the microfluidic channels.
3. After cutting, be sure to place the lid on the wafer to make sure that the wafer doesn't get contaminated by air particulates.
4. Cut a thin sheet of plain PDMS slightly larger than the device.
5. Take a marker and make a note of where the arteriole-like channels start and end on the top of the wafer. This is important since it will indicate where to place the DCS sensor.
6. Create inlet and outlet holes in the PDMS device using a 1.0 mm hole punch.
7. Clean the surfaces of the PDMS device and PDMS sheet with scotch tape.
8. Now insert these two pieces into the plasma cleaner. Insert the PDMS device facing upward since that will be placed on top of the PDMS sheet. Place both pieces on top of a taped glass slide.
9. When using the plasma cleaner, lock the device with the black valve. The arrow should point to the black valve because that's the direction of flow.
10. Turn the pump on and hook-on lid. Vacuum/Clean for 3 minutes with air.
11. Add the plasma bond for 1 min on high.

12. To unlock, turn the valve slowly with arrow and the lid will fall off. Go slow because otherwise the PDMS device may lift off from the glass slide due to the sudden gush of air.
13. Now the two strips can be stuck together. The oxygen plasma creates reactive species on the exposed surface of the PDMS which bond when brought into physical contact.
14. Take a marker and draw circles around the inlet and outlet tubing
15. Also use the marker to write on the PDMS sheet what the cross section of the device that was made.
16. After bonding, then place the device on a hot plate or oven at 80 degrees Celsius for 10 minutes.
17. Repeat these steps for each device.
18. During these steps, there are times when there will be breaks, which can be used to make a new batch of the PDMS/TiO_2/India Ink mixture to pour over the wafer.
19. Using a disposable cup, measure out TiO_2 and India Ink. This is the ratio that is used for these experiments, but these values can be changed using the equations described in Ayers et al.[164]
20. Then add the PDMS curing agent.
21. Mix these 3 materials together. Make sure they're well-mixed such that there is no TiO_2 powder settling at the bottom. Hand mixing is possible but also use the vortex machine.
22. Finally add the PDMS. This will be a very viscous substance. The ratio of PDMS to the PDMS curing agent is 10:1.

23. After mixing is complete, pour this mixture on top of the PDMS wafer and the blank petri dish, which will be used for future blank sheets.
24. Finally, vacuum the PDMS wafer and PDMS sheet in order to eliminate any air bubbles from the mixture by placing the PDMS wafer and sheet into a desiccator.
25. After placing in the vacuum chamber for at least an hour or until all air bubbles are gone, then place both the PDMS wafer and sheet in the oven. The devices will be cured overnight at 60 degrees Celsius.

Appendix 2: How to make DCS measurements with microfluidic devices

Here are the step-by-step instructions to run a microfluidic experiment after the microfluidic phantom devices have been constructed:

1. Take the marked microfluidic phantom and place it on top of the big phantom block (block to satisfy the semi-infinite medium criteria).
2. The phantom will already have circles drawn marking the location of the inlet and outlet tubing locations.
3. Take one blunt-point needle-tip (920050-TE, Metcal) and connect it to a syringe.
4. Now, two types of tubing will stem out from the syringe. Cut off a medium size length of tubing from the larger tubing (06418-02, Cole-Parmer Instrument Company) and insert it over the syringe tip.
5. Then cut off a large size length of smaller tubing (06417-11, Cole-Parmer Instrument Company), and insert it into the larger tubing.
6. Using the tweezers, insert the smaller tubing in the inlet of microfluidic phantom.
7. Cut off a larger size length of the smaller tubing and insert it into the outlet of the microfluidic phantom.

8. Tape the outlet of the smaller tubing to a beaker.
9. After, take the DCS probe holder and place it in the middle of the marked areas on the microfluidic phantom.
10. Take the DCS source and detector fibers and insert into the holes in the custom-made probe holder. The source-detector separation of the probe holder is 1 cm.
11. To make measurements, set the speed on the infusion pump (Harvard Appartus).
12. Wait 45 seconds.
13. While lightly pressing down on the sensor with the index and middle fingers on the probe holder, click on start on the DCS program. Now the software, will take 21 frames of data.
14. When acquiring data, make sure to stay still, as small vibrations could influence the DCS data.
15. After that round of data is complete, repeat steps 13 -16 for all velocities needed for the experiment.

Appendix 3: Ergodicity

Ergodicity was a theory that had to be accounted for when analyzing the microfluidic DCS data, which is also discussed in [73]. A system is said to be ergodic if time and ensemble averages of physical quantities associated with that system are identical. Problems may arise whenever the sample has static and dynamic scattering components[190]. Specifically, ergodicity presents a problem when one is measuring the temporal autocorrelation function, $g_2(\tau)$.

Temporal and spatial average can be better understood in this drawing below (Figure 20).

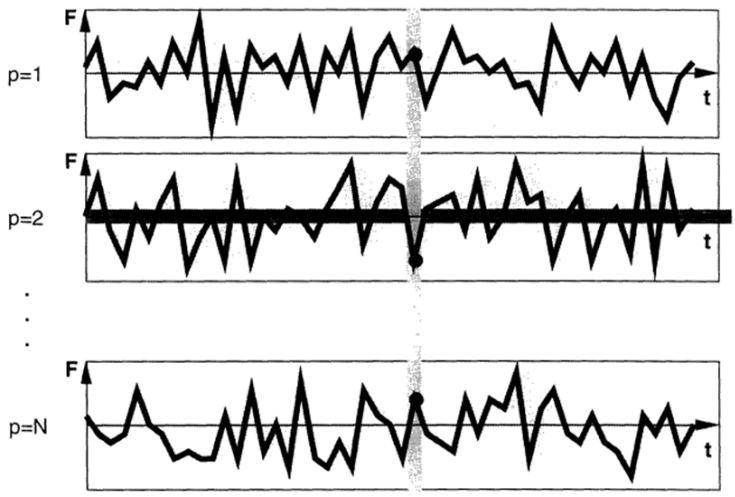

Figure 20: Drawing of temporal and spatial/ensemble average.

From the image above, for a temporal average, the system can be divided into sub-ensembles of some quantity F, where each p represents sub-ensembles. The thick horizontal line at p=2 represents the domain of time-averaging for that sub-ensemble. The temporal average can be mathematically written as: $\langle X_p \rangle_T = \lim_{T\to\infty} \frac{1}{T} \int_0^T dt\, X_p(t)$. In contrast for a spatial average, from the figure above, the vertical line across all sub-ensembles represents the ensemble averaging that will take place. The value of F at time t is averaged over all sub-ensembles of the system. The spatial average can be mathematically written as: $\langle X \rangle_E = \lim_{P\to\infty} \frac{1}{P} \sum_{p=1}^{P} X_p(t)$, where X_p is equivalent to an average over the sub-ensemble. The mathematical steps below show that the spatial average of a time-averaged quantity is equal to the spatial-averaged quantity:

$$\left\langle \langle \boldsymbol{X_p} \rangle_{\boldsymbol{T}} \right\rangle_{\boldsymbol{E}} = \left\langle \lim_{T\to\infty} \frac{1}{T} \int_0^T dt\, X_p(t) \right\rangle_E$$

$$= \lim_{P\to\infty} \frac{1}{P} \sum_{p=1}^{P} \lim_{T\to\infty} \frac{1}{T} \int_0^T dt\, X_p(t)$$

$$* \lim_{P\to\infty} \sum_{p=1}^{P} x = \sum_{p=1}^{\infty} x$$

- $\sum_n \int f_n x dx = \int \sum_n f_n x dx$, for all x that is positive

$$= \frac{1}{P} \sum_{P=1}^{\infty} \lim_{T \to \infty} \frac{1}{T} \int_0^T dt X_p(t)$$

$$= \sum_{P=1}^{\infty} \int_0^{\infty} dt X_p(t)$$

$$= \int_0^{\infty} dt \sum_{P=1}^{\infty} X_p(t)$$

$$= \int_0^{\infty} dt \langle X \rangle_E = \langle \langle \boldsymbol{X} \rangle_{\boldsymbol{E}} \rangle_{\boldsymbol{T}}$$

A sample is non-ergodic when there's a solid-like media involved. In this situation, the scatterers are localized near fixed average positions and are only able to execute limited Brownian motions about these positions. One sample of this non-ergodic system will be trapped in a restricted region, "sub-ensemble," whose location and extent are determined respectively by their average positions of the scatterers and the magnitudes of their displacements. Different samples will contain scatterers in different average positions and will be described by different sub-ensembles. In our microfluidic phantom platform, the non-ergodic media is the solid PDMS/TiO_2/India Ink block that each microfluidic device rests on to simulate a semi-infinite medium. The effects of non-ergodicity can be seen by our experimental $g_2(\tau)$ curves (Figure 13a). To reduce the effects of non-ergodicity, we objectively isolate our fits of $g_2(\tau)$ to be ≥ 1.25 to ensure that our theoretical models fit for the early portion of the autocorrelation curve that is dominated by photons that have sampled the dynamic portion of the microchannels[73].

Appendix 4: Integrating Sphere to Assess the Optical Properties of Sickle Blood

DCS is a light-based optical modality that measures an index of cerebral blood flow by measuring the shear-induced diffusion of red blood cells[66]. For the first time, we demonstrated the application of DCS to measure sickle cell anemic children[182]. However, sickle cell anemia is a red blood cell disorder. Therefore, we want to explore how our

measurements of blood flow are affected by sickle red blood cell properties. Our previous experiments using the microfluidic phantom were accomplished by flowing healthy blood[92], where we know the optical properties (absorption and scattering) of whole blood as a function of light wavelength[169]. Next, we were interested in repeating these microfluidic experiments while flowing sickle cell blood. However, the optical properties of sickle cell whole blood have not been published. Therefore, we needed to utilize an integrating sphere to measure the optical properties of sickle cell whole blood.

Experimental Setup and Data Acquisition

An integrating sphere consists of a hollow spherical shell coated on the inside with a highly reflecting diffuse coating. The integrating sphere's diffuse coating and multiple reflections cause any light introduced into the sphere to produce uniform irradiance and radiance of the wall of the sphere. For our experiments, we utilized an integrating sphere from Labsphere (RT-060-SF) and made both reflectance and transmittance measurements for our blood samples using a single beam configuration.

The setup of the integrating sphere includes a collimated light source (Tungsten halogen lamp, Ocean Optics) and spectrometer (Flame NIR Spectrometer, Ocean Optics). To calculate the absorption and reduced scattering coefficients of a sample, two measurements need to be made by measuring the sample in reflectance and transmittance mode. In the reflection configuration, reflectance is the light that is reflected by the sample and normalized by the incoming light. However, in the transmittance configuration, the incoming light hits the sample before it enters the integrating sphere[1]. Both measured reflectance and transmittance have no units.

To make these measurements in the transmittance and reflectance configurations, I followed section 8 the IAD manual provided by Scott Prahl[1]. At a high level, I first made three transmittance measurements: 1) empty port, 2) dark measurement, and 3) sample measurement in transmittance configuration (Figure 21). Next, I made three reflectance measurements: 1) empty port, 2) measurement with the reflectance standard, and 3) sample measurement in the reflectance configuration.

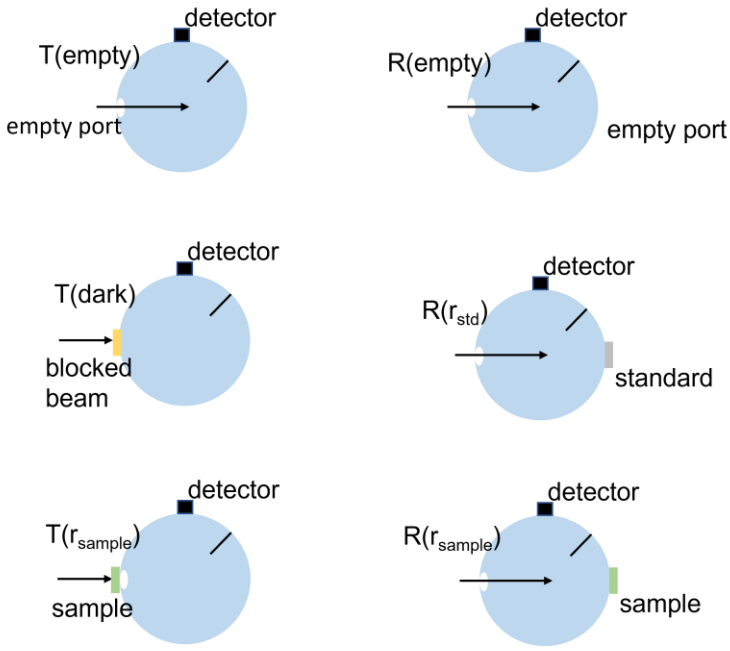

Figure 21: Adapted from Prahl's IAD manual[1] on how to make the reflectance and transmittance measurements for a single integrating sphere.

From these 6 measurements, the output is a plot of the intensity counts as a function of wavelength. To calculate transmittance, we use this equation, based off of our acquired data[1]:

$$M_T = \frac{T_{sample} - T_{dark}}{T_{empty} - T_{dark}}. \quad (29)$$

To calculate reflectance, we use this equation:

$$M_R = r_{std} \cdot \frac{R_{sample} - R_{empty}}{R_{std} - R_{empty}}, \quad (30)$$

where r_{std} is known for our experimental setup to be 0.992. These calculated transmittance and reflectance values are used as inputs for the publicly available data analysis software – IAD program[1]. The inverse adding-doubling method solves the radiative transport equation. At a high level, the IAD consists of the following steps: 1) Guess a set of optical properties (μ_a and μ_s), 2) Calculate the reflectance and transmittance values for this set of optical properties using the adding-doubling method, 3) Compare the calculated values against the measured reflectance and transmittance values, 4) Repeat until a match is made[191].

Chapter 5: Subarachnoid Hemorrhage and DCS

5.1 Introduction

Subarachnoid hemorrhage (SAH) is an uncommon cause of stroke that disproportionately contributes to increased mortality and morbidity. Globally, the incidence of SAH is estimated at ~8:100,000 people annually, with a mortality rate of ~30%[192,193]. One common complication of non-traumatic SAH is cerebral vasospasm, which is described as an aberrant constriction of the cerebral vasculature that can occur as soon as post-bleed day 3 and can persist up to 21 days[194]. This maladaptive response contributes to a decrease in cerebral blood flow (CBF)[195,196] and is associated with the development of a secondary stroke known as delayed cerebral ischemia (DCI)[197]. DCI affects up to 30% of SAH patients and leaves them with a reduced quality of life due to motor deficits and/or cognitive dysfunction[198]. Because ischemic conditions can lead to poor functional outcome, treating cerebral vasospasm and avoiding DCI remains a major clinical unmet need after SAH.

Calcium channel blockers (CCB), which act on smooth muscle cells to dilate the vasculature, have been long investigated for their potential role in the treatment of vasospasm and prevention of DCI. Indeed, the only guideline recommended treatment for prevention of DCI is oral administration of the dihydropyridine CCB nimodipine[194]. However, once vasospasm or DCI develop, there is no proven treatment to address them.

Recent data within Emory University Hospital suggest that the intrathecal (IT) delivery of the CCB nicardipine may have a role in a reactive (rather than a preventative) treatment approach to address cerebral vasospasm and avoid DCI[199]. This approach has the advantage of avoiding deleterious systemic effects, which are common with oral and

intravenous CCBs[200]. An intermittent and titratable IT nicardipine regimen was shown to be associated with proximal vessel vasodilation, reduced risk for DCI and improved long-term functional outcomes[199,201]. However, the macrovascular vasodilation itself (as quantified by a reduction in TCD blood flow velocity) was not associated with outcome[199]. Therefore, the underlying mechanism driving the effect of IT nicardipine on patient outcomes remains unclear.

Both DCI and, to a more controversial extent, vasospasm are thought to occur on the microvascular level[201–204], yet, the efficacy of IT nicardipine has only been assessed to date at the macrovascular level[199,201,205–207]. While vascular tone at the arteriolar and capillary level is governed by calcium-dependent processes within astrocytic podocytes and pericytes[208,209], intrathecal delivery of nicardipine does not guarantee the drug reaches smaller blood vessels that travel and bifurcate within the subarachnoid space. Understanding the influence of IT nicardipine on the microvasculature is needed to improve our mechanistic understanding of the treatment's effect.

Current neuroimaging modalities to characterize the microvascular hemodynamic response to IT nicardipine are limited in the critical care environment. While perfusion magnetic resonance imaging (MRI), positron emission tomography (PET), and/or computed tomography (CT) can quantify microvascular cerebral blood flow, cost, the need for patient transport, and the lack of continuous monitoring limit their feasibility. Other indirect measures of microvascular flow like continuous, non-invasive near-infrared spectroscopy (NIRS) measurements of hemoglobin oxygen saturation, or invasive brain tissue oxygen monitors (e.g., Licox®) have been shown to be poor surrogates of cerebral perfusion in brain injured patients[54,210–212].

In this study, we employ a non-invasive, well-validated optical technique known as diffuse correlation spectroscopy (DCS) to measure regional microvascular cerebral blood flow[47,66,115,158,213]. In DCS, a coherent near-infrared light source is placed on the tissue surface. This input light multiply scatters before detection at some distance away on the tissue surface. Scattering off of moving red blood cells within the tissue leads to temporal fluctuations in detected light intensity. These temporal fluctuations are quantified through a normalized temporal intensity autocorrelation function, $g_2(\tau)$, that is fit to simple analytical models, known as correlation diffusion theory, to extract a blood flow index (BFI) [46,47]. Although the units of BFI (cm^2/s) do not match the traditional units of blood flow (mL/min/100g), numerous validation studies against various "gold-standard" modalities (i.e., Xenon-CT, MRI, PET) in adults, children, and animals demonstrate that BFI correlates with cerebral blood flow measured by other modalities[58,67,76,158,214,215].

5.2 DCS-measured Blood Flow Response to the First Dose of IT Nicardipine is Associated with Patient Outcomes

We employed diffuse correlation spectroscopy (DCS) to measure regional microvascular cerebral blood flow in adult subarachnoid hemorrhage patients receiving IT nicardipine[47,115,158]. We use DCS to test the hypothesis that IT nicardipine increases microvascular cerebral blood flow from pre-administration levels in the absence of systemic blood pressure changes. We also explore the relationship between microvascular flow measured by DCS and macrovascular flow velocities measured by transcranial Doppler ultrasound.

5.2.1 Materials and Methods

Study design

For this observational study, we enrolled non-traumatic subarachnoid hemorrhage (SAH) adult patients in the neurocritical care unit at Emory University Hospital (Atlanta, GA, USA) who had an external ventricular drain (EVD) placed as part of their usual care. This study was approved by the Emory University Institutional Review Board (IRB00107474). Written, informed consent was obtained prior to study initiation from all patients or their surrogates.

Once consented, patients were only included for monitoring if 1) they developed cerebral vasospasm, and 2) they were deemed to require IT nicardipine by the treating clinical teams (neurocritical care, vascular neurosurgery) as part of usual care. Diagnosis of cerebral vasospasm was confirmed by either transcranial Doppler ultrasound (TCD), computed tomography (CT) angiography, or digital subtraction angiography, according to accepted definitions To quantify the cerebral hemodynamic effects of intrathecal nicardipine, continuous measurements of microvascular cerebral blood flow were made with diffuse correlation spectroscopy (DCS) during the first dose of IT nicardipine treatment.

DCS measurements were made with a custom-built instrument comprised of an 852 nm long coherence laser (iBEAM smart, TOPTICA Photonics, Farmington, NY), eight photon-counting avalanche photodiodes (SPCM-AQ4C-IO, Perkin-Elmer, Quebec, Canada), and a counter/timer data acquisition board (PCIe-6612, National Instruments)[102]. Detected photon counts were used to estimate an intensity autocorrelation function, $g_2(\tau)$, with a custom software correlator[216] (LabVIEW, National Instruments).

The patient interface for these measurements consisted of a custom-made, flexible sensor that contained a 1 mm fiber bundle source (FTIIG23767, Fiberoptics Technology,

Pomfret, CT) spaced 2.5 cm from a bundle of seven 4.4 μm single-mode detection fibers (780HP, Thorlabs, Newton, NJ) (Figure 22a). All fibers were coupled to right angle mirrors (MRA05-E03, Thorlabs, Newton, NJ) to allow the fibers to lie flush with the forehead. The sensor was placed on the forehead of the hemisphere with the higher MCA velocities on TCD, suggesting worse cerebral vasospasm. It was secured with medical tape (3M^{TM} Durapore Surgical Tape) and further secured with a head strap (Figure 22b,c). If vasospasm was observed in both hemispheres, the sensor was placed on the hemisphere with higher detected light intensities to maximize the signal-to-noise ratio (SNR). The sensor was positioned up to 5 minutes prior to IT nicardipine initiation and monitoring at 0.3 Hz ensued for up to 90 minutes post-administration. Monitoring was discontinued prior to 90 minutes if the patient received secondary vasodilators (e.g., oral nimodipine, intravenous milrinone) or if the sensor had to be removed due to a clinical event (e.g., vomiting). The entire dataset was discarded if monitoring had to be discontinued <15 min after nicardipine administration.

To determine the effect of nicardipine on microvascular cerebral blood flow, the measured intensity autocorrelation functions, $g_2(t,\tau)$, at time, t, and delay time, τ, were fit for a blood flow index (BFI(t)) using the semi-infinite solution to the correlation diffusion equation[47]. For these fits, we assumed a constant absorption coefficient, reduced scattering coefficient, and tissue index of refraction of 0.2 cm^{-1}, 10 cm^{-1}, and 1.4, respectively[83]. Fits were constrained to $g_2(t,\tau) > 1.2$ to increase sensitivity to the cerebral layer[134]. Data were excluded if the detected light intensity was < 8 kHz, due to poor signal-to-noise ratio (SNR). Finally, relative change in cerebral blood flow (rCBF) as a function of time was calculated as:

$$rCBF(t) = \frac{BFI(t) - BFI_{baseline}}{BFI_{baseline}} \times 100\%, \quad (31)$$

where $BFI_{baseline}$ is the temporal mean of $BFI(t)$ over the five-minute baseline immediately prior to IT nicardipine administration.

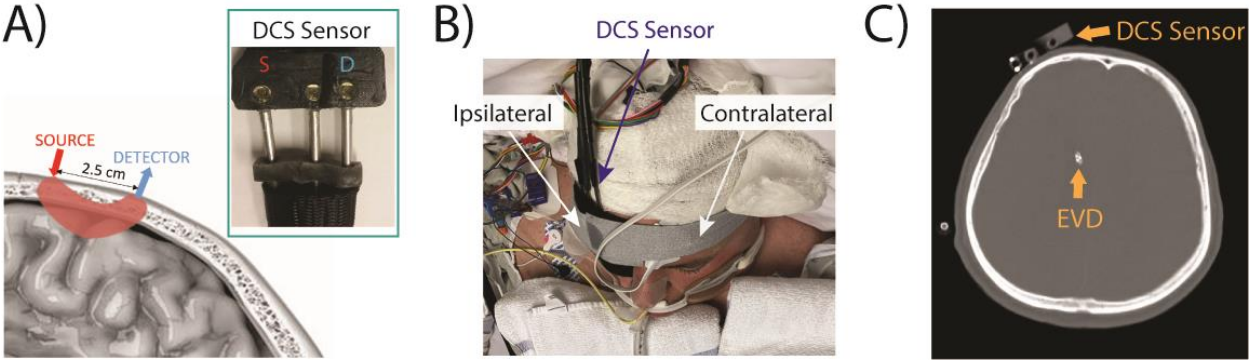

Figure 22: ***Diffuse correlation spectroscopy (DCS) experimental setup*** *(**A**) Pictorial representation of the DCS sensor on the scalp and the optical interrogation path for the source and detector geometry (pink shaded region), along with a photograph of the non-invasive DCS sensor (inset), (**B**) The DCS sensor was secured to the patient's forehead, typically on the side with higher TCD velocities, suggesting more severe cerebral vasospasm, (patient image obtained with specific consent). (**C**) Representative CT scan showing typical placement of the DCS sensor and external ventricular drain (EVD).*

Measurements of blood pressure, heart rate, and intracranial pressure

To investigate the potential confounding systemic influences of blood pressure and heart rate, as well as any influence of intracranial pressure, on the cerebral hemodynamic response to IT intrathecal nicardipine, we simultaneously captured blood pressure, heart rate, and intracranial pressure. Per standard clinical care, continuous arterial blood pressure was measured with a transducer in the radial artery. Blood pressure was captured at 125 Hz with an analog to digital converter board (NI USB-6343) beginning 5 minutes before the first dose of IT nicardipine and continuing for up to 90 minutes post-administration. This data was time synced with DCS measurements of cerebral blood flow. Beat-to-beat values of systolic, diastolic, and mean blood pressure (MAP), as well as heart rate (HR),

were derived from the arterial blood pressure waveform in post-processing using the *delineator* function[217] in MATLAB (MathWorks, Natick, MA).

Intracranial pressure (ICP) was measured with a transducer in the EVD (INS8401, Integra, Plainsboro, NJ). In general, the EVD was opened to allow for spontaneous CSF drainage, thus continuous ICP measurements were not available. However, the EVD was clamped for the first 30 minutes after the administration of IT nicardipine, as well as briefly before and after this 30-minute window. Thus, intracranial pressure was stochastically captured by hand every 1-15 minutes for up to 90 minutes post-administration.

To quantify the effect of IT nicardipine on HR, MAP, and ICP, we estimated the change in each parameter from pre-administration levels, e.g., $\Delta\, MAP(\,t) \;-\; MAP(\,t) - MAP_{\,baseline}$, where $MAP_{\,baseline}$ is the temporal mean of *MAP(t)* over the five-minute baseline immediately prior to IT nicardipine administration.

Measurement of macrovascular blood flow velocity

To investigate the relationship between microvascular and macrovascular perfusion, we compared the average DCS-measured BFI in the 5 minutes prior to IT nicardipine administration to TCD measures of mean cerebral blood flow velocity in the middle cerebral artery (MCA) and anterior cerebral artery (ACA). We focused our investigation on these vessels because our DCS sensor was positioned near the intersection of the MCA and ACA vascular territories (Figure 22). TCD data were acquired per clinical care on the morning of the study, prior to IT nicardipine administration (Dolphin IQ, Viasonix, TN). For each vessel, the maximum value of the time-averaged mean velocities over the range of depths quantified was used to compare with DCS[218].

Statistical analysis

To test our hypothesis that IT nicardipine increases microvascular cerebral blood flow in the absence of systemic changes, we first graphically explored rCBF, MAP, HR, and ICP as a function of time post nicardipine administration. Data were downsampled to 10-minute intervals to aid in visualization. Next, a linear mixed effects model was applied to the downsampled data to determine significant trends in each measured variable with time, where we accounted for repeated measures within participants. For the outcomes MAP, HR, and ICP, we modeled subject-specific intercepts and slopes. For outcomes that were relative to time zero (e.g., rCBF, $\Delta\, MAP$), we modeled subject specific slopes. The model R^2 was used to determine goodness of fit. Further, because we observed a heterogeneous response of rCBF to nicardipine, we used a latent class mixture model[219] (LCMM) to classify CBF responses into unobserved groups (i.e., latent classes) with similar, more homogenous patterns of rCBF. In this model, time post-nicardipine initiation was treated as the linear fixed effect, and the number of latent classes (e.g., distinct rCBF trajectories) was specified *a priori*. Given our relatively small sample size, we tested both 2 and 3 latent class solutions. No differences in the log-likelihood statistic were observed between the 2- versus 3-class solutions; therefore, we employed a 2-class solution. Patients were assigned to a latent class (e.g., response pattern group) based on the class with the highest posterior probability of class membership. We used Chi-square tests and Wilcoxon rank sum tests to test for differences between these empirically derived classes in age, sex, SAH grade, mean arterial pressure pre-administration, TCD velocities pre-administration, and incidence of DCI.

To determine the relationship between microvascular cerebral blood flow measured with DCS and macrovascular cerebral blood flow velocity measured with TCD,

Spearman's rank coefficient, r_s, was used to assess the extent to which a linear model explains the variability in the relationship between $BFI(r=2.5\ cm)_{baseline}$ and mean blood flow velocities in the middle cerebral artery (MCA) and anterior cerebral artery (ACA).

Data are reported as mean $\pm$ standard deviation unless otherwise stated. LCMM analysis was performed with the LCMM package in R (version 3.5.2, rproject.org); all other analyses were performed in MATLAB. Statistical significance was assessed at the 0.05 level.

5.2.2 Results

Between April 1, 2019 and October 31, 2021, 57 patients with non-traumatic SAH (aneurysmal or diffuse pattern angiogram negative) admitted to the neurocritical care unit at the Emory University Hospital were consented. 37 of these 57 patients developed clinically significant cerebral vasospasm that required treatment with IT nicardipine, as determined by the treating attending physician. The CBF response to the first dose of IT nicardipine was monitored in 27 out of 37; 10/37 were excluded due to availability of the research-based DCS device. Of those 27 monitored with DCS, 20 (74%) were included in our final analysis; the remaining 7 datasets were excluded due to measurement duration < 15 min. Of these seven, premature discontinuation of monitoring was caused by patient discomfort related to the intrathecal administration and EVD clamping (n=3), failure to properly secure the DCS sensor on the patient's forehead (n=3), or administration of oral nimodipine that induced confounding effects on CBF (n=1). Average duration of DCS monitoring post-nicardipine was 82.7 ± 23.2 min.

Patients were mostly female (70%), with a mean $\pm$ standard deviation age of 48.5 $\pm$ 10.1 years (Table 4). Aneurysm location and grade severity were heterogeneous, as

described in Table 5. An IT nicardipine dose of 4 or 5 mg was administered every 6-8 hours for an average of 36 ± 20 doses according to the decision of the attending physician, as part of usual care. One patient had evidence of DCI on CT prior to nicardipine initiation. Four out of 20 developed new DCI on the latest imaging available (up to 6 weeks post-bleed).

Table 4: ***Summary of Patient Cohort.*** *Data is reported as mean ± standard deviation or N (%)*

Demographic Information and Risk Factors	
Age (y)	48.5 ± 10.1
Sex – Female, N (%)	14 (70%)
Race	
African American	11 (55%)
White	8 (40%)
Asian	1 (5%)
Hispanic	2 (10%)
Hypertension, N (%)	12 (60%)
Coronary artery disease, N (%)	1 (5%)
Diabetes mellitus, N (%)	1 (5%)
Tobacco use, N (%)	12 (60%)
Dyslipidemia, N (%)	2 (10%)
Depth to brain (cm)	1.2 ± 0.3
Total IT nicardipine doses (N)	36 ± 20

Table 5: ***Summary of patient demographics and clinical characteristics****. Sex: M, male; F: female; SAH grade at admission: H&H, Hunt and Hess grade; WFNS: World Federation of Neurosurgical Societies grade; mFG: Modified Fisher Grading Scale; DCI: delayed cerebral ischemia; R: right; L: left; PCom: posterior communicating artery; Ant: Anterior; PICA: posterior inferior cerebellar artery; ACom: anterior communicating artery; MCA: middle cerebral artery; SCA: superior cerebellar artery; ICA: internal carotid artery. DCI was determined based off the latest imaging available (up to 6 weeks). One patient (marked as *) developed DCI prior to treatment.*

Patient Clinical Characteristics

Sex	Age	H&H	WFNS	mFG	Aneurysm Location	Aneurysm Treatment	Sensor Location	DCI	DCI Location
F	61	3	4	4	R PCom	Endovascular	L Frontal	No	
F	47	3	4	4	R Ant Choroidal	Clip ligation	R Frontal	Yes	R MCA
F	62	4	5	4	Angio Negative		L Frontal	Yes	R MCA
F	62	1	2	4	L PCom	Clip ligation	L Frontal	No	
F	37	4	4	4	R Vertebral	Endovascular	R Frontal	No	
M	44	5	5	2	R PICA	Endovascular	R Frontal	No	
F	49	3	2	4	R PCom	Clip ligation	R Frontal	No	
M	56	3	2	4	L PCom	Endovascular	L Frontal	No	
F	58	4	4	4	ACom	Endovascular	R Frontal	Yes	L ACA
M	33	1	1	4	L MCA	Endovascular	L Frontal	No	
F	35	3	2	2	L MCA	Endovascular	L Frontal	Yes	L & R ACA
M	50	4	4	4	L SCA	Clip ligation	L Frontal	No	
F	58*	5	5	4	R MCA	Clip ligation	L Frontal	Yes	R SCA
M	43	3	4	4	ACom	Endovascular	L Frontal	No	
F	52	3	2	4	ACom	Endovascular	R Frontal	No	
M	37	3	2	4	ACom	Endovascular	L Frontal	No	
F	64	1	2	4	R MCA	Endovascular	R Frontal	No	
F	44	4	4	4	L PCom	Endovascular	L Frontal	No	
F	38	5	5	4	L ICA	Endovascular	R Frontal	No	
F	40	1	2	4	L MCA	Clip ligation	L Frontal	No	

Average MAP prior to IT nicardipine administration was 102.1 $\pm$ 13.1 mmHg; average heart rate was 79.5 $\pm$ 14.4 bpm. Post-administration, no significant trends with time were observed for MAP or heart rate (both $p>0.05$, Figure 23). Average ICP at start of IT nicardipine and 30 minutes post-administration were 10.4 $\pm$ 7.9 mmHg and 10.5 $\pm$ 4.9 mmHg, respectively ($p>0.05$); ICP remained unchanged from IT nicardipine administration until the next dose ($p=0.8$, data not shown).

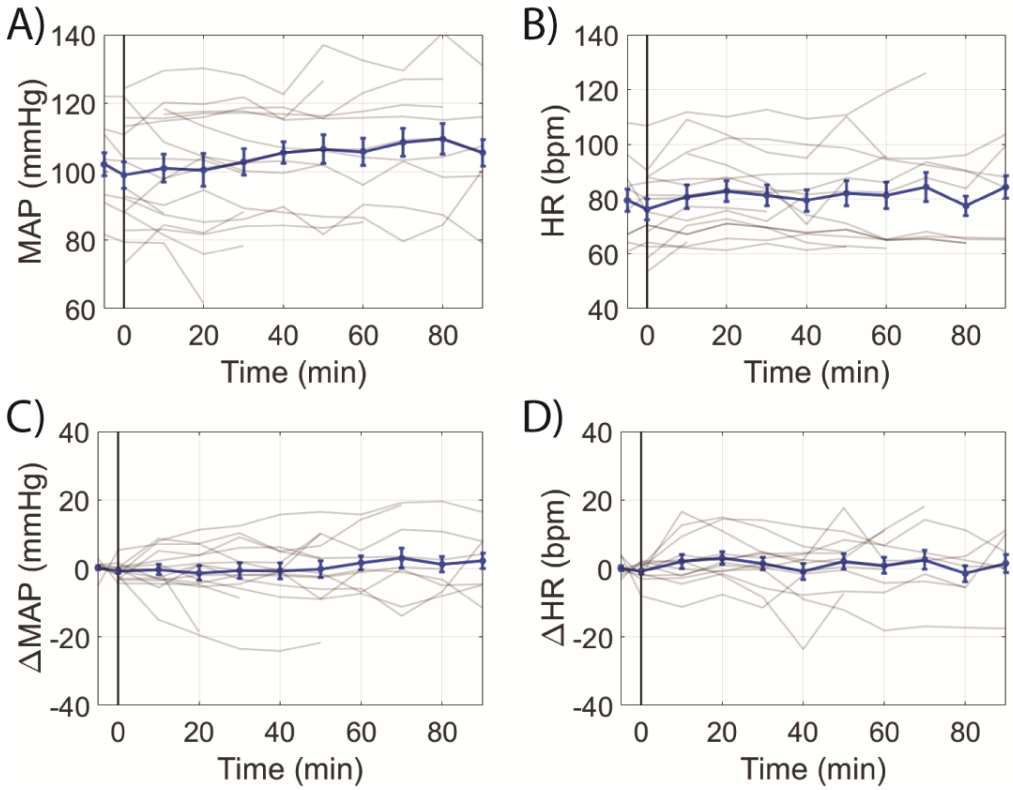

Figure 23: ***Effect of IT nicardipine on systemic blood pressure and heart rate****: Mean arterial pressure (MAP,* ***A****), heart rate (HR,* ***B****), change in MAP from pre-administration levels (ΔMAP,* ***C****), and change in HR from pre-administration levels (ΔHR,* ***D****) as a function of time post-administration of IT nicardipine. Thin grey lines in each subplot denote individual patient responses and thick blue lines denote the mean and standard error across all patients. The black vertical line at time = 0 denotes the start of treatment.*

We found that microvascular cerebral blood flow measured with DCS significantly increased with time after IT nicardipine administration ($p<0.001$), although significant response heterogeneity was noted across subjects (Figure 24). Using a latent class mixture model, 19/20 patients were classified into two distinct classes of CBF response; Class 1 (n = 6, in red in Figure 24) showed minimal change in rCBF post-administration, whereas Class 2 (n = 13, in green in Figure 24) exhibited a steady increase in rCBF over the course of monitoring. Note, for this analysis, visual inspection revealed 1 distinct trajectory that the LCMM model was overly sensitive to (shown in blue in Figure 24); this outlier

trajectory was excluded from LCMM analysis. No significant differences in age, sex, SAH grade, depth to brain, baseline MAP, baseline HR, baseline ICP, baseline TCD maximal mean velocities at any depth, or relative change in TCD velocities were seen between the LCMM identified classes of CBF response to nicardipine (all $p>0.05$). However, the frequency of DCI was significantly different between classes ($p<0.001$); 5/6 subjects in class 1 had DCI, 4 of whom developed new DCI on the latest imaging available up to 6 weeks post-bleed and 1 of whom started with DCI prior to nicardipine, while 0/13 subjects in Class 2 had DCI. Further review of the excluded outlier revealed that the CBF trajectory correlated with these trends; this patient had a sharp increase in CBF, similar to those in class 2, and did not develop DCI.

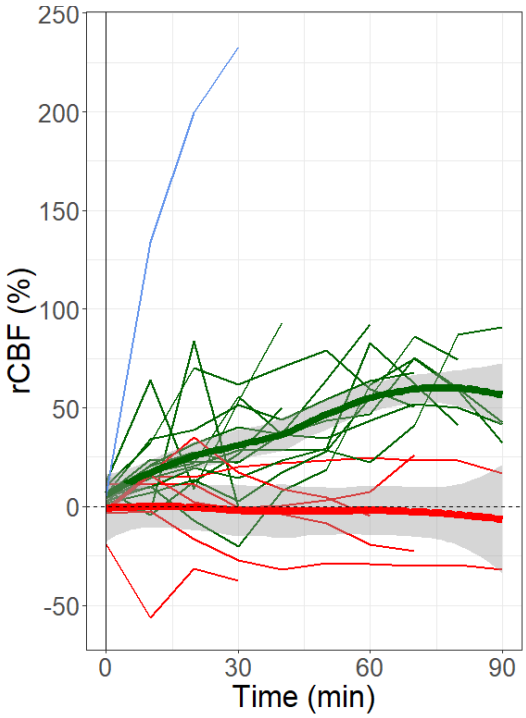

Figure 24: ***Latent class trajectory groups of relative changes in cerebral blood flow (rCBF) as a function of time post-IT nicardipine administration****. Two distinct classes of rCBF response were identified by the model: Class 1 (n=6, in red) showed minimal change in rCBF post-nicardipine, whereas Class 2 (n=13, in green) exhibited an increase in rCBF over the course of monitoring. The model was overly sensitive to one distinct trajectory (in blue); this outlier trajectory was excluded from analysis. Here, thin*

lines denote individual patient responses, while thick lines denote the model best fit for each response class.

19 out of 20 patients in our cohort had TCD measurements performed on the morning of IT nicardipine initiation (4.3 ± 0.1 hours, time difference between TCD and DCS measurements). In this subset of patients, we observed a significant positive correlation between mean blood flow velocity in the middle cerebral artery (MCA) and baseline BFI measured by DCS (r_s = 0.68, p = 0.0012) (Figure 25a). Similar correlation was not seen between mean flow velocity in the ACA and baseline BFI (p=0.176, Figure 25b).

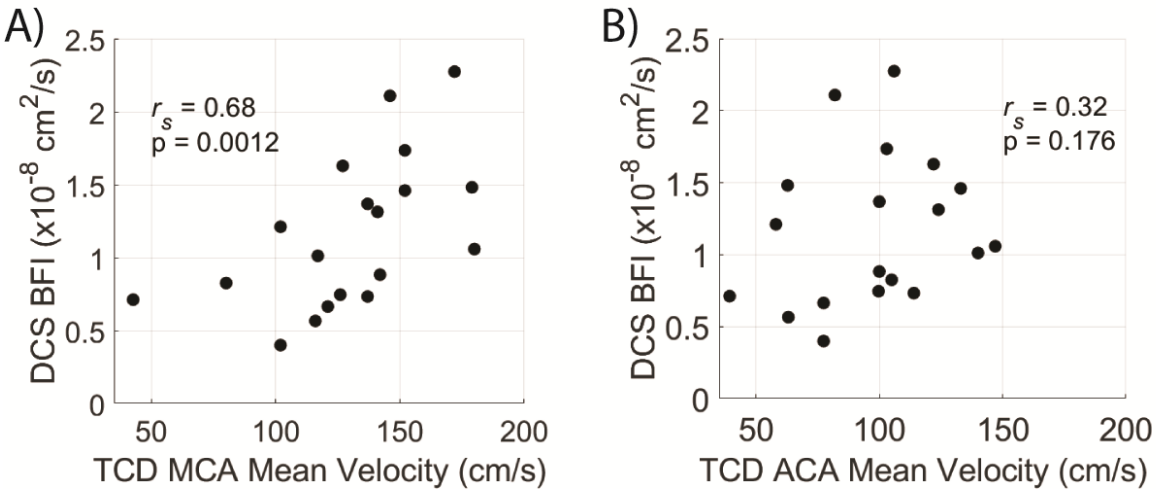

Figure 25: ***Relationship between micro and macrovascular blood flow. (A)*** *Mean blood flow velocity in the middle cerebral artery (MCA) measured by transcranial Doppler ultrasound (TCD) versus diffuse correlation spectroscopy (DCS)-measured blood flow index (BFI)****,*** *n=19* ***(B)*** *Mean blood flow velocity in the anterior cerebral artery (ACA) measured by TCD versus DCS-measured BFI, n=19.*

5.2.3 Discussion

In this study, we used DCS to quantify the response of microvascular cerebral blood flow to intrathecal administration of nicardipine in patients with cerebral vasospasm after subarachnoid hemorrhage. We found that on average microvascular CBF increased over

the 90 minutes of monitoring. This increase in CBF was observed in the absence of systemic changes in blood pressure or heart rate, suggesting that the cerebral hemodynamic response is likely due to a local drug effect rather than systemic changes.

While CBF increased on average, we observed substantial heterogeneity in the response across patients. This heterogeneity was quantitatively explored using a latent class mixture model that identified two distinct classes of CBF response – Class 1, wherein minimal-to-no change in CBF was observed, and Class 2, wherein a steady increase in CBF was observed. Interestingly, this differential CBF response was significantly associated with DCI. No patient with increased CBF after IT nicardipine developed DCI, while 5/6 patients whose CBF did not respond to IT nicardipine had DCI. Although these are preliminary observations, these data suggest that the CBF response to the first dose of IT nicardipine could be a novel biomarker for treatment response and DCI risk, alerting clinicians to consider alternative interventions. Identifying high-risk patients, or those who do not respond to a specific treatment in real-time, is of high importance, as previous studies have demonstrated that DCI development was associated with poor functional outcome after SAH[198,220,221].

Several possible mechanisms may explain the lack of CBF response to nicardipine in the Class 1 subset. Many vasospasm-independent mechanisms, including microthrombosis, venous outflow obstruction, and spreading depolarization, may be present in these patients that are unaffected by nicardipine[222,223]. Alternatively, the additional volume of drug and diluent into the cranial vault could potentially decrease cerebral perfusion in certain patients. Further, the timing of treatment may influence the CBF response. Using a rabbit SAH model, Vorkapic et al.[224] demonstrated two phases of

vasospasms – an early pharmacologically reversible phase and a later irreversible phase. During the acute reversible vasospasm stage, cerebral vasoconstriction could be reversed by calcium channel blockers[224]. However, with time, as organic changes such as intimal proliferation, edema, and degeneration occur, the efficacy of pharmacological interventions is reduced[205,224]. Regardless of mechanism, coupling DCS with a pharmacological challenge may be a valuable risk-stratification tool to measure a treatment effect in the microvascular bed alongside TCD assessment of the macrovasculature to better guide clinical decisions and minimize DCI after SAH.

A secondary aim of this study was to investigate the relationship between DCS measurements of microvascular blood flow and TCD measurements of macrovascular flow in the context of the complicated CBF dynamics after SAH. We observed a significant positive correlation between the DCS-measured blood flow index measured prior to nicardipine administration and the TCD-measured mean blood flow velocity in the MCA measured on the morning of DCS monitoring. Similar correlation was trending towards significance in the ACA ($p=0.176$). Of note, the sensor was positioned over the watershed area between the ACA and MCA territories. On the surface, these positive correlations were somewhat surprising, as TCD blood flow velocities are elevated in the presence of vasospasm due to the narrowing of the arteries, which could lead to a *reduction* in microvascular blood flow. However, previous work has demonstrated that microvascular blood flow is typically only significantly reduced in the setting of severe vasospasm[225], while the majority of our cohort was classified as either mild, moderate, or no vasospasm in the MCA and ACA. Thus, the correlation between DCS and TCD measurements suggests that the coupling between microvascular and macrovascular perfusion in the MCA

(and possibly ACA) territory remains intact in our patient cohort. In the future, measurements of microvascular perfusion with DCS in concert with macrovascular TCD assessments may serve as a role in dissecting complicated CBF dynamics after SAH, with the distinct advantage of providing non-invasive, dynamic monitoring over several hours rather than a snapshot in time measurement like TCD.

Our study has several limitations. First, by design, this was an observational study that involved dynamic monitoring of patients treated per usual care, and thus these results should be confirmed in the setting of a randomized controlled trial, which is currently in the planning stages at EUH. Second, seven (26%) monitoring sessions were discarded from analysis. While this incidence is appreciable, we note we used this pilot study to continually improve the DCS patient interface to maximize patient comfort and signal-to-noise. With the improvements developed in this study, we anticipate a significantly lower discard rate with continued future enrollment. Numerous novel wearable sensor designs for diffuse optics applications have been recently developed that DCS can capitalize on to improve wearability and reduce motion artifacts[226,227]. Third, based on previous reports of a short half-life of nicardipine[206,228], we limited monitoring to up to 90 minutes, although monitoring was discontinued prior to 90 min in several patients due to instrument availability or the administration of therapeutic agents known to exert confounding influences on cerebral hemodynamics (e.g., oral nimodipine). With a larger sample size and extended monitoring, we will explore the necessary duration of monitoring required to robustly distinguish the dichotomy between the patients who did and did not respond favorably to IT nicardipine. Moreover, future work should characterize how the vasodilatory effects of IT nicardipine change as a function of dose during the roughly 8-

day treatment duration. Third, with our current DCS instrument, we were limited by SNR to a single measurement location, which we selected to be hemisphere in which higher TCD velocities were measured (suggesting worse vasospasm). In the future, increasing the number of laser sources and detectors may enable studying the cerebral hemodynamic effects of nicardipine in multiple locations around the head simultaneously. Lastly, to analyze our DCS data, we employed the semi-infinite solution to the correlation diffusion equation[47], which models the head as a homogenous medium. While the strong correlation with TCD suggests that this approach provides a suitable first order approximation, future work should employ multi-layer modeling[90,92,93] that better models the head as a layered medium (i.e., scalp, skull, cerebral spinal fluid, and brain) to enhance sensitivity to cerebral perfusion and minimize contributions from extracerebral layers.

Finally, future work will utilize employing the hematocrit correction equations developed in Chapter 4 to account for the influence of hematocrit in our SAH cohort. In addition, figure 18 of this thesis demonstrates the influence of vessel size on our DCS measurements. However, clinically, we measure a wide array of vessel sizes; therefore, I would assume that the influence of vessel size on the DCS blood flow index may average out.

5.2.4 Conclusions

In summary, we use a novel, non-invasive optical technique known as diffuse correlation spectroscopy to characterize the cerebral hemodynamic response to intrathecal nicardipine treatment in patients with subarachnoid hemorrhage and cerebral vasospasm. We observed two distinct classes of microvascular cerebral blood flow response: 1) a steady increase, and 2) minimal-to-no change. Further, we found that 83% of patients who failed to respond

to nicardipine developed DCI, while 0% of the patients who showed a steady increase in cerebral blood flow developed DCI. These results suggest that monitoring microvascular perfusion is needed to ensure that intrathecal nicardipine is inducing its desired vasodilatory effects and that DCS is capable of performing these assessments. In the future, DCS may be a valuable biomarker alongside TCD to better inform clinical decisions, diminish the development of delayed cerebral ischemia, and improve functional outcomes following subarachnoid hemorrhage.

5.3 DCS-Measured Cerebral Blood Flow Changes in IT Nicardipine Over Multiple Days

Emory University Hospital (EUH) administers IT nicardipine multiple times a day, typically every 6-8 hours, for up to two weeks. Earlier, our first publication examined the DCS-measured cerebral blood flow changes in response to the first dose of IT nicardipine. Herein, we utilize DCS to characterize the microvascular cerebral blood flow response to IT nicardipine in a cohort of medium-high grade non-traumatic SAH patients on days 1, 2, 3, and 7 of treatment. We hypothesized that (1) the first dose of IT nicardipine will continuously increase microvascular cerebral blood flow from pre-administration levels and that these changes will be detectable by DCS and (2) the blood flow response to IT nicardipine will reach a steady state by day 3 of treatment.

5.3.1 Methods

Medium-high grade non-traumatic subarachnoid hemorrhage (SAH) patients at the Neurointensive Care Unit at Emory University Hospital were enrolled in this study. Written informed consent was obtained from all patients or their surrogates, and the study was approved by the Emory University Institutional Review Board. Nicardipine is

routinely administered intrathecally through an external ventricular drain upon detection of cerebral vasospasm. To assess the effects of IT nicardipine on cerebral blood flow, longitudinal 20Hz monitoring with DCS was performed before, during, and for up to 2h after IT nicardipine administration on days 1, 2, 3, and 7 of treatment. During data analysis, data were downsampled to 0.3 Hz. For the first day of nicardipine treatment, we captured the first dose of IT nicardipine. For the remaining days, we captured at least one dose during the day depending on the DCS instrument, clinical team availability, and the IT nicardipine administration schedule. For some patients, by day 7, IT nicardipine was no longer administered.

Patients received 4-5 mg of nicardipine mixed with 2 mL of preservative free saline intrathecally (IT) through an existing EVD. After administration, the EVD was clamped for up to 30 minutes to promote the uptake of nicardipine by the local tissue microenvironment. Treatment dose, frequency, and length were determined by the attending physician and were not influenced by this study.

Patient outcome was defined as the presence of DCI on the latest imaging available within 6 weeks from admission, per consensus criteria[229]. All available imaging studies (CT, MRI) were reviewed by at least two board-certified neurocritical care attending physicians, and a consensus decision was achieved regarding the presence of DCI.

DCS measurements were made with a custom built DCS instrument, comprised of an 852-nm long coherence length laser, a photon counting avalanche photodiode, and a software correlator. The patient interface consisted of a flexible sensor with source-detector separations of 1 and 2.5 cm, as detailed in [182]. This sensor was secured with a head strap on the forehead of the hemisphere with the vasospasm. Measured intensity autocorrelation

functions ($g_2(\tau)$), from our DCS measurements were each fit for a blood flow index, (BFI(t)), using the semi-infinite solution to the correlation diffusion equation[47]. Fits were constrained to $g_2(\tau) > 1.2$ to increase sensitivity to the brain[134]. To calculate relative change in cerebral blood flow (rCBF(t)) due to nicardipine administration, the BFI time series was normalized to the mean BFI in the 5 minutes immediately prior to nicardipine. Further, to investigate the relationship between micro and macrovascular blood flow in these patients, baseline BFI was compared to mean cerebral blood flow velocities measured by TCD on the same day as the DCS assessment.

In our first publication, we looked at the trends in data from the first dose of IT nicardipine and observed: 1) that changes in blood flow from IT nicardipine were detectable by DCS and 2) a statistically significant correlation between TCD-measured blood flow velocity in the MCA and DCS-measured blood flow. The next step of this study was to expand our data analysis across multiple days (days 2,3, and 7) to see if these trends remained constant or deviated.

5.3.2 Results

To date, between April 2019 and February 2022, we have recruited 22 patients. On average, cerebral blood flow increased significantly with time after IT nicardipine administration on days 1 and 2 ($p<0.001$,Figure 26), though the response was fairly heterogenous across subject. By the third and seventh day of treatment, the blood flow response was significantly reduced, suggesting that the drug had reached a steady state concentration in the brain (Figure 26).

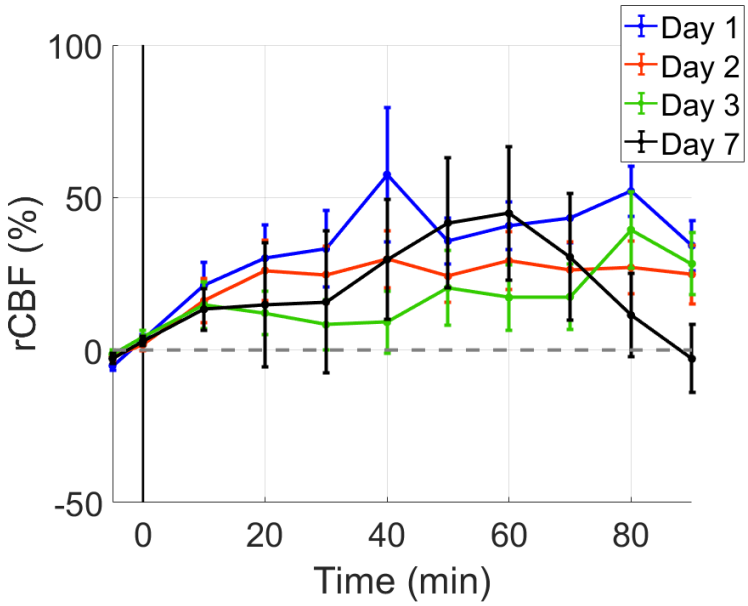

Figure 26: Mean ± standard error in relative changes of cerebral blood flow (rCBF, %) as a function of time post-IT nicardipine administration (given at t=0, denoted by the vertical black line). rCBF is shown for four days of the treatment. n=22 for Day 1, n=19 for Day 2, n=17 for Day 3, and n=7 for Day 7.

The graph above depicts the overall changes in blood flow regardless of outcome. The graphs below dichotomize each of the day's responses depending on their outcome, where outcome is classified if a patient is diagnosed with a DCI (Figure 27).

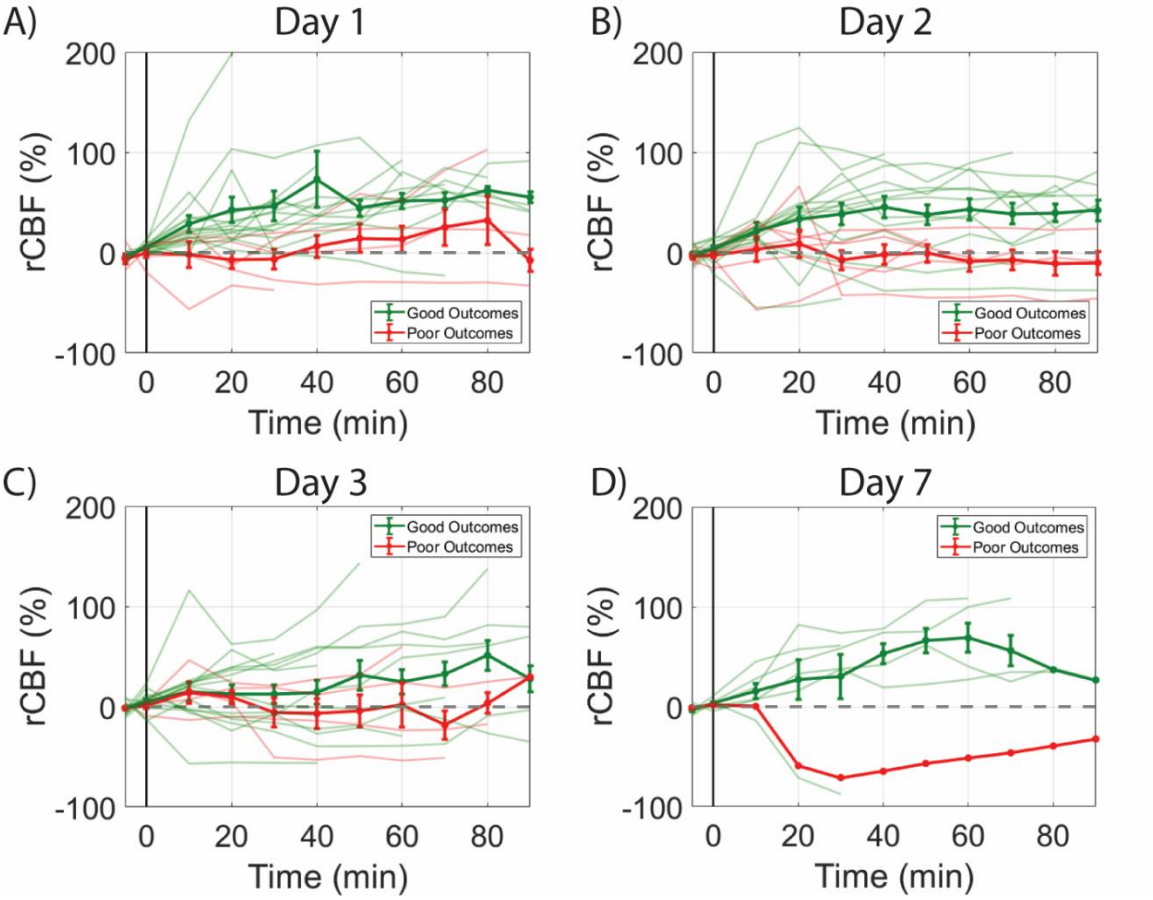

Figure 27: Mean ± standard error as a function of time for days 1 (a), 2 (b), 3 (c), and 7 (d) of nicardipine. Here, thin lines denote individual patient responses, while thick lines denote the model best fit for each response class identified by patient outcome. Green-colored lines represent the patients with no DCI, while the red-colored lines represent the patients who were diagnosed with DCI.

For these patients, we also noticed that the baseline blood flow index measured by DCS was significantly correlated with mean blood flow velocity in the middle cerebral artery (p=0.002, Figure 28). Similar correlation was not seen, although trending towards significance, with the mean blood flow velocity in the anterior cerebral artery (p=0.07, Figure 28). Similar results were also seen with our correlations from our first dose of nicardipine (Figure 25). Note, there was one patient where we were able to capture a day 4 DCS measurement, so their data was included in the figure below.

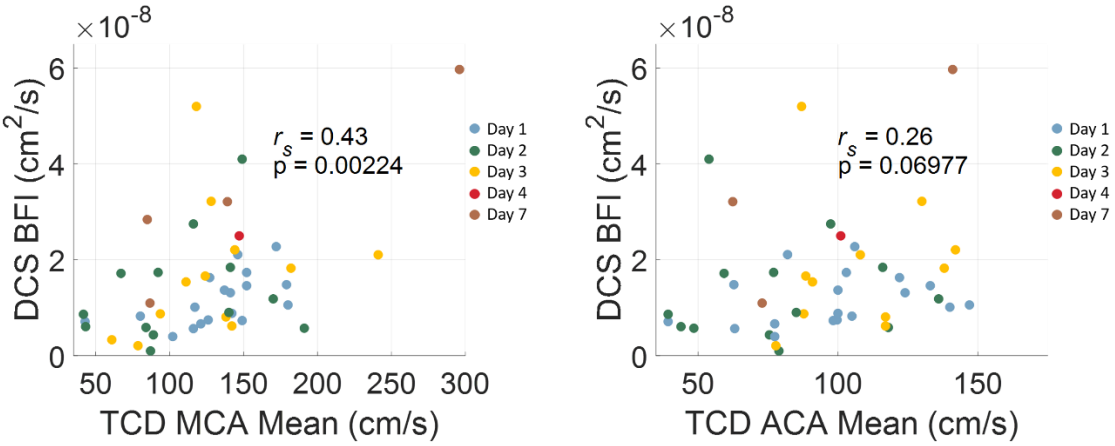

Figure 28: Relationship between DCS-measured BFI and TCD-measured mean blood flow velocity in the MCA (cm/s, a) and the ACA (b)

5.3.3 Conclusion

Our results suggest that IT nicardipine achieves the desired effect of microvascular vasodilation in the majority of patients after the first dose of treatment. Interestingly, those patients whose microvascular cerebral blood flow did not respond were the ones who went on to develop worse outcome (secondary stroke). Furthermore, after day 3, the patient's change in blood flow in response to nicardipine seems to reach a steady state. This finding suggests that for the DCI group, IT nicardipine does not induce any change in their cerebral blood flow for these patients over multiple days. This finding suggests that if this response is measured early on, then clinicians could change the course of care for these patients in an effort to avoid DCI. If these trends persist with a larger n, this work demonstrates that DCS may be a powerful tool to monitor the therapeutic efficacy of nicardipine treatment and to better guide clinical decisions targeted at reducing the incidence of secondary stroke.

5.4 Diffuse Optical Spectroscopies for Daily Trends from IT Nicardipine

5.4.1 Introduction

In previous sections of this chapter, we utilized DCS to measure blood flow changes from IT nicardipine. However, in the Buckley lab, we also have another optical modality, frequency-domain NIRS (FDNIRS)[167], that measures the concentration of oxygenated (HbO) and deoxygenated (HbR) hemoglobin, cerebral blood volume (CBV), and hemoglobin blood oxygenation (SO_2). In FDNIRS, a modulated (110 MHz) continuous light source at multiple (eight wavelengths for the instrument in the Buckley Lab) wavelengths illuminates the tissue. The detectors measure the outputted light that has been attenuated and phase shifted.

Simply, in FDNIRS, we solve the frequency domain solution of the photon diffusion equation (Equation 15) for a semi-infinite geometry to obtain the wavelength-dependent optical properties of the sampled tissue- absorption, μ_a, and reduced scattering, μ_s', coefficients[230]. For our experimental setup, we utilize 8 wavelengths and have four detectors at source-detector separations of 2, 2.5, 3, and 3.5 cm. The data analysis for FDNIRS is described in detail in[47,75]. With FDNIRS, we measure the oxy and deoxy-hemoglobin concentrations of the sampled tissue (HbO and HbR, μM). HbO and HbR are used to calculate: total hemoglobin, hemoglobin blood oxygenation, cerebral blood volume, and oxygen extraction fraction. Total hemoglobin (HbT) is calculated from the summation of HbO and HbR. Next, hemoglobin blood oxygenation is $SO_2 = HbO/HbT \times 100\%$. Cerebral blood volume (CBV) is calculated as $CBV = MW \times HbT/(D_{bt} \times Hgb)$, where MW is the molecular weight of hemoglobin (64500 g/mol), D_{bt} is the brain tissue density (assumed to be 1.05 g/mL), and Hgb (g/dL) is the blood hemoglobin

content determined from the most recent blood sample from a complete blood count. Finally, oxygen extraction fraction (OEF) is calculated as $OEF = (SaO_2 - SO_2)/(\gamma SaO_2)$, where SaO_2 is arterial oxygen saturation, which can be measured from a pulse oximeter and γ is the fraction of blood volume within the probed venous compartment of the tissue (assumed to be 1 for all subjects for simplicity)[58,231].

In addition, we combine the outputs of OEF from FDNIRS and CBF from DCS to measure an index of cerebral metabolic rate of oxygenation ($CMRO_2$). $CMRO_2$ is calculated as $CMRO_2 = \kappa \times Hgb \times BFI \times (SaO_2 - SO_2)$, where κ is the amount of oxygen that each gram of hemoglobin can carry ($\kappa = 1.34$).

Herein, we utilized FDNIRS and DCS to measure our subarachnoid hemorrhage patient cohort for each dose before IT nicardipine was administered. We were interested in exploring trends in oxygenated hemoglobin (HbO), deoxygenated hemoglobin (HbR), total hemoglobin (HbT), hemoglobin blood oxygenation (SO_2), oxygen extraction fraction (OEF), and cerebral metabolic rate of oxygenation ($CMRO_2$) across all patients and see if there were any differences between the patients with DCI and no DCI.

5.4.2 Methods

Between January 2021 and February 2022, we measured 9 patients with FDNIRS and DCS on days 1,2,3, and 7 prior to the administration of IT nicardipine. To make these measurements, a member from the SAH clinical team gently placed the FDNIRS and DCS sensor over both the left and right hemisphere for 10s and repeated this measurement 3x/hemisphere. We averaged each repetition to calculate a mean hemispheric estimate of each measured parameter.

For our FDNIRS measurements, raw data were discarded if the standard deviation of the phase measurements exceeded two degrees or if the AC amplitude ratio of standard deviation to mean was > 0.05. Next, at each wavelength, the slopes of ln ($AC \times r^2$) and phase as functions of source-detector separation, r, were used to estimate μ_s' and μ_a. Data at a given wavelength were discarded if R^2<0.95. The entire dataset was discarded if <5 wavelengths total passed this linear fit criterion.

5.4.3 Results/Discussion

In the cohort of 9 patients, we gathered FDNIRS data. 8/9 patients did not go on to develop a DCI, while 1/9 patients developed a DCI. Due to instrument availability, there were times when we were not able to measure FDNIRS prior to the start of IT nicardipine. The figure below shows the absolute average values of HbO, HbR, HbT, SO_2, OEF, μ_a, and μ_s', where the latter two contain important optical information, in our SAH cohort (Figure 29). Outcomes are dichotomized by the location of the vasospasm and if these patients were diagnosed with DCI or not.

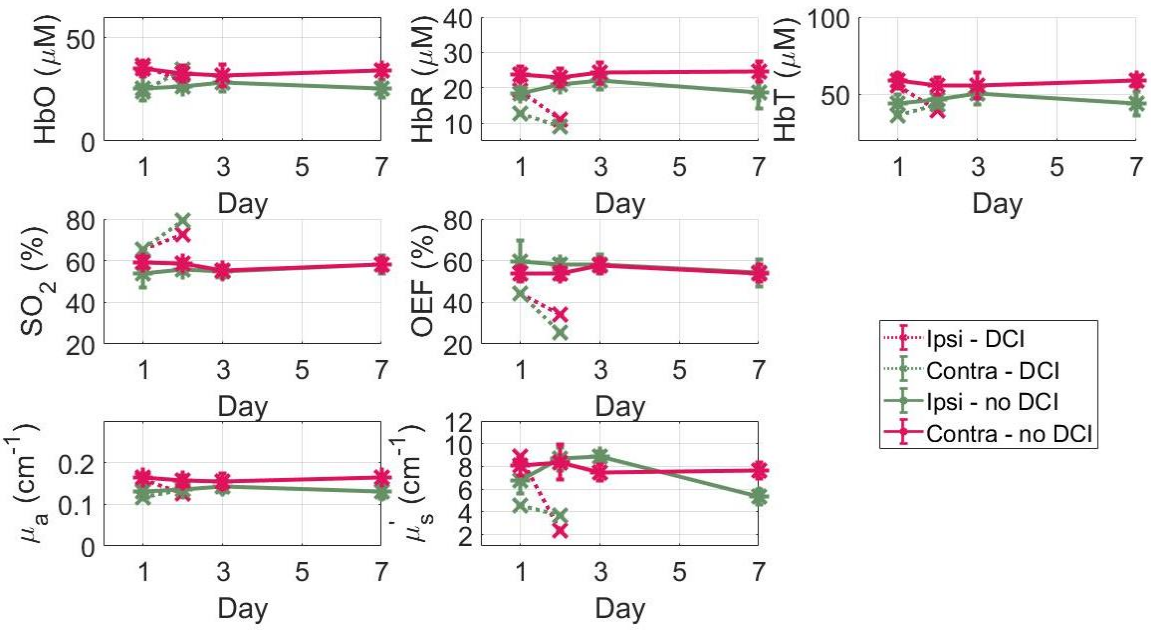

Figure 29: Overview of absolute mean and standard error values for HbO, HbR, HbT, SO_2, OEF, absorption coefficient, and reduced scattering coefficient across days 1,2,3, and 7 for n=9 patients. Results are dichotomized by outcome (DCI – dashed lines or no DCI – solid lines) and the location of the vasospasm (ipsilateral – red or contralateral – green). All of these values were acquired solely from the FDNIRS device.

In this small population, HbR is statistically significant between DCI and no DCI patients. This could suggest that from our short measurements HbR could also be another biomarker for which patients go on to develop a secondary stroke.

We also investigated if there were any hemispherical differences due to the vasospasm location dichotomized by outcome (Figure 30).

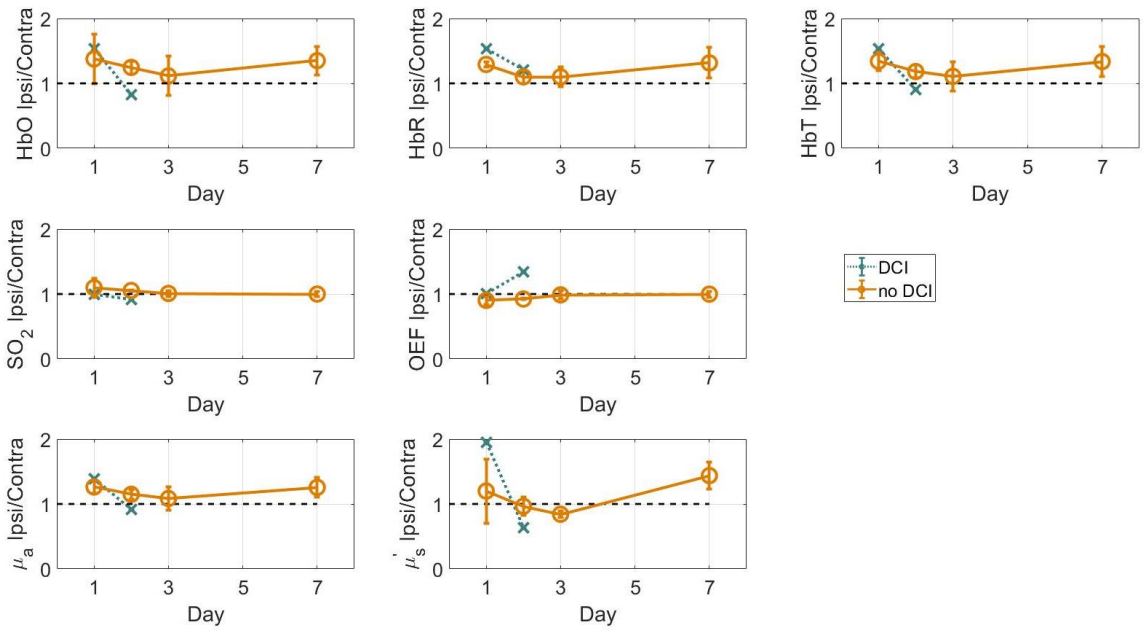

Figure 30: Mean and standard error values of the ratio of ipsilateral divided by the contralateral side for HbO, HbR, HbT, SO_2, OEF, absorption coefficient, and reduced scattering coefficient, where ipsilateral refers to the hemisphere with the vasospasm. Here, gold solid lines denote patients who did not go on to develop a DCI (n=8), whereas teal dashed lines represent patients who went on to develop a DCI (n=1).

Later on, for the 3 most recent patients, we were able to take DCS measurements along with FDNIRS measurements, which allows us to calculate the cerebral metabolic rate of oxygenation, $CMRO_2$, (Figure 31).

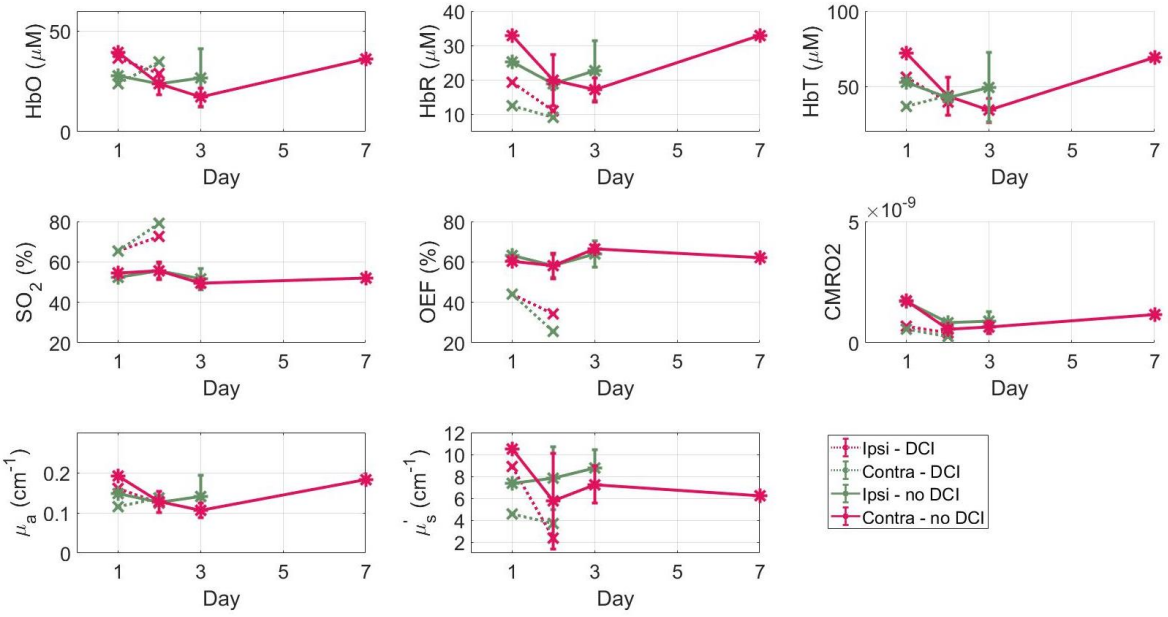

Figure 31: Overview of absolute mean and standard error values for HbO, HbR, HbT, SO_2, OEF, $CMRO_2$, absorption coefficient, and reduced scattering coefficient across days 1,2,3, and 7 for n=3 patients. Results are dichotomized by outcome (DCI – dashed lines or no DCI – solid lines) and the location of the vasospasm (ipsilateral – red or contralateral – green).

Similarly, we also investigated if there were any hemispherical differences due to the vasospasm location dichotomized by outcome (Figure 32).

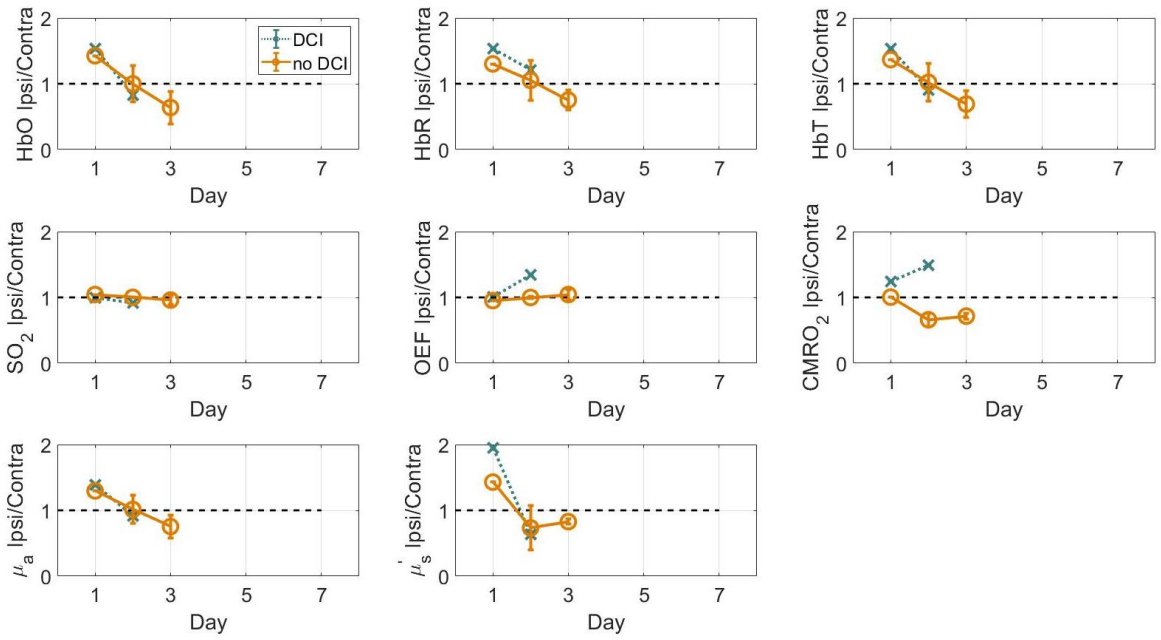

Figure 32: Mean and standard error values of the ratio of ipsilateral divided by the contralateral side for HbO, HbR, HbT, SO_2, OEF, $CMRO_2$, absorption coefficient, and reduced scattering coefficient, where ipsilateral refers to the hemisphere with the vasospasm. Here, gold solid lines denote patients who did not go on to develop a DCI (n=2), whereas teal dashed lines represent patients who went on to develop a DCI (n=1).

While this current cohort has a small sample size, since we started measuring patients recently as of January 2021, there are some promising trends that could emerge if we increase our sample size. In fact, these FDNIRS/DCS measurements are less time-intensive (~10 min) in comparison to the continuous DCS measurements that I discussed about in the previous section (~90 min). A potential future direction would be to make these FDNIRS/DCS measurements as soon as a SAH patient is admitted (day 0 of SAH) to explore if diffuse optics can be utilized as a prognostic tool for which SAH patients who would not only develop vasospasm but also require IT nicardipine, instead of only measuring SAH patients who are severe enough to require IT nicardipine.

Chapter 6: Conclusion

6.1 Summary and Key Findings

Diffuse correlation spectroscopy is a novel optical technique that was established in the late 1990s. Since then, a lot of publications from the community have focused on furthering this technology from hardware and software upgrades to various validation studies against other imaging modalities in preclinical and clinical cohorts. Within the DCS community, it is well-known that with DCS we measure an index of microvascular blood flow. However, it wasn't until 2016, when Boas et al. demonstrated that the origins of the DCS signal potentially stem from the shear-induced diffusion of red blood cells, which they demonstrated with Monte Carlo simulations. My work with the microfluidics platform advanced this previous work by making *in vitro* measurements for the first time. This microfluidic phantom platform is a huge advancement for the DCS community, as typical *in vitro* platforms within the DCS community consist of a large liquid vat filled with intralipid and India Ink or one large (~1-3 mm) embedded tube. However, the microfluidic platform developed in this dissertation is novel because it consists of 100s of micron-sized tubes ranging from 10 – 100 μm, which more accurately recapitulates the microvasculature. The added benefit of this novel *in vitro* platform is that I am able to manipulate a single red blood cell parameter, such as hematocrit, vessel size, flow rate, and blood type, and not experience any compensatory mechanism that would be otherwise seen *in vivo*. My first key finding with the microfluidics experiment was demonstrating the confounding influence of hematocrit on our DCS blood flow measurements when flowing healthy blood. I developed a hematocrit correction factor. Next, I examined the influence of vessel size on our DCS blood flow measurements. Finally, I demonstrated the influence of sickle cell

blood on the DCS blood flow index. All of this work conducted using the microfluidic platform theoretically advanced our knowledge of diffuse correlation spectroscopy.

The second half of my dissertation focused on the translational impact of diffuse correlation spectroscopy such that blood flow could potentially be used as biomarker in the brain's blood flow response to the intrathecal administration of the drug nicardipine in subarachnoid hemorrhage patients. This study was the first study to our knowledge that explores the impact of the intrathecal administration of nicardipine at the microvascular level. It was pivotal to see that patients who had an increase in their cerebral blood flow in response to IT nicardipine did not go on to develop a secondary stroke, whereas patients whose blood flow did not change or decreased went on to develop this secondary stroke known as delayed cerebral ischemia. If these trends prove to hold true with increased sample size, then DCS could function as a powerful biomarker to recognize patients who are poor responders to the drug, right from the first dose of IT nicardipine, and alert clinicians that alternative treatment strategies are merited.

6.2 Future Work

From the foundational work done in this dissertation, there are many opportunities for future work for both the theoretical (microfluidics) and the translational (SAH) components.

First, for the microfluidics project, the next steps would be to investigate how/if our DCS BFI changes when deoxygenating sickle cell blood. Additionally, it would be interesting to explore the impact of different ratios of HbA to HbSS to HbF on the DCS blood flow index.

Next, for the SAH project, I foresee many future projects that could stem from this rich dataset. Currently, we arrive at the hospital when the SAH patient is about to receive IT nicardipine. However, it would be interesting if we could do daily spot measurements once the SAH patient arrives at the hospital to see if FDNIRS/DCS could be used as a prognostic tool to predict which patients may not develop only vasospasms and will need IT nicardipine but also DCI. Next, I hope that we can utilize DCS when EUH starts their phase 2 clinical trial of randomizing IT nicardipine doses across SAH patients, allowing us to examine if the relative changes in the blood flow response to IT nicardipine as measured by DCS change in magnitude as a function of concentration among responders and non-responders.

Secondly, for the SAH project, we take up to 90 minutes of data at the bedside and simultaneously acquire measurements of arterial blood pressure. Therefore, we could utilize the acquired pulsatile cerebral blood flow and arterial blood pressure information to calculate critical closing pressure[232–235]. We also stochastically record the ICP numbers, so it would be informative to compare the measured ICP from the patient's external ventricular drain to our noninvasive measurements of critical closing pressure.

Lastly, it would be valuable to explore cerebral autoregulation using this SAH dataset. It is possible to calculate an index of cerebral autoregulation[49,236,237] by plotting our DCS blood flow index values against the measured arterial blood pressure. Here, we could see if cerebral autoregulation is potentially impaired in the SAH patients who go on to develop a DCI.

Overall, in medicine today, there's a shift towards more non-invasive medical devices in an effort to provide clinicians with more information for a patient-centered care.

Ultimately, I believe that the work presented here in this dissertation demonstrates the clinical utility and potential of DCS to one day be routinely utilized in the hospital as a prognostic tool. With this powerful goal in mind, the future is bright for diffuse correlation spectroscopy.

References

1. Prahl SA. Everything I think you should know about Inverse Adding-Doubling. 2011;(503):821-1344. Accessed October 21, 2021. http://omlc.org

2. Markus HS. Cerebral perfusion and stroke. *Journal of Neurology, Neurosurgery and Psychiatry*. 2004;75(3):353-361. doi:10.1136/jnnp.2003.025825

3. Durukan A, Tatlisumak T. Acute ischemic stroke: overview of major experimental rodent models, pathophysiology, and therapy of focal cerebral ischemia. *Pharmacol Biochem Behav*. 2007;87(1):179-197. doi:S0091-3057(07)00137-2 [pii]\r10.1016/j.pbb.2007.04.015 [doi]

4. Rickards CA. Cerebral blood-flow regulation during hemorrhage. *Compr Physiol*. 2015;5(4):1585-1621. doi:10.1002/cphy.c140058

5. Giza CC, Hovda DA. The new neurometabolic cascade of concussion. *Neurosurgery*. 2014;75(0 4):S24-S33. doi:10.1227/NEU.0000000000000505

6. Werner C, Engelhard K. Pathophysiology of traumatic brain injury. *British Journal of Anaesthesia*. 2007;99(1):4-9. doi:10.1093/bja/aem131

7. Wood T, Smit E, Maes E, et al. Monitoring of cerebral blood flow during hypoxia-ischemia and resuscitation in the neonatal rat using laser speckle imaging. *Physiological Reports*. 2016;4(7):1-14. doi:10.14814/phy2.12749

8. Liu W, Liu J, Lou X, et al. A longitudinal study of cerebral blood flow under hypoxia at high altitude using 3D pseudo-continuous arterial spin labeling. *Scientific Reports*. 2017;7. doi:10.1038/srep43246

9. Lucas SJE, Burgess KR, Thomas KN, et al. Alterations in cerebral blood flow and cerebrovascular reactivity during 14 days at 5050 m. *Journal of Physiology*. 2011;589(3):741-753. doi:10.1113/jphysiol.2010.192534

10. Muller M, Van Der Graaf Y, Visseren FL, Mali WPTM, Geerlings MI. Hypertension and longitudinal changes in cerebral blood flow: The SMART-MR study. *Annals of Neurology*. 2012;71(6):825-833. doi:10.1002/ana.23554

11. Strandgaard S, Paulson OB. Cerebral blood flow and its pathophysiology in hypertension. *Am J Hypertens*. 1989;2(6 Pt 1):486-492.

12. Fantini S, Sassaroli A, Tgavalekos KT, Kornbluth J. Cerebral blood flow and autoregulation: current measurement techniques and prospects for noninvasive optical methods. *Neurophotonics*. 2016;3(3):031411. doi:10.1117/1.nph.3.3.031411

13. Carden MA, Fay ME, Lu X, et al. Extracellular fluid tonicity impacts sickle red blood cell deformability and adhesion. *Blood*. 2017;130(24):2654-2663. doi:10.1182/blood-2017-04-780635

14. Toda N, Ayajiki K, Okamura T. Cerebral Blood Flow Regulation by Nitric Oxide: Recent Advances. *Pharmacological Reviews*. 2009;61(1):62-97. doi:10.1124/pr.108.000547

15. Lassen NA. Normal average value of cerebral blood flow in younger adults is 50 ml/100 g/min. *Journal of Cerebral Blood Flow and Metabolism*. 1985;5(3):347-349. doi:10.1038/jcbfm.1985.48

16. Dankbaar JW, de Rooij NK, Rijsdijk M, et al. Diagnostic threshold values of cerebral perfusion measured with computed tomography for delayed cerebral ischemia after aneurysmal subarachnoid hemorrhage. *Stroke*. 2010;41(9):1927-1932. doi:10.1161/STROKEAHA.109.574392

17. Zaaroor M, Mahamid E, Shik V, Soustiel JF. Course of cerebral blood flow and metabolism following severe brain injury. Correlation with neurological function and outcome. *The Indian Journal of Neurotrauma*. 2007;4(1):25-29. doi:10.1016/s0973-0508(07)80007-4

18. Kelly DF, Martin NA, Kordestani R, et al. Cerebral blood flow as a predictor of outcome following traumatic brain injury. *Journal of Neurosurgery*. 1997;86(4):633-641. doi:10.3171/jns.1997.86.4.0633

19. Golay X, Hendrikse J, Lim TC. Perfusion imaging using arterial spin labeling. *TopMagn ResonImaging*. 2004;15(0899-3459 (Print)):10-27. doi:10.1097/00002142-200402000-00003

20. Detre JA, Alsop DC. Perfusion magnetic resonance imaging with continuous arterial spin labeling: methods and clinical applications in the central nervous system. *Europ J Rad*. 1999;30:115-124.

21. Cherry SB. Fundamentals of positron emission tomography and applications in preclinical drug development. *Journal of Clinical Pharmacology*. 2001;41(5):482-491. doi:10.1177/00912700122010357

22. Hutton BF. The origins of SPECT and SPECT/CT. *European Journal of Nuclear Medicine and Molecular Imaging*. 2014;41(SUPPL. 1). doi:10.1007/s00259-013-2606-5

23. Purkayastha S, Sorond F. Transcranial Doppler ultrasound: technique and application. *Semin Neurol*. 2012;32(4):411-420. doi:10.1055/s-0032-1331812

24. Jahng GH, Li KL, Ostergaard L, Calamante F. Perfusion magnetic resonance imaging: A comprehensive update on principles and techniques. *Korean Journal of Radiology*. 2014;15(5):554-577. doi:10.3348/kjr.2014.15.5.554

25. Petcharunpaisan S. Arterial spin labeling in neuroimaging. *World Journal of Radiology*. 2010;2(10):384. doi:10.4329/wjr.v2.i10.384

26. Ferré JC, Bannier E, Raoult H, Mineur G, Carsin-Nicol B, Gauvrit JY. Arterial spin labeling (ASL) perfusion: Techniques and clinical use. *Diagnostic and Interventional Imaging*. 2013;94(12):1211-1223. doi:10.1016/j.diii.2013.06.010

27. Alsop DC, Detre JA, Golay X, et al. Recommended Implementation of Arterial Spin Labeled Perfusion MRI for Clinical Applications: A consensus of the ISMRM Perfusion Study Group and the European Consortium for ASL in Dementia.

28. Wolf RL, Detre JA. Clinical Neuroimaging Using Arterial Spin-Labeled Perfusion Magnetic Resonance Imaging. *Neurotherapeutics*. 2007;4(3):346-359. doi:10.1016/j.nurt.2007.04.005

29. Shen Q, Duong TQ. Magnetic Resonance Imaging of Cerebral Blood Flow in Animal Stroke Models. *Brain Circ*. 2016;2(1):20-27. doi:10.4103/2394-8108.178544

30. Williams DS, Detre JA, Leigh JS, Koretsky AP. Magnetic resonance imaging of perfusion using spin inversion of arterial water. *Proceedings of the National Academy of Sciences*. 1992;89(1):212-216. doi:10.1073/pnas.89.1.212

31. Essig M, Shiroishi MS, Nguyen TB, et al. Perfusion MRI: The five most frequently asked technical questions. *American Journal of Roentgenology*. 2013;200(1):24-34. doi:10.2214/AJR.12.9543

32. Sakoh M, Røhl L, Gyldensted C, Gjedde A, Østergaard L. Cerebral blood flow and blood volume measured by magnetic resonance imaging bolus tracking after acute stroke in pigs: Comparison with [15O]H2O positron emission tomography. *Stroke*. 2000;31(8):1958-1964. doi:10.1161/01.STR.31.8.1958

33. Zakariaee SS, Oghabian MA, Firouznia K, Sharifi G, Arbabi F, Samiei F. Assessment of the Agreement between Cerebral Hemodynamic Indices Quantified Using Dynamic Susceptibility Contrast and Dynamic Contrast-enhanced Perfusion Magnetic Resonance Imagings. *Journal of Clinical Imaging Science*. 2018;8(1). doi:10.4103/jcis.JCIS_74_17

34. Ayaz Khan M, Liu J, Tarumi T, et al. Measurement of cerebral blood flow using phase contrast magnetic resonance imaging and duplex ultrasonography. doi:10.1177/0271678X16631149

35. Phase-Contrast MRI: Physics, Tech-niques, and Clinical Applications. doi:10.1148/rg.2020190039

36. Liu P, Lu H, Filbey FM, Pinkham AE, Mcadams CJ. Automatic and Reproducible Positioning of Phase-Contrast MRI for the Quantification of Global Cerebral Blood Flow. *PLoS ONE*. 2014;9(5):95721. doi:10.1371/journal.pone.0095721

37. Proisy M, Bruneau B, Rozel C, et al. Arterial spin labeling in clinical pediatric imaging. *Diagnostic and Interventional Imaging*. 2016;97(2):151-158. doi:10.1016/J.DIII.2015.09.001

38. Herscovitch P, Markham J, Raichle ME. Brainb Blood Flow Measured with Intravenous H2 15O. *Investigative Nuclear Medicine*. 1983;24(9):782-789.

39. Raichle ME, Martin WRW, Herscovltch P, Mintun MA, Markham J. Raichle1983_BrainBlood..

40. Yonas H, Pindazola RR, Johnson DW. Xenon/computed tomography cerebral blood flow and its use in clinical management. *Neurosurgery Clinics of North America*. 1996;7(4):605-616. doi:10.1016/s1042-3680(18)30349-8

41. Drayer BP, Wolfson SK, Reinmuth OM, Dujovny M, Boehnke M, Cook EE. Xenon enhanced ct for analysis of cerebral integrity, perfusion, and blood flow. *Stroke*. 1978;9(2):123-130. doi:10.1161/01.STR.9.2.123

42. Hoedt-Rasmussen K, Sveinsdottir E, Lassen NA. Regional cerebral blood flow in man determined by intra-arterial injection of radioactive inert gas. *Circ Res*. 1966;18(3):237-247. doi:10.1161/01.RES.18.3.237

43. Webster MW, Steed DL, Yonas H, Latchaw RE, Wolfson SK, Gur D. Cerebral blood flow measured by xenon-enhanced computed tomography as a guide to management of patients with cerebrovascular disease. *Journal of Vascular Surgery*. 1986;3(2):298-304. doi:10.1067/mva.1986.avs0030298

44. Bathala L, Mehndiratta M, Sharma V. Transcranial doppler: Technique and common findings (Part 1). *Ann Indian Acad Neurol*. 2013;16(2):174-179. doi:10.4103/0972-2327.112460

45. Boas DA, Campbell LE, Yodh AG. Scattering and imaging with diffusing temporal field correlations. *Physical Review Letters*. 1995;75(9):1855-1858. doi:10.1103/PhysRevLett.75.1855

46. Boas DA, Yodh AG. Spatially varying dynamical properties of turbid media probed with diffusing temporal light correlation. *Journal of Optical Society of America*. 1997;14. Accessed May 21, 2018. https://www.physics.upenn.edu/yodhlab/papers/1997/JOSAA_vol14p192_1997.pdf

47. Durduran T, Choe R, Baker WB, Yodh AG. Diffuse optics for tissue monitoring and tomography. *Reports on Progress in Physics*. 2010;73(7):76701-76743. doi:10.1088/0034-4885/73/7/076701

48. Durduran T, Zhou C, Edlow BL, et al. Transcranial optical monitoring of cerebrovascular hemodynamics in acute stroke patients. *Optics Express*. 2009;17(5):3884. doi:10.1364/OE.17.003884

49. Selb J, Wu KC, Sutin J, et al. Prolonged monitoring of cerebral blood flow and autoregulation in subarachnoid hemorrhage and stroke patients with diffuse correlation spectroscopy. *Neurophotonics*. 2018;5(4). doi:10.1117/1.NPh.5.4.045005

50. Mullen MT, Parthasarathy AB, Zandieh A, et al. Cerebral Blood Flow Response During Bolus Normal Saline Infusion After Ischemic Stroke. *Journal of Stroke and Cerebrovascular Diseases*. 2019;28(11):104294. doi:10.1016/j.jstrokecerebrovasdis.2019.07.010

51. Favilla CG, Mesquita RC, Mullen M, et al. Optical bedside monitoring of cerebral blood flow in acute ischemic stroke patients during head-of-bed manipulation. *Stroke*. 2014;45(5):1269-1274. doi:10.1161/STROKEAHA.113.004116

52. Baker WB, Balu R, He L, et al. Continuous non-invasive optical monitoring of cerebral blood flow and oxidative metabolism after acute brain injury. *Journal of Cerebral Blood Flow and Metabolism*. Published online 2019. doi:10.1177/0271678X19846657

53. Busch DR, Balu R, Baker WB, et al. Detection of Brain Hypoxia Based on Noninvasive Optical Monitoring of Cerebral Blood Flow with Diffuse Correlation Spectroscopy. *Neurocritical Care*. 2019;30(1):72-80. doi:10.1007/s12028-018-0573-1

54. Kim MN, Edlow BL, Durduran T, et al. Continuous optical monitoring of cerebral hemodynamics during head-of-bed manipulation in brain-injured adults. *Neurocritical Care*. 2013;20(3):443-453. doi:10.1007/s12028-013-9849-7

55. Kim MN, Durduran T, Frangos S, et al. Noninvasive measurement of cerebral blood flow and blood oxygenation using near-infrared and diffuse correlation spectroscopies in critically brain-injured adults. *Neurocritical Care*. 2010;12(2):173-180. doi:10.1007/s12028-009-9305-x

56. Lynch JM, Ko T, Busch DR, et al. Preoperative cerebral hemodynamics from birth to surgery in neonates with critical congenital heart disease. *Journal of Thoracic and Cardiovascular Surgery*. 2018;156(4):1657-1664. doi:10.1016/j.jtcvs.2018.04.098

57. Lynch JM, Buckley EM, Schwab PJ, et al. Time to surgery and preoperative cerebral hemodynamics predict postoperative white matter injury in neonates with hypoplastic left heart syndrome. *Journal of Thoracic and Cardiovascular Surgery*. 2014;148(5):2181-2188. doi:10.1016/j.jtcvs.2014.05.081

58. Jain V, Buckley EM, Licht DJ, et al. Cerebral oxygen metabolism in neonates with congenital heart disease quantified by MRI and optics. *Journal of Cerebral Blood Flow and Metabolism*. 2014;34(3):380-388. doi:10.1038/jcbfm.2013.214

59. Durduran T, Zhou C, Buckley EM, et al. Optical measurement of cerebral hemodynamics and oxygen metabolism in neonates with congenital heart defects. *Journal of Biomedical Optics*. 2010;15(3):037004. doi:10.1117/1.3425884

60. Buckley EM, Naim MY, Lynch JM, et al. Sodium bicarbonate causes dose-dependent increases in cerebral blood flow in infants and children with single-ventricle physiology. *Pediatric Research*. 2013;73(5):668-673. doi:10.1038/pr.2013.25

61. Buckley EM, Lynch JM, Goff DA, et al. Early postoperative changes in cerebral oxygen metabolism following neonatal cardiac surgery: Effects of surgical duration. *Journal of Thoracic and Cardiovascular Surgery*. 2013;145(1). doi:10.1016/j.jtcvs.2012.09.057

62. Dehaes M, Cheng HH, Buckley EM, et al. Perioperative cerebral hemodynamics and oxygen metabolism in neonates with single-ventricle physiology. *Biomedical Optics Express*. 2015;6(12):4749. doi:10.1364/boe.6.004749

63. The Radiative Transfer Equation With Scattering.

64. Wu MM, Chan S tak, Mazumder D, et al. Improved accuracy of cerebral blood flow quantification in the presence of systemic physiology cross-talk using. *Neurophotonics*. 2021;8(1):1-24. doi:10.1117/1.NPh.8.1.015001

65. Boas DA, Yodh AG. Spatially varying dynamical properties of turbid media probed with diffusing temporal light correlation. *Journal of Optical Society of America*. Published online 1997.

66. Boas DA, Sakadžic S, Selb J, Farzam P, Franceschini MA, Carp SA. Establishing the diffuse correlation spectroscopy signal relationship with blood flow. *Neurophotonics*. 2016;3(3):031412. doi:10.1117/1.NPh.3.3.031412

67. Buckley EM, Hance D, Pawlowski T, et al. Validation of diffuse correlation spectroscopic measurement of cerebral blood flow using phase-encoded velocity mapping magnetic resonance imaging. *Journal of Biomedical Optics*. 2012;17(3):037007. doi:10.1117/1.jbo.17.3.037007

68. Proctor AR, Ramirez GA, Han S, Liu Z, Bubel TM, Choe R. Validation of diffuse correlation spectroscopy sensitivity to nicotinamide-induced blood flow elevation in the murine hindlimb using the fluorescent microsphere technique. *Journal of Biomedical Optics*. 2018;23(03):1. doi:10.1117/1.JBO.23.3.035006

69. Zhou C, Eucker SA, Durduran T, et al. Diffuse optical monitoring of hemodynamic changes in piglet brain with closed head injury. *J Biomed Opt*. 2009;14(3):034015. doi:10.1117/1.3146814

70. Lemieux PA, Durian DJ. Investigating non-Gaussian scattering processes by using nth -order intensity correlation functions. *Journal of the Optical Society of America A*. 1999;16(7):1651. doi:10.1364/JOSAA.16.001651

71. Yu G, Durduran T, Zhou C, Cheng R, Yodh AG. Near-Infrared Diffuse Correlation Spectroscopy for Assessment of Tissue Blood Flow. *Handbook of Biomedical Optics*. Published online 2011:195-216. doi:doi:10.1201/b10951-13

72. Ackerson BJ, Dougherty RL, Reguigui NM, Nobbmann U. Correlation Transfer: Application of Radiative Transfer Solution Methods to Photon Correlation Problems. *JOURNAL OF THERMOPHYSICS AND HEAT TRANSFER*. 6(4). doi:10.2514/3.11537

73. Boas D. *Diffuse Photon Probes of Structural and Dynamical Properties of Turbid Media*. 1996.

74. R. L. DOUGHERTY, B. J. ACKERSON,N. M. REGUIGUI, F. DORRI-NOWKOORANI. Correlation Transfer : Development. *Science (1979)*. Published online 1994.

75. Baker WB. Optical Cerebral Blood Flow Monitoring of Mice To Men. Published online 2015:273.

76. Mesquita RC, Durduran T, Yu G, et al. Direct measurement of tissue blood flow and metabolism with diffuse optics. *Philosophical Transactions of the Royal Society A: Mathematical, Physical and Engineering Sciences*. 2011;369(1955):4390-4406. doi:10.1098/rsta.2011.0232

77. Einstein A. *ON THE ELECTRODYNAMICS OF MOVING BODIES*.; 1905.

78. Boas DA, Sakadžić S, Selb J, Farzam P, Franceschini MA, Carp SA. Establishing the diffuse correlation spectroscopy signal relationship with blood flow. *Neurophotonics*. 2016;3(3):031412. doi:10.1117/1.NPh.3.3.031412

79. Eckstein EC, Bailey DG, Shapiro AH. Self-diffusion of particles in shear flow of a suspension. *Journal of Fluid Mechanics*. 1977;79(1):191-208. doi:10.1017/S0022112077000111

80. Leighton D, Acrivos A. The Shear-Induced Migration of Particles in Concentrated Suspensions. *Journal of Fluid Mechanics*. 1987;181:415-439. doi:10.1017/S0022112087002155

81. Leighton D, Acrivos A. Measurement of shear induced self diffusion in concentrated suspensions of spheres. *Journal of Fluid Mechanics*. 1987;177:109-131. doi:10.1017/S0022112087000880

82. Goldsmith HL, Marlow JC. Flow Behavior of Erythrocytes. *Journal of Colloid and Interface Science*. 1979;71(2):383-407.

83. Haskell RC, Svaasand LO, Tsay TT, Feng TC, Tromberg BJ, McAdams MS. Boundary conditions for the diffusion equation in radiative transfer. *Journal of the Optical Society of America A*. 1994;11(10):2727. doi:10.1364/JOSAA.11.002727

84. Irwin D, Dong L, Shang Y, et al. Influences of tissue absorption and scattering on diffuse correlation spectroscopy blood flow measurements. *Biomedical Optics Express*. 2011;2(7):1969. doi:10.1364/boe.2.001969

85. Durduran T, Yodh AG. Diffuse correlation spectroscopy for non-invasive, micro-vascular cerebral blood flow measurement. *Neuroimage*. 2014;85:51-63. doi:10.1016/j.neuroimage.2013.06.017

86. Gagnon L, Ele Desjardins M, Jehanne-Lacasse J, Bherer L, Lesage F. *Investigation of Diffuse Correlation Spectroscopy in Multi-Layered Media Including the Human Head*.; 2008. Accessed October 10, 2018. https://www.osapublishing.org/DirectPDFAccess/F1EFD1FB-09A2-F57C-F23528BE943E7F05_172103/oe-16-20-15514.pdf?da=1&id=172103&seq=0&mobile=no

87. Milej D, Abdalmalak A, Rajaram A, St Lawrence K. Direct Assessment of Extracerebral Signal Contamination on Optical Measurements of Cerebral Blood Flow, Oxygenation, and Metabolism. *Neurophotonics*. 2020;7(4):1-17. doi:10.1117/1.NPh.7.4.045002

88. Baker WB, Parthasarathy AB, Ko TS, et al. Pressure modulation algorithm to separate cerebral hemodynamic signals from extracerebral artifacts. Published online 2015. doi:10.1117/1.NPh.2.3.035004

89. Verdecchia K, Diop M, Lee A, et al. Assessment of a multi-layered diffuse correlation spectroscopy method for monitoring cerebral blood flow in adults. *BIOMEDICAL OPTICS EXPRESS*. 2016;27(3659):1951-1958. doi:10.1364/BOE.7.003659

90. Li J, Qiu L, Poon C sing, Sunar U. Analytical models for time-domain diffuse correlation spectroscopy for multi-layer and heterogeneous turbid media. *Biomedical Optics Express*. 2017;8(12):5518. doi:10.1364/BOE.8.005518

91. Li J, Dietsche G, Iftime D, et al. Noninvasive detection of functional brain activity with near-infrared diffusing-wave spectroscopy. *Journal of Biomedical Optics*. 2005;10(4). doi:10.1117/1.2007987

92. Sathialingam E, Williams EK, Lee SY, McCracken CE, Lam WA, Buckley EM. Hematocrit significantly confounds diffuse correlation spectroscopy measurements of blood flow. *Biomedical Optics Express*. 2020;11(8):4786. doi:10.1364/boe.397613

93. Zhao H, Sathialingam E, Buckley EM. Accuracy of Diffuse Correlation Spectroscopy measurements of brain blood flow when using a three-layer analytical model. *Biomed Opt Express*. 2021;2021(11):8-9.

94. Kim MN. *APPLICATIONS OF HYBRID DIFFUSE OPTICS FOR CLINICAL MANAGEMENT OF ADULTS AFTER BRAIN INJURY*. 2013.

95. Carp SA, Tamborini D, Mazumder D, et al. Diffuse correlation spectroscopy measurements of blood flow using 1064 nm light. *Journal of Biomedical Optics*. 2020;25(09):97003-97004. doi:10.1117/1.JBO.25.9.097003

96. Bellini T, Glaser MA, Clark NA, Degiorgio V. Effects of finite laser coherence in quasielastic multiple scattering. *Physical Review A*. 1991;44(8):5215-5223. doi:10.1103/PhysRevA.44.5215

97. Biswas A, Parthasarathy AB. Fast diffuse correlation spectroscopy with a low-cost, fiberless embedded diode laser. *Optics InfoBase Conference Papers*. 2020;Part F178-(11):6686-6700. doi:10.1364/boe.435136

98. Kiguchi M, Ichikawa N, Atsumori H, et al. Comparison of light intensity on the brain surface due to laser exposure during optical topography and solar irradiation. *Journal of Biomedical Optics*. 2007;12(6):062108. doi:10.1117/1.2804152

99. Code P. Consolidated editions Further information on IEC publications IEC TR 60825-14 Safety of laser products-Part 14: A user's guide including photocopying and microfilm, without permission in writing from the publisher. Published online 2004. Accessed April 30, 2022. www.iec.ch/searchpub

100. Laser Products-Conformance with IEC 60825-1 Ed. 3 and IEC 60601-2-22 Ed. 3.1 (Laser Notice No. 56) Guidance for Industry and Food and Drug Administration Staff Preface Public Comment. Published online 2019. Accessed April 30, 2022. https://www.regulations.gov

101. Zhou C. *In-Vivo Optical Imaging and Spectroscopy of Cerebral Hemodynamics*. 2007.

102. Wang D, Parthasarathy AB, Baker WB, et al. Fast blood flow monitoring in deep tissues with real-time software correlators. *Biomedical Optics Express*. 2016;7(3):776. doi:10.1364/BOE.7.000776

103. Sathialingam E, Lee SY, Sanders B, et al. Small separation diffuse correlation spectroscopy for measurement of cerebral blood flow in rodents. *Biomedical Optics Express*. 2018;9(11):5719-5734. doi:10.1364/BOE.9.005719

104. Fang Q, Boas DA. Monte Carlo simulation of photon migration in 3D turbid media accelerated by graphics processing units. *Opt Express*. 2009;17(22):20178-20190. doi:187243 [pii]

105. Wang L, Jacques SL, Zheng L. MCML- Monte Carlo Modeling of light transport in multi-layered tissues. *Computer Methods and Programs in Biomedicine*. Published online 1995.

106. Larsson B, Ullberg S. *Whole-Body Autoradiography*. Vol 29.; 1981.

107. Jay TM, Lucignani G, Crane AM, Jehle J, Sokoloff L. Measurement of local cerebral blood flow with [14C]iodoantipyrine in the mouse. *J Cereb Blood Flow Metab*. 1988;8(1):121-129. doi:10.1038/jcbfm.1988.16

108. Muir ER, Shen Q, Duong TQ. Cerebral blood flow MRI in mice using the cardiac-spin-labeling technique. *Magnetic Resonance in Medicine*. 2008;60(3):744-748. doi:10.1002/mrm.21721

109. Hedna VS, Ansari S, Shahjouei S, et al. Validity of Laser Doppler Flowmetry in Predicting Outcome in Murine Intraluminal Middle Cerebral Artery Occlusion Stroke. *Journal of Vascular and Interventional Neurology*. 2015;8(3):74-82.

110. Tajima Y, Takuwa H, Kawaguchi H, et al. Reproducibility of measuring cerebral blood flow by laser-Doppler flowmetry in mice. *Frontiers in Bioscience*. 2014;(11):1-27.

111. Piilgaard H, Lauritzen M. Persistent increase in oxygen consumption and impaired neurovascular coupling after spreading depression in rat neocortex. *Journal of Cerebral Blood Flow and Metabolism*. 2009;29(9):1517-1527. doi:10.1038/jcbfm.2009.73

112. Boas DA, Dunn AK. Laser speckle contrast imaging in biomedical optics. *Journal of Biomedical Optics*. 2010;15(1):011109. doi:10.1117/1.3285504

113. Dunn AK. Laser speckle contrast imaging of cerebral blood flow. *Annals of Biomedical Engineering*. 2012;40(2):367-377. doi:10.1007/s10439-011-0469-0

114. Stuart Foster F, Hossack J, Lee Adamson S. Micro-ultrasound for preclinical imaging. *Interface Focus*. 2011;1(4):576-601. doi:10.1098/rsfs.2011.0037

115. Buckley EM, Parthasarathy AB, Grant PE, Yodh AG, Franceschini MA. Diffuse correlation spectroscopy for measurement of cerebral blood flow: future prospects. *Neurophotonics*. 2014;1(1):011009. doi:10.1117/1.nph.1.1.011009

116. Culver JP, Durduran T, Cheung C, Furuya D, Greenberg JH, Yodh AG. Diffuse optical measurement of hemoglobin and cerebral blood flow in rat brain during hypercapnia, hypoxia and cardiac arrest. In: *Oxygen Transport to Tissue XXIII*. ; 2003:293-297.

117. Zhou C, Yu G, Furuya D, Greenberg JH, Yodh AG, Durduran T. Diffuse optical correlation tomography of cerebral blood flow during cortical spreading depression in rat brain. *Optics Express*. 2006;14(3):1125. doi:10.1364/OE.14.001125

118. Cheung C, Culver JP, Takahashi K, Greenberg JH, Yodh AG. In vivo cerebrovascular measurement combining diffuse near-infrared absorption and correlation spectroscopies. *Physics in Medicine and Biology*. 2001;46(8):2053-2065. doi:10.1088/0031-9155/46/8/302

119. Shang Y, Chen L, Toborek M, Yu G. Diffuse optical monitoring of repeated cerebral ischemia in mice. *Optics Express*. 2011;19(21):20301. doi:10.1364/OE.19.020301

120. Buckley EM, Patel SD, Miller BF, Franceschini MA, Vannucci SJ. In vivo Monitoring of Cerebral Hemodynamics in the Immature Rat: Effects of Hypoxia-Ischemia and Hypothermia. *Developmental Neuroscience*. 2015;37(4-5):407-416. doi:10.1159/000381704

121. Buckley EM, Miller BF, Golinski JM, et al. Decreased microvascular cerebral blood flow assessed by diffuse correlation spectroscopy after repetitive concussions in mice. *Journal of Cerebral Blood Flow & Metabolism*. 2015;35. doi:10.1038/jcbfm.2015.161

122. Carp SA, Dai GP, Boas DA, Franceschini MA, Kim YR. Validation of diffuse correlation spectroscopy measurements of rodent cerebral blood flow with simultaneous arterial spin labeling MRI; towards MRI-optical continuous cerebral metabolic monitoring. *Biomedical Optics Express*. 2010;1(2):553. doi:10.1364/BOE.1.000553

123. Buckley EM, Miller BF, Golinski JM, et al. Decreased microvascular cerebral blood flow assessed by diffuse correlation spectroscopy after repetitive concussions in mice. *Journal of Cerebral Blood Flow and Metabolism*. 2015;35(12):1995-2000. doi:10.1038/jcbfm.2015.161

124. Kaplan PD, Kao MH, Yodh AG, Pine DJ. Geometric constraints for the design of diffusing-wave spectroscopy experiments. *Applied Optics*. 1993;32(21):3828-3836. doi:10.1364/AO.32.003828

125. Favilla CG, Parthasarathy AB, Detre JA, et al. Non-invasive respiratory impedance enhances cerebral perfusion in healthy adults. *Frontiers in Neurology*. 2017;8(FEB):45. doi:10.3389/fneur.2017.00045

126. Durduran T, Yu G, Burnett MG, et al. Diffuse optical measurement of blood flow, blood oxygenation, and metabolism in a human brain during sensorimotor cortex activation. *Optics Letters*. 2004;29(15):1766. doi:10.1364/OL.29.001766

127. Yu G, Floyd TF, Durduran T, et al. Validation of diffuse correlation spectroscopy for muscle blood flow with concurrent arterial spin labeled perfusion MRI. *Optics Express*. 2007;15(3):1064. doi:10.1364/OE.15.001064

128. Diop M, Verdecchia K, Lee TY, St Lawrence K. Calibration of diffuse correlation spectroscopy with a time-resolved near-infrared technique to yield absolute

cerebral blood flow measurements. *Biomedical Optics Express*. 2012;3(6):1476. doi:10.1364/boe.3.001476

129. Buckley EM, Cook NM, Durduran T, et al. Cerebral hemodynamics in preterm infants during positional intervention measured with diffuse correlation spectroscopy and transcranial Doppler ultrasound. *Opt Express*. 2009;17(15):12571-12581. doi:10.1364/OE.17.012571

130. Zirak P, Delgado-Mederos R, Martí-Fàbregas J, Durduran T. Effects of acetazolamide on the micro- and macro-vascular cerebral hemodynamics: a diffuse optical and transcranial doppler ultrasound study. *Biomedical Optics Express*. 2010;1(5):1443. doi:10.1364/BOE.1.001443

131. Roche-Labarbe N, Carp SA, Surova A, et al. Noninvasive optical measures of CBV, StO2, CBF index, and rCMRO2 in human premature neonates' brains in the first six weeks of life. *Human Brain Mapping*. 2011;32(7):1179. doi:10.1002/hbm.21190

132. Yu G, Durduran T, Zhou C, et al. Noninvasive Monitoring of Murine Tumor Blood Flow During and After Photodynamic Therapy Provides Early Assessment of Therapeutic Efficacy. *Clinical Cancer Research*. 2005;11(9):3543-3552. doi:10.1158/1078-0432.ccr-04-2582

133. Hong G, Diao S, Chang J, et al. Through-skull fluorescence imaging of the brain in a new near-infrared window. *Nature Photonics*. 2014;8(9):723-730. doi:10.1038/nphoton.2014.166

134. Selb J, Boas DA, Chan ST, Evans KC, Buckley EM, Carp SA. Sensitivity of near-infrared spectroscopy and diffuse correlation spectroscopy to brain hemodynamics: simulations and experimental findings during hypercapnia. *Neurophotonics*. 2014;1(1):015005. doi:10.1117/1.NPh.1.1.015005

135. Cuccia DJ, Abookasis D, Frostig RD, Tromberg BJ. Chapter 12 Quantitative In Vivo Imaging of Tissue Absorption , Scattering , and Hemoglobin Concentration in Rat Cortex Using Spatially Modulated Structured Light. *In Vivo Optical Imaging of Brain Function*. Published online 2009:2-6. doi:10.1201/9781420076851.ch12

136. Kim SG. Quantification of Relative Cerebral Blood Flow Change by Flow-Sensitive Alternating Inversion Recovery (FAIR) Technique: Application to Functional Mapping. *Magnetic Resonance in Medicine*. Published online 1995.

137. Kim SG, Tsekos N V. Perfusion imaging by a flow-sensitive alternating inversion recovery (FAIR) technique: application to functional brain imaging. *Magnetic resonance in medicine : official journal of the Society of Magnetic Resonance in Medicine / Society of Magnetic Resonance in Medicine*. 1997;37(3):425-435.

138. Herscovitch P, Raichle ME. What Is the Correct Value for the Brain Blood Partition-Coefficient for Water. *Journal of Cerebral Blood Flow and Metabolism*. 1985;5(1):65-69. doi:10.1038/jcbfm.1985.9

139. Mesquita RC, Schenkel SS, Minkoff DL, et al. Influence of probe pressure on the diffuse correlation spectroscopy blood flow signal: extra-cerebral contributions. *Biomedical Optics Express*. 2013;4(7):978. doi:10.1364/BOE.4.000978

140. Lin LIK. A Concordance Correlation Coefficient to Evaluate Reproducibility. *Biometrics*. 1989;45(1):255. doi:10.2307/2532051

141. Bland JM, Altman DG. Measuring agreement in method comparison studies. *Statistical Methods in Medical Research*. 1999;8(2):135-160. doi:10.1191/096228099673819272

142. Koo TK, Li MY. A Guideline of Selecting and Reporting Intraclass Correlation Coefficients for Reliability Research. *Journal of Chiropractic Medicine*. 2016;15(2):155-163. doi:10.1016/j.jcm.2016.02.012

143. Cicchetti D V. Guidelines, Criteria, and Rules of Thumb for Evaluating Normed and Standardized Assessment Instruments in Psychology. *Psychological Assessment*. 1994;6(4):284-290. doi:10.1037/1040-3590.6.4.284

144. Wu L, Chung JY, Saith S, et al. Repetitive head injury in adolescent mice: A role for vascular inflammation. *Journal of Cerebral Blood Flow & Metabolism*. Published online 2018:0271678X1878663. doi:10.1177/0271678X18786633

145. Ramirez G, Proctor AR, Jung KW, et al. Chemotherapeutic drug-specific alteration of microvascular blood flow in murine breast cancer as measured by diffuse correlation spectroscopy. *Biomed Opt Express*. 2016;7(9):3610-3630. doi:10.1364/BOE.7.003610

146. Han S, Johansson J, Mireles M, et al. Non-contact scanning diffuse correlation tomography system for three-dimensional blood flow imaging in a murine bone graft model. *Biomedical Optics Express*. 2015;6(7):2695. doi:10.1364/BOE.6.002695

147. Han S, Proctor AR, Vella JB, Benoit DSW, Choe R. Non-invasive diffuse correlation tomography reveals spatial and temporal blood flow differences in murine bone grafting approaches. *Biomed Opt Express*. 2016;7(9):3262-3279. doi:10.1364/BOE.7.003262

148. Lee SY, Pakela JM, Helton MC, et al. Compact dual-mode diffuse optical system for blood perfusion monitoring in a porcine model of microvascular tissue flaps. *Journal of Biomedical Optics*. 2017;22(12):1. doi:10.1117/1.JBO.22.12.121609

149. Vishwanath K, Gurjar R, Wolf D, Riccardi S, Duggan M, King D. Diffuse optical monitoring of peripheral tissues during uncontrolled internal hemorrhage in a

porcine model. *Biomedical Optics Express*. 2018;9(2):569. doi:10.1364/BOE.9.000569

150. Lee SY, Zheng C, Buckley E. Monte-Carlo lookup table-based inverse model for non-invasive quantification of cerebral optical properties in small animal using frequency-domain near-infrared spectroscopy. In: *Biophotonics Congress: Biomedical Optics Congress*. ; 2018.

151. Lee SY, Zheng C, Buckley EM. *Small Separation Frequency-Domain near-Infrared Spectroscopy for Measurements of Cerebral Optical Properties in Rodents*.

152. Hallacoglu B, Sassaroli A, Fantini S, Troen AM. Cerebral perfusion and oxygenation are impaired by folate deficiency in rat: Absolute measurements with noninvasive near-infrared spectroscopy. *Journal of Cerebral Blood Flow and Metabolism*. 2011;31(6):1482-1492. doi:10.1038/jcbfm.2011.13

153. Heimbach D, Engrav L, Grube B, Marvin J. Burn depth: A review. *World Journal of Surgery*. 1992;16(1):10-15. doi:10.1007/BF02067108

154. Kaiser M, Yafi A, Cinat M, Choi B, Durkin AJ. Noninvasive assessment of burn wound severity using optical technology: A review of current and future modalities. *Burns*. 2011;37(3):377-386. doi:10.1016/j.burns.2010.11.012

155. Han S, Hoffman MD, Proctor AR, et al. Non-Invasive Monitoring of Temporal and Spatial Blood Flow during Bone Graft Healing Using Diffuse Correlation Spectroscopy. *PLoS One*. 2015;10(12):e0143891. doi:10.1371/journal.pone.0143891

156. Cortese L, Presti G Lo, Pagliazzi M, et al. Liquid phantoms for near-infrared and diffuse correlation spectroscopies with tunable optical and dynamic properties. *Biomedical Optics Express*. 2018;9(5):2068. doi:10.1364/boe.9.002068

157. Zanfardino S, Vishwanath K. Sensitivity of diffuse correlation spectroscopy to flow rates: a study with tissue simulating optical phantoms. In: *Medical Imaging 2018: Physics of Medical Imaging*. Vol 10573. SPIE; 2018:91. doi:10.1117/12.2293952

158. Durduran T, Yodh AG. Diffuse correlation spectroscopy for non-invasive, micro-vascular cerebral blood flow measurement. *Neuroimage*. 2014;85 Pt 1(0 1):51-63. doi:10.1016/j.neuroimage.2013.06.017

159. Góñez C, Donayre M, Villena A, Gonzales GF. Hematocrit levels in children at sea level and at high altitude: effect of adrenal androgens. *Human biology; an international record of research*. 1993;65(1):49-57.

160. Buckley EM;, Platt M, Lam W. Novel in vivo and in vitro techniques to image and model the cerebral vasculature in sickle cell disease. *Blood Cells, Moleculues and Diseases*. 2017;119(20). doi:10.1016/j.bcmd.2017.08.008

161. Carlson BM. The Circulatory System. In: *The Human Body*. ; 2019:271-301. doi:10.2307/30047425

162. Myers DR, Sakurai Y, Tran R, et al. Endothelialized Microfluidics for Studying Microvascular Interactions in Hematologic Diseases. *Journal of Visualized Experiments*. 2012;643958(64). doi:10.3791/3958

163. Tsai M, Kita A, Leach J, et al. In vitro modeling of the microvascular occlusion and thrombosis that occur in hematologic diseases using microfluidic technology. *Journal of Clinical Investigation*. 2012;122(1):408-418. doi:10.1172/JCI58753

164. Ayers F, Grant A, Kuo D, Cuccia DJ, Durkin AJ. Fabrication and characterization of silicone-based tissue phantoms with tunable optical properties in the visible and near infrared domain. In: *Design and Performance Validation of Phantoms Used in Conjunction with Optical Measurements of Tissue*. Vol 6870. ; 2008:687007. doi:10.1117/12.764969

165. Caro CG, Pedley TJ, Schroter WA. *The Mechanics of the Circulation*.; 2012.

166. Nichols WW, O'Rourke MF. *McDonald's Blood Flow in Arteries : Theoretical, Experimental and Clinical Principles*.; 2011.

167. Fantini S, Sassaroli A. Frequency-Domain Techniques for Cerebral and Functional Near-Infrared Spectroscopy. *Frontiers in Neuroscience*. 2020;14(April):1-18. doi:10.3389/fnins.2020.00300

168. Choe R. *Diffuse Optical Tomography and Spectroscopy of Breast Cancer and Fetal Brain*. 2005. doi:10.1118/1.2047847

169. Meinke M, Müller G, Helfmann J, Friebel M. Empirical model functions to calculate hematocrit-dependent optical properties of human blood. *Applied Optics*. 2007;46(10):1742. doi:10.1364/ao.46.001742

170. Tang J, Erdener SE, Li B, et al. Measurement of shear-induced diffusion of red blood cells using dynamic light scattering-optical coherence tomography. Luo Q, Ding J, eds. *Proceedings of SPIE*. Published online February 12, 2018. doi:10.1117/12.2290345

171. Cha W, Beissinger RL. Evaluation of Shear-Induced Particle Diffusivity in Red Cell Ghosts Suspensions. *Korean Journal of Chemical Engineering*. 2001;18(4):479-485. doi:10.1007/BF02698294

172. Higgins JM, Eddington DT, Bhatia SN, Mahadevan L. Statistical Dynamics of Flowing Red Blood Cells by Morphological Image Processing. *PLoS Comput Biol*. 2009;5(2):1000288. doi:10.1371/journal.pcbi.1000288

173. Bishop JJ, Popel AS, Intaglietta M, Johnson PC. Effect of aggregation and shear rate on the dispersion of red blood cells flowing in venules. *American Journal of Physiology - Heart and Circulatory Physiology*. 2002;283(5 52-5). doi:10.1152/ajpheart.00888.2001

174. Dupire J, Socol M, Viallat A. Full dynamics of a red blood cell in shear flow. *Proc Natl Acad Sci U S A*. 2012;109(51):20808-20813. doi:10.1073/pnas.1210236109

175. Stickel JJ, Powell RL. Fluid Mechanics and Rheology of Dense Suspensions. *Annual Review of Fluid Mechanics*. 2005;37(1):129-149. doi:10.1146/annurev.fluid.36.050802.122132

176. Omori T, Ishikawa T, Imai Y, Yamaguchi T. Shear-induced diffusion of red blood cells in a semi-dilute suspension. *Journal of Fluid Mechanics*. 2013;724:154-174. doi:10.1017/jfm.2013.159

177. van Staveren HJ, Moes CJM, van Marie J, Prahl SA, van Gemert MJC. Light scattering in lntralipid-10% in the wavelength range of 400–1100 nm. *Applied Optics*. 1991;30(31):4507. doi:10.1364/ao.30.004507

178. Tang J, Erdener SE, Li B, et al. Shear-induced diffusion of red blood cells measured with dynamic light scattering-optical coherence tomography. *Journal of Biophotonics*. 2017;11(2):1-10. doi:10.1002/jbio.201700070

179. Fåhræus R, Lindqvist T. The Viscosity of the Blood in Narrow Capillary Tubes. *American Journal of Physiology-Legacy Content*. 1931;96(3):562-568. doi:10.1152/ajplegacy.1931.96.3.562

180. Pries AR, Neuhaus D, Gaehtgens P. Blood viscosity in tube flow: Dependence on diameter and hematocrit. *American Journal of Physiology - Heart and Circulatory Physiology*. 1992;263(6 32-6). doi:10.1152/ajpheart.1992.263.6.h1770

181. Lima R, Ishikawa T, Imai Y, Takeda M, Wada S, Yamaguchi T. Radial dispersion of red blood cells in blood flowing through glass capillaries: The role of hematocrit and geometry. *Journal of Biomechanics*. 2008;41(10):2188-2196. doi:10.1016/j.jbiomech.2008.04.033

182. Lee SY, Cowdrick KR, Sanders B, et al. Noninvasive optical assessment of resting-state cerebral blood flow in children with sickle cell disease. *Neurophotonics*. 2019;6(03):1. doi:10.1117/1.nph.6.3.035006

183. Fields ME, Guilliams KP, Ragan DK, et al. Regional oxygen extraction predicts border zone vulnerability to stroke in sickle cell disease. *Neurology*. Published online 2018. doi:10.1212/WNL.0000000000005194

184. Prohovnik I, Pavlakis SG, Piomelli S, et al. Cerebral hyperemia, stroke, and transfusion in sickle cell disease. *Neurology*. 1989;39(3):344-348. doi:10.1212/wnl.39.3.344

185. Herold S, Brozovic M, Gibbs J, et al. Measurement of regional cerebral blood flow, blood volume and oxygen metabolism in patients with sickle cell disease using positron emission tomography. *Stroke*. 1986;17(4):692-698. doi:10.1161/01.STR.17.4.692

186. Tsai M, Kita A, Leach J, et al. In vitro modeling of the microvascular occlusion and thrombosis that occur in hematologic diseases using microfluidic technology. *The Journal of clinical …*. 2012;122(1). doi:10.1172/JCI58753DS1

187. Secomb TW, Pries AR. Blood viscosity in microvessels: Experiment and theory. *Comptes Rendus Physique*. 2013;14(6):470-478. doi:10.1016/j.crhy.2013.04.002

188. Fantini S, Franceschini MA. Frequency-Domain Techniques for Tissue Spectroscopy and Imaging. In: *Handbook of Optical Biomedical Diagnostics, Second Edition, Volume 1: Light-Tissue Interaction*. ; 2017. doi:10.1117/3.2219603.ch7

189. Arslan-Ergül A. Computational study of scattering from healthy and diseased red blood cells. *Journal of Biomedical Optics*. 2010;15(4):045004. doi:10.1117/1.3467493

190. Pusey PN. Dynamic light scattering by non-ergodic media. *Macromolecular Symposia*. 1994;79:17-30.

191. Prahl SA, van Gemert MJC, Welch AJ. Determining the optical properties of turbid media by using the adding–doubling method. *Applied Optics*. 1993;32(4):559. doi:10.1364/ao.32.000559

192. Connolly ES, Rabinstein AA, Carhuapoma JR, et al. Guidelines for the management of aneurysmal subarachnoid hemorrhage: A guideline for healthcare professionals from the american heart association/american stroke association. *Stroke*. 2012;43(6):1711-1737. doi:10.1161/STR.0b013e3182587839

193. Etminan N, Chang HS, Hackenberg K, et al. Worldwide Incidence of Aneurysmal Subarachnoid Hemorrhage According to Region, Time Period, Blood Pressure, and Smoking Prevalence in the Population: A Systematic Review and Meta-analysis. *JAMA Neurology*. 2019;76(5):588-597. doi:10.1001/jamaneurol.2019.0006

194. Dabus G, Nogueira RG. Current Options for the Management of Aneurysmal Subarachnoid Hemorrhage-Induced Cerebral Vasospasm: A Comprehensive Review of the Literature Dabus et al.: Current Options for the Management of Aneurysmal Subarachnoid Hemorrhage-Induced Cerebral Vasospasm. *Intervent Neurol*. 2013;2:30-51. doi:10.1159/000354755

195. Grubb RL, Raichle ME, Eichling JO, Gado MH. Effects of subarachnoid hemorrhage on cerebral blood volume, blood flow, and oxygen utilization in humans. *Journal of Neurosurgery*. 1977;46.

196. Ohkuma H, Manabe H, Tanaka M, Suzuki S. Impact of Cerebral Microcirculatory Changes on Cerebral Blood Flow During Cerebral Vasospasm After Aneurysmal Subarachnoid Hemorrhage. *Stroke*. Published online 2000:1621-1627.

197. Bhogal P, Yeo LL, Müller LO, Blanco PJ. The Effects of Cerebral Vasospasm on Cerebral Blood Flow and the Effects of Induced Hypertension: A Mathematical Modelling Study. *Interventional Neurology*. 2020;8(2-6):152-163. doi:10.1159/000496616

198. Schweizer TA, Al-Khindi T, Loch Macdonald R. Mini-Mental State Examination versus Montreal Cognitive Assessment: Rapid assessment tools for cognitive and functional outcome after aneurysmal subarachnoid hemorrhage. *Journal of the Neurological Sciences*. 2012;316:137-140. doi:10.1016/j.jns.2012.01.003

199. Sadan O, Waddel H, Moore R, et al. Does intrathecal nicardipine for cerebral vasospasm following subarachnoid hemorrhage correlate with reduced delayed cerebral ischemia? A retrospective propensity score–based analysis. *Journal of Neurosurgery*. 2021;0:1-10. doi:10.3171/2020.12.jns203673

200. Haley EC, Kassell NF, Torner JC. A randomized controlled trial of high-dose intravenous nicardipine in aneurysmal subarachnoid hemorrhage. A report of the Cooperative Aneurysm Study. *Journal of Neurosurgery*. 1993;78(4):537-547. doi:10.3171/jns.1993.78.4.0537

201. Hafeez S, Grandhi R. Systematic Review of Intrathecal Nicardipine for the Treatment of Cerebral Vasospasm in Aneurysmal Subarachnoid Hemorrhage. *Neurocritical Care*. 2019;31(2):399-405. doi:10.1007/s12028-018-0659-9

202. Diana F, Romano DG, Peschillo S. Distribution of symptomatic cerebral vasospasm following subarachnoid hemorrhage assessed using cone beam CT angiography. *Journal of NeuroInterventional Surgery*. 2021;0:neurintsurg-2021-018528. doi:10.1136/neurintsurg-2021-018528

203. Simonato D, Borchert RJ, Vallee F, et al. Distribution of symptomatic cerebral vasospasm following subarachnoid hemorrhage assessed using cone-beam CT angiography Hemorrhagic stroke. *J NeuroIntervent Surg*. 2021;0:1-5. doi:10.1136/neurintsurg-2021-018080

204. Fukui MB, Johnson DW, Yonas H, Sekhar L, Latchaw RE, Pentheni S. Xe / CT Cerebral Blood Flow Evaluation of Delayed Symptomatic Cerebral Ischemia after Subarachnoid Hemorrhage. *American Journal of Neuroradiology*. Published online 1992:265-270.

205. Shibuya M, Suzuki Y, Enomoto H, Okada T, Ogura K, Sugita K. Effects of prophylactic intrathecal administrations of nicardipine on vasospasm in patients with severe aneurysmal subarachnoid haemorrhage. *Acta Neurochirurgica*. 1994;131(1-2):19-25. doi:10.1007/BF01401450

206. Shibuya M, Suzuki Y, Takayasu M, Asano T, Ikegaki I, Sugita K. Effects of intrathecal administration of nicardipine and nifedipine on chronic cerebral vasospasm in dogs. *Journal of Clinical Neuroscience*. 1994;1(1):58-61. doi:10.1016/0967-5868(94)90012-4

207. Pasqualin A, Vollmer DG, Marron JA, Tsukahara T, Kassell NF, Torner JC. The Effect of Nicardipine on Vasospasm in Rabbit Basilar Artery after Subarachnoid Hemorrhage. *Neurosurgery*. 1991;29(2).

208. Peppiatt CM, Howarth C, Mobbs P, Attwell D. Bidirectional control of CNS capillary diameter by pericytes. *Nature*. 2006;443(7112):700-704. doi:10.1038/nature05193

209. Kamouchi M, Kitazono T, Ago T, et al. Calcium influx pathways in rat CNS pericytes. *Molecular Brain Research*. 2004;126(2):114-120. doi:10.1016/j.molbrainres.2004.03.008

210. Rosenthal G, Hemphill JC, Sorani M, et al. Brain tissue oxygen tension is more indicative of oxygen diffusion than oxygen delivery and metabolism in patients with traumatic brain injury. *Critical Care Medicine*. 2008;36(6):1917-1924. doi:10.1097/CCM.0b013e3181743d77

211. Brady KM, Lee JK, Kibler KK, Easley RB, Koehler RC, Shaffner DH. Continuous measurement of autoregulation by spontaneous fluctuations in cerebral perfusion pressure: comparison of 3 methods. *Stroke; a journal of cerebral circulation*. 2008;39(9):2531-2537. doi:10.1161/STROKEAHA.108.514877

212. Eriksson EA, Barletta JF, Figueroa BE, et al. Cerebral perfusion pressure and intracranial pressure are not surrogates for brain tissue oxygenation in traumatic brain injury. *Clinical Neurophysiology*. 2012;123(6):1255-1260. doi:10.1016/j.clinph.2011.08.035

213. Boas DA, Campbell LE, Yodh AG. Scattering and Imaging with Diffusing Temporal Field Correlations. *Physical Review Letters*. 1995;75(9):1855-1858. doi:10.1103/PhysRevLett.75.1855

214. Giovannella M, Andresen B, Andersen JB, et al. Validation of diffuse correlation spectroscopy against 15O-water PET for regional cerebral blood flow measurement in neonatal piglets. *Journal of Cerebral Blood Flow and Metabolism*. Published online October 30, 2019. doi:10.1177/0271678X19883751

215. Kim MN, Durduran T, Frangos S, et al. Noninvasive measurement of cerebral blood flow and blood oxygenation using near-infrared and diffuse correlation spectroscopies in critically brain-injured adults. *Neurocritical Care*. 2010;12(2):173-180. doi:10.1007/s12028-009-9305-x

216. Wang D, Parthasarathy AB, Baker WB, et al. Fast blood flow monitoring in deep tissues with real-time software correlators. *Biomedical Optics Express*. 2016;7(3):776. doi:10.1364/BOE.7.000776

217. Pulse Waveform Delineator - File Exchange - MATLAB Central. Accessed January 18, 2022. https://www.mathworks.com/matlabcentral/fileexchange/29484-pulse-waveform-delineator

218. Wechsler LR, Babikian VL, Baron JC, et al. Neuroimaging CPC Advances in Technology Book Reviews EDITORIAL BOARD. *NeuroImaging*. 2002;12(2).

219. Proust-Lima C, Philipps V, Liquet B. Estimation of extended mixed models using latent classes and latent processes: The R package lcmm. *Journal of Statistical Software*. 2017;78(2). doi:10.18637/jss.v078.i02

220. Pegoli M, Mandrekar J, Rabinstein AA, Lanzino G. Predictors of excellent functional outcome in aneurysmal subarachnoid hemorrhage. *Journal of Neurosurgery*. 2015;122(2):414-418. doi:10.3171/2014.10.JNS14290

221. Eagles ME, Tso MK, Macdonald RL. Cognitive Impairment, Functional Outcome, and Delayed Cerebral Ischemia After Aneurysmal Subarachnoid Hemorrhage. *World Neurosurgery*. 2019;124:e558-e562. doi:10.1016/j.wneu.2018.12.152

222. Naraoka M, Matsuda N, Shimamura N, Asano K, Ohkuma H. The Role of Arterioles and the Microcirculation in the Development of Vasospasm after Aneurysmal SAH. Published online 2014. doi:10.1155/2014/253746

223. Suzuki H, Kanamaru H, Kawakita F, Asada R, Fujimoto M, Shiba M. Cerebrovascular pathophysiology of delayed cerebral ischemia after aneurysmal subarachnoid hemorrhage. *Histology and Histopathology*. 2021;36(2):143-158. doi:10.14670/HH-18-253

224. Vorkapic P, Bevan RD, Bevan JA. Longitudinal time course of reversible and irreversible components of chronic cerebrovasospasm of the rabbit basilar artery. *Journal of Neurosurgery*. 1991;74(6):951-955. doi:10.3171/jns.1991.74.6.0951

225. Dankbaar JW, Rijsdijk M, van der Schaaf IC, Velthuis BK, Wermer MJH, Rinkel GJE. Relationship between vasospasm, cerebral perfusion, and delayed cerebral ischemia after aneurysmal subarachnoid hemorrhage. *Neuroradiology*. 2009;51(12):813-819. doi:10.1007/s00234-009-0575-y

226. Zhao H, Cooper RJ. Review of recent progress toward a fiberless, whole-scalp diffuse optical tomography system. *Neurophotonics*. 2017;5(01):1. doi:10.1117/1.nph.5.1.011012

227. Pinti P, Aichelburg C, Gilbert S, et al. A Review on the Use of Wearable Functional Near-Infrared Spectroscopy in Naturalistic Environments. *Jpn Psychol Res*. 2018;14(4):535-562. doi:10.1111/jpr.12206.A

228. Tobias JD. Nicardipine: Applications in anesthesia practice. *Journal of Clinical Anesthesia*. 1995;7(6):525-533. doi:10.1016/0952-8180(95)00093-W

229. Vergouwen MDI. Vasospasm versus delayed cerebral ischemia as an outcome event in clinical trials and observational studies. *Neurocritical Care*. 2011;15(2):308-311. doi:10.1007/s12028-011-9586-8

230. Kienle A, Patterson MS. Determination of the optical properties of semi-infinite turbid media from frequency-domain reflectance close to the source. *Phys Med Biol*. 1997;42:1801-1819.

231. Farzam P, Buckley EM, Lin PY, et al. Shedding light on the neonatal brain: Probing cerebral hemodynamics by diffuse optical spectroscopic methods. *Scientific Reports*. 2017;7(1). doi:10.1038/s41598-017-15995-1

232. Wu KC, Farzam P, Sheriff F, et al. Critical closing pressure measured in stroke patients with diffuse correlation spectroscopy and transcranial Doppler ultrasound. *J Biomed Opt*. 2021;(March). doi:10.1364/BRAIN.2019.BW4A.4

233. Ruesch A, Yang J, Schmitt S, Acharya D, Smith MA, Kainerstorfer JM. Estimating intracranial pressure using pulsatile cerebral blood flow measured with diffuse correlation spectroscopy. *Biomedical Optics Express*. 2020;11(3):1462. doi:10.1364/boe.386612

234. Fischer JB, Ghouse A, Tagliabue S, et al. Non-invasive estimation of intracranial pressure by diffuse correlation spectroscopy. Published online 2020:BTh3C.4. doi:10.1364/brain.2020.bth3c.4

235. Baker WB, Parthasarathy AB, Gannon KP, et al. Noninvasive optical monitoring of critical closing pressure and arteriole compliance in human subjects. *Journal of Cerebral Blood Flow & Metabolism*. 2017;37(8):2691-2705. doi:10.1177/0271678X17709166

236. Zhang R, Zuckerman JH, Giller CA, Levine BD. Transfer function analysis of dynamic cerebral autoregulation in humans. *American Journal of Physiology - Heart and Circulatory Physiology*. 1998;274(1):H233-H241. doi:10.1016/j.preghy.2015.09.001

237. Parthasarathy AB, Gannon KP, Baker WB, et al. Dynamic autoregulation of cerebral blood flow measured non-invasively with fast diffuse correlation spectroscopy. *Journal of Cerebral Blood Flow and Metabolism*. 2018;38(2):230-240. doi:10.1177/0271678X17747833